From two-dimensional materials to their heterostructures: An electrochemist's perspective

Velicky, M., & Toth, P. S. (2017). From two-dimensional materials to their heterostructures: An electrochemist's perspective. Applied Materials Today, 8, 68-103. DOI: 10.1016/j.apmt.2017.05.003

Published in:
Applied Materials Today

Document Version:
Publisher's PDF, also known as Version of record

Applied Materials Today 8 (2017) 68–103

Contents lists available at ScienceDirect

Applied Materials Today

journal homepage: www.elsevier.com/locate/apmt

Review

From two-dimensional materials to their heterostructures: An electrochemist's perspective

Matěj Velický[a,b,*], Peter S. Toth[c,d]

[a] Centre for Nanostructured Media, School of Mathematics and Physics, Queen's University Belfast, University Road, Belfast BT7 1NN, UK
[b] School of Chemistry, University of Manchester, Oxford Road, Manchester M13 9PL, UK
[c] Graphene Labs, Istituto Italiano di Tecnologia, Via Morego 30, Genoa 16163, Italy
[d] iCub Facility, Istituto Italiano di Tecnologia, Via Morego 30, Genoa 16163, Italy

ARTICLE INFO

Article history:
Received 31 March 2017
Received in revised form 9 May 2017
Accepted 9 May 2017

Keywords:
2D materials
TMDC
Heterostructures
Electrochemistry
Photovoltaics

ABSTRACT

Two-dimensional (2D) materials have, within just one decade, reshaped many disciplines of modern science and technology, both through intensive fundamental research and early commercial applications. In this review, we will provide a comprehensive summary of the properties, synthesis, characterisation, and application of 2D materials in the context of electrochemistry and related scientific fields. Firstly, the structural, electronic, optical, and mechanical properties, and a variety of preparation and characterisation techniques of 2D materials are presented. Secondly, current electrochemical understanding of 2D and layered materials and their modification is discussed. Lastly, future perspectives and new frontiers in optoelectronics, photocatalysis, and renewable energy using 2D materials are outlined.

Our primary focus is on group 6 transition metal dichalcogenides (TMDCs) and other emerging 2D materials beyond graphene, including their heterostructures. These nanomaterials are essential for the next generation of devices in tuneable electrochemistry, sensing, and photovoltaics. Although broad in scope, this review is not an exhaustive list of facts; rather, it summarises the established knowledge and pinpoints the most promising future trends. It is aimed at readers with background in electrochemistry wanting to broaden their perspective or initiate research on 2D materials as well as those with 2D materials expertise looking to work on electrochemistry-based applications, such as energy storage and conversion.

Contents

* Corresponding author at: Centre for Nanostructured Media, School of Mathematics and Physics, Queen's University Belfast, University Road, Belfast, BT7 1NN, UK.
E-mail addresses: m.velicky@qub.ac.uk, matej.velicky@manchester.ac.uk (M. Velický).

http://dx.doi.org/10.1016/j.apmt.2017.05.003

1. Introduction

Two-dimensional (2D) materials are crystalline solids with a high ratio between their lateral size (~1–10,000 μm) and thickness (<1 nm) [1]. The layered structure of the corresponding bulk crystals, which facilitates their exfoliation to 2D layers, originates from the strong intralayer covalent bonding and comparatively weaker interlayer van der Waals (vdW) interaction with typical binding energies of 40–70 meV [2]. The electronic transport and therefore conductivity in layered materials is much more efficient through the layers (i.e. in the direction perpendicular to the vertical *c*-axis) than between the layers, typically by 3 or 4 orders of magnitude [3]. This is due to the strong charge carrier localisation within the individual layers and simultaneous transport of charge carriers through multiple layers [4]. The basal plane of 2D and layered materials (perpendicular to the *c*-axis) is well defined and chemically stable surface due to the absence of dangling bonds, unlike the edge plane (parallel to the *c*-axis), which is usually terminated by various surface groups [5]. The discovery of graphene and its unique properties in 2004 [6] launched a scientific revolution due to the fact that 2D materials were long thought to be thermodynamically unstable [7]. A large number of other layered materials with diverse properties based on the elements highlighted in Fig. 1a were gradually exfoliated in 2D. These include hexagonal boron nitride (hBN), metal and non-metal chalcogenides, oxides, hydroxides and halides, covalent organic frameworks, silicates, and perovskites [8–14].

Graphene stands out amongst other 2D materials due to its unique electronic band structure and the associated record carrier mobility, thermal conductivity, and high transparency. These properties make it a serious candidate for the replacement of indium tin oxide (ITO), a transparent conductive material, successfully used in liquid crystal displays, touch panels, or light-emitting diodes, whose performance is compromised by its low-flexibility, conflicting opposing relationship between its optical transparency and conductivity, and low abundance of indium [15]. However, many other 2D materials have what graphene does not: a band gap of 1–2 eV, which is well matched to the solar spectrum and is comparable to the current industrial standards in photovoltaics: Si (1.1 eV), GaAs (1.4 eV), or CdTe (1.5 eV) [16]. 2D crystals of high-κ dielectrics, i.e. highly insulating materials such as hBN, mica, or perovskites, can be used as tunnelling barriers in capacitors and gate insulators [11]. The future generations of nanoelectronics, beyond the silicon-based era, need to address the ever-increasing drive for the reduction in size of the circuit-elements in digital electronics without compromising their quality. Utilisation of the sub-nanometre thickness and high quality of atomically-thin 2D materials in electronic circuits offers an effective electrostatic control of conductivity. Furthermore, the lack of surface groups or dangling bonds in 2D materials reduces charge carrier scattering otherwise common in bulk materials. The high surface-to-volume ratio of 2D materials is directly exploitable in electrochemistry [17] and results in their extreme sensitivity to the environment applicable in molecular sensors [18]. The vanishingly small thickness of 2D materials should further lead to a reduction in volume, mass, and ultimately the cost of devices in many applications such as transparent solar cells, conductive displays, or protective light-absorbing layers. Other applications such spintronics, valleytronics, photonics, or plasmonics, exploiting more exotic properties of 2D materials, were also proposed or realised [2,19–23].

TMDCs are a large group of crystals with a generic chemical formula of MX_2 (M = transition metal, X = S, Se, or Te), about two thirds of which are known to form layered structures [8]. Significant scientific knowledge of bulk TMDCs has been accumulated in 1960–80s, especially for the group 6 TMDCs, where M = Mo or W, and, following the success of graphene, their mono- and few-layer forms were soon produced [9]. Typically, group 4 or 6 TMDCs are semiconductors or insulators, while group 5 TMDCs are metallic [23,24]. Other metal chalcogenides, which have attracted interest in the recent years include PtS_2, InSe, and SnS_2. Semiconducting TMDCs hold promise for a number of applications ranging from photovoltaics [25], photodetection [26], optoelectronics [23], light-emitting diodes [27], to energy storage/conversion, sensing, and catalysis [5,28]. Molybdenum disulphide (MoS_2) is the most common TMDC, which has traditionally been used as a lubricant [29–31], and as an intercalation host [32], following the successful use of graphite-based Li-ion batteries. Monolayer MoS_2 has soon been implemented in field-effect transistors (FET) (Fig. 2e) with superb on/off ratios of 10^7–10^8 [26,33,34] in comparison to the much lower 10^0–10^1 on/off ratios typical for graphene [35], and phototransistors with fast (>50 ms) switching times [36]. Optoelectronic properties of 2D materials are dominated by quasiparticles such as excitons and trions, i.e. bound complexes of photogenerated holes and electrons. Their binding energies are typically 1 or 2 orders of magnitude larger than in conventional 3D semiconductors, which results in their longer lifetimes and diffusion paths prior to their recombination, making them relevant and observable at room temperature [37].

The overarching idea behind the enormous research efforts in the field of 2D materials is the prospect of building an inventory of stable, atomically-thin building blocks of nanomaterials, whose electronic properties range widely from insulators (e.g. hBN or mica), semiconductors (e.g. MoS_2 or phosphorene), semimetals (e.g. graphene or TiS_2), to metals (e.g. VSe_2 or $PtTe_2$), or even more exotic groups of materials such as superconductors (e.g. $NbSe_2$ or TaS_2) or topological insulators (e.g. Bi_2Te_3 or stanene). Furthermore, heterostructures can be constructed either by stacking of the individual 2D materials on top of one another (vdW heterostructures), or through synthesis of different 2D materials in the same plane (lateral heterostructures), which opens a much wider world of artificial nanomaterials with diverse functionalities packed into

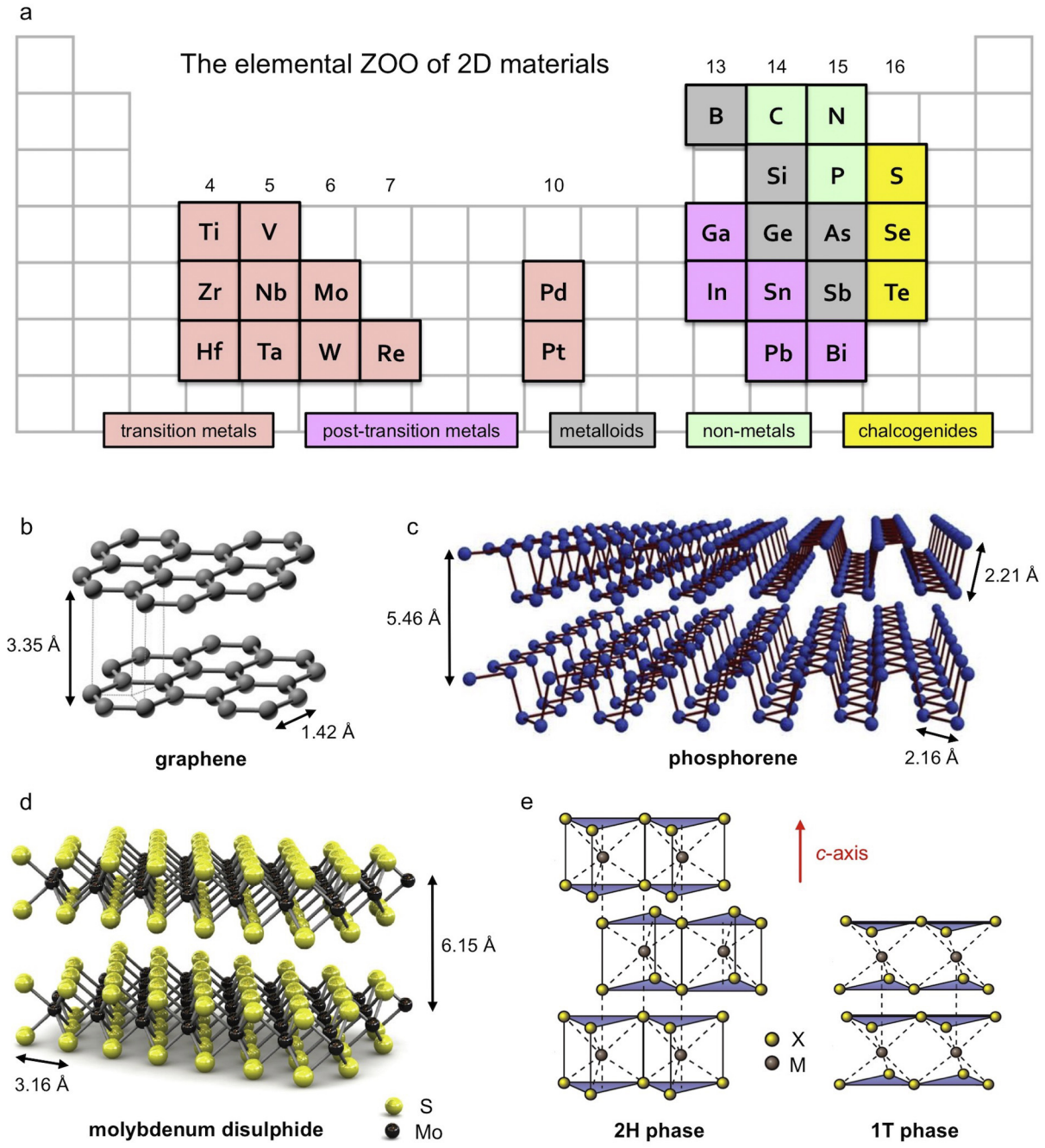

Fig. 1. Two-dimensional ZOO. a, Simplified periodic table highlighting the elements, which form the most common layered and 2D materials. b,c,d, Crystal structures of graphene, phosphorene, and MoS_2 bilayers, respectively. e, Schematic of the two most common TMDC phases, 2H and 1T. The lattice parameters in b, c, and d are taken from [368], [369], and [24], respectively. Figures adapted with permission from: b, [47] © 2011 American Physical Society. c, [99] © 2000 John Wiley and Sons. d, [33] © 2011 Nature Publishing Group. e, [23] © 2012 Nature Publishing Group.

a thickness of a few nm [22,38]. Importantly, the properties of 2D materials can be tuned "on-demand" by external stimuli such as electric field, strain, illumination, or functionalisation. In the following chapters we will review the fundamental properties of 2D materials in the context of electrochemistry and condensed matter physics.

2. Properties, preparation, and characterisation of 2D materials

2.1. Crystal structure of 2D materials

Monolayer graphene and hBN are the only true 2D crystals where all the atoms, covalently bound in a hexagonal lattice, occupy the same plane (Fig. 1b). Other single-element 2D materials such as phosphorene form corrugated (or buckled) structures with the atoms distributed across more than one plane (Fig. 1c).

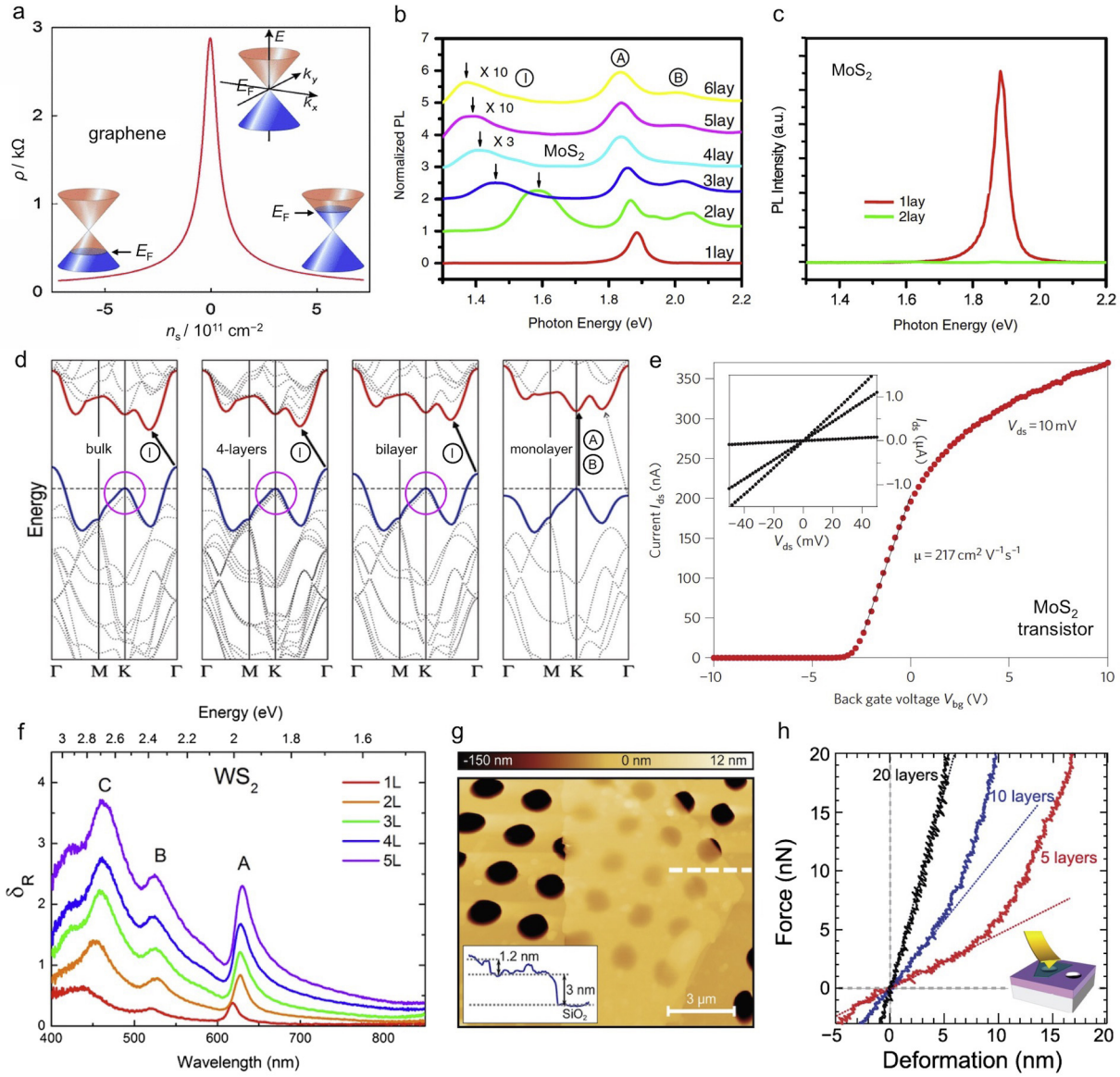

Fig. 2. Electronic, optical, and mechanical properties of 2D materials. a, Dependence of resistance on carrier concentration in monolayer graphene. b, Evolution of the PL with the number of layers in MoS_2 due to the indirect-to-direct band gap transition between bulk and monolayer. c, The increase in PL intensity observed in monolayer MoS_2. d, Changes in the electronic band structure of MoS_2 as a function of thickness. e, Current–voltage characteristics of a monolayer MoS_2 FET. f, Differential reflectance spectra of WS_2 as a function of thickness. g, AFM image of a few-layer MoS_2 crystal suspended over micron-sized holes in an SiO_2 substrate. h, Corresponding measurement of the applied force as a function of deformation for different MoS_2 thicknesses. The abbreviations in b, d, and f correspond to the A, B, and C excitons and the indirect transition (I). Figures adapted with permission from: a, [47] © 2011 American Physical Society. b–c, [63] © 2010 American Physical Society. d, [68] © 2010 American Chemical Society. e, [33] © 2011 Nature Publishing Group. f, [165] © 2013 American Chemical Society. g–h, [81] © 2012 John Wiley and Sons.

Table 1
Crystal structure parameters of the most common TMDCs.

2D material	Interlayer distance[a] (Å)	vdW gap[b] (Å)	MX_2 sandwich thickness (Å)	M–X bond length (Å)	M|M distance[c] (Å)
2H-MoS_2	6.15	2.98	3.17	2.42	3.16
2H-$MoSe_2$	6.47	3.24	3.23	2.49	3.29
2H-$MoTe_2$	7.28	3.68	3.60	2.72	3.52
2H-WS_2	6.16	3.02	3.14	2.40	3.15
2H-WSe_2	7.00	3.76	3.24	2.49	3.29
1T′-WTe_2	7.02	3.80–3.90	3.50–4.00	2.71–2.82	2.86

[a] Distance the M atomic planes in two neighbouring layers.
[b] Closest distance between the X atomic planes in two neighbouring layers.
[c] Closest distance between two M atoms (also between two X atoms).
Data collected from the following references: [24,42,45,46,370,371].

Table 2
Charge carrier mobility in graphene and TMDCs.

2D material	Mobility[a] ($cm^2 V^{-1} s^{-1}$)	
	Bulk (>10 layers)	Monolayer
Graphene	10,000	>140,000
2H-MoS_2	60–200	>200
2H-$MoSe_2$	160–250	50
2H-$MoTe_2$	40	–
2H-WS_2	20–100	0.2
2H-WSe_2	120–150	30–180
1T'-WTe_2	6000–44,000	20–21,000

[a] Typical values at room temperature (large variation is common in literature).
Data collected from the following references: [4,33,52,54,75,117,134,137,354,372].

Table 3
Band gap evolution with thickness for the most common TMDCs.

2D material	Band gap (eV)				
	Bulk	Tetralayer	Trilayer	Bilayer	Monolayer
2H-MoS_2	1.23^I	1.41^I	1.46^I	1.59^I	1.89^D
2H-$MoSe_2$	1.09^I	–	1.34^I	1.46^I	1.57^D
2H-$MoTe_2$	0.93^I	1.00^I	1.02	1.05^I	1.08^D
2H-WS_2	1.35^I	1.47^I	1.53^I	1.73^I	1.98^D
2H-WSe_2	1.20^I	1.42^I	1.45^I	1.54^I	1.66^D
1T'-WTe_2	Semimetal/metal (~0.5 eV overlap between W 5*d* and Te 5*p* bands)				

^{I} Indirect band gap determined at room temperature.
^{D} Direct band gap determined at room temperature.
Data collected from the following references: [43,63,69,165,245,249].

Monolayer TMDCs are three atoms thick and comprise of an X–M–X sandwich (Fig. 1d and e) with either trigonal prismatic or octahedral coordination of the metal atom [24]. The *d* orbitals of M and the *p* orbitals of X facilitate their covalent bonding within an MX_2 monolayer, the atoms are arranged in a hexagonal pattern when viewed in the *c*-axis direction, and the individual layers are held by the weak vdW forces. Importantly, all the accessible orbitals of M and X at the basal surface are involved in the intralayer bonding, leaving only the high-energy antibonding orbitals for interlayer or external bonding, which leads to a complete absence of dangling bonds [30]. The interlayer distances and intralayer bond lengths generally increase with the size of M and X, as shown in Table 1.

The metal coordination and stacking order between the individual layers defines the phase or the polytype of a TMDC (Fig. 1e). Common phases are 1T, 2H, or 3R, where 1, 2, 3 defines the number of X–M–X sandwiches per unit cell in the *c* axis direction and T (tetragonal), H (hexagonal), R (rhombohedral) denotes the crystal symmetry [24,39]. The phase determines the properties of TMDCs: i.e. MoS_2 exist either as 2H, which is a thermodynamically stable semiconducting phase with a bulk band gap of ~1.2 eV, or as 1T, which is a metastable metallic phase. The 2H and 1T phases can be transformed to one another by simple gliding of the atomic planes, demonstrated by an in situ electron microscopy [40], or by chemical modification [41]. The coordination of the M atoms is a trigonal prismatic in the 1H and 3R phases and octahedral in the 1T phase (Fig. 1e) [24].

Most group 6 TMDCs exist in the 2H phase but the tellurides are also prone to form the 1T′ distorted octahedral structure of CdI_2, sometimes also called Td phase [8,24,42]. The displacement of the M atoms from the octahedral centre in the 1T′ phase leads to a reduction in the minimum M|M distance and to a semimetallic behaviour as shown in Tables 1–3 [43–46]. From hereon, all TMDCs will be assumed to be of the 2H phase, unless stated otherwise.

2.2. Electronic, optical, and mechanical properties of 2D materials

Band diagrams describe the electronic structure of solids, whose multitude of electronic states lead to continuum-like bands of allowed energy levels. Solids are then classified based on their electronic structure: metals and semimetals with a large and small overlap between their valence band (VB) and conduction band (CB), respectively, and semiconductors and insulators with a 1–4 eV and >4 eV band gap between their VB and CB, respectively. Graphene occupies a unique position amongst other 2D materials due to its zero-band gap semiconducting nature and a linear dispersion of charge carriers near the K and K′ points of the Brillouin zone. This results in relativistic-like charge carriers, wavelength-independent light absorption, Klein tunnelling, and other interesting physical phenomena [7,47]. Conductivity (σ) of graphene is intrinsically high due to the high charge carrier mobility (μ) in graphene, and it is readily tuneable through charge carrier density (n), according to the Eq. (1), where e is the elementary charge. Fig. 2a demonstrates this ambipolar nature of graphene in the vicinity of the Dirac point [6,48].

$$\sigma = ne\mu \quad (1)$$

The charge carrier mobility of semiconducting 2D materials is strongly dependent on factors such as charge carrier polarity, temperature, number of layers, substrate, charged impurities, localised states, defects, device geometry, and contacts. Thus, large discrepancies are found in the electronic transport of mono- and few-layer MoS_2 with the mobility ranging over 6 orders of magnitude, between 0.03 and 34,000 $cm^2 V^{-1} s^{-1}$ [18,33,49,50]. The mobility generally increases with the number of layers in TMDC FETs [18,51,52], although exception to this have been reported [26] and attributed to the interlayer resistance [53]. The charge carrier density depends on the intrinsic and extrinsic doping levels, electric field, and recombination centres. The typical values of ~10^{12} cm^{-2} increase significantly to 10^{13}–10^{14} cm^{-2} when electrochemical top-gating using polymers, ionic liquids, or organic solvents is employed [54], as discussed later. Mobilities of graphene and group 6 TMDCs are compared in Table 2.

Semiconducting 2D materials also experience strong enhancement of the Coulomb interactions among charge carriers and defects due to the quantum confinement and significantly reduced dielectric screening [55,56], as schematically shown in Fig. 3a. As a result, long-lived excitons and trions with spatial extent of several nm are observed in monolayer TMDCs [37,57]. Their binding energies, e.g. ~320 meV for excitons in WS_2 [57] and ~20 meV for trions in MoS_2 [58], which are several times higher than those in bulk, imply high thermal stability of these quasiparticles at room temperature and therefore their direct relevance to electrochemical studies. Biexcitons with a binding energy of ~52 meV have also been recently observed in the emission spectra of monolayer WSe_2 at high exciton densities [59]. These results open new experimental avenues for studying many body physics phenomena, which were previously only observed in exotic systems such as quantum wells at low temperatures [60,61].

The electronic band structure of most 2D materials is thickness-dependent as a result of the strong interlayer coupling and quantum confinement (Figs. 2b–d and 3b) [62–64]. Due to the strong hybridisation between *d* orbitals of the M atoms, bulk group 6 2H-TMDCs possess an indirect band gap of 0.9–1.4 eV, originating from the transition between the VB maximum (VBM) at the Γ point to the CB minimum (CBM) halfway between the Γ and K points [8,65], as shown in Fig. 2d and Table 3. This indirect transition is strongly affected by the presence of neighbouring layers due to the fact that the VBM states near the Γ point are a linear combination of the *d* and *p* orbitals of M and X and that the involved holes and electrons have low out-of-plane masses. In contrast, the smallest direct band gap, which is larger in size than the indirect one, originates from the *d*–*d* metal orbital transitions at the K (and K′) point of the VBM and CBM [24,66,67]. The direct transition remains almost

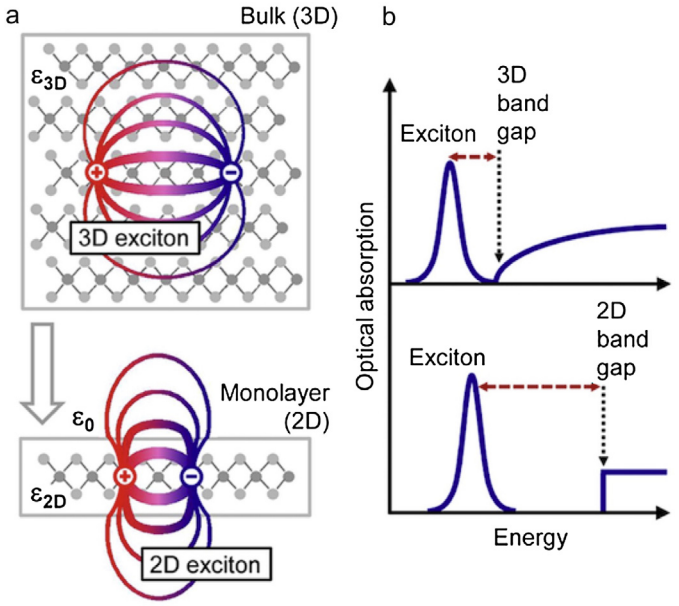

Fig. 3. Quantum confinement and reduced dielectric screening in 2D materials. a, Schematic of the confinement of charge carriers and the reduced dielectric screening due to the absence of adjacent layers in 2D materials in comparison to bulk 3D materials. b, Consequent increase of the band gap and exciton binding energy in semiconducting 2D materials. Figure adapted with permission from [57] © 2014 American Physical Society.

unaffected by the interlayer interaction because the M *d* orbitals are nested inside the X–M–X sandwich and the holes and electrons at the K (K′) point have much higher out-of-plane mass than free electrons [63,67,68]. As a result, the indirect band gap is strongly dependent of the number of layers, while the direct one is not (Fig. 2d). These changes are manifested by energy shifts in the TMDC photoluminescence (PL) spectra shown in Fig. 2b. Importantly for optoelectronics, this band structure evolution is accompanied by an enormous increase of PL intensity in monolayer TMDCs in comparison to thicker layers [63,68,69] as shown in Fig. 2c. For the group 6 TMDCs, the band gaps increase with the increasing size of M and decreasing size of X, regardless of thickness [23,62,70], as shown in Table 3, whereas the VBM and the CBM increase with the increasing size of both M and X [37,71]. Furthermore, the direct band gap comprises of two excitonic transitions, A and B, at energies between 1.1 and 2.4 eV, originating from the transition between the spin–orbit split VBM (indicated in Fig. 2d by magenta circles) and doubly degenerate CBM at the K (K′) point, and further transitions are observed at higher energies (2.5–4.8 eV) [39,66,72–74]. The size of the A–B energy splitting increases with the increasing size of M and X (Table 4) due to a greater overlap between the outer orbitals of larger atoms [73,74]. 1T′-WTe_2 is an exception to this due to its perfectly-compensated semimetallic character with a small overlap between the W 5*d* and Te 5*p* orbitals due to the distorted octahedral coordination discussed earlier [43,75].

Table 4
A and *B* exciton energies in bulk TMDCs.

2D material	Bulk exciton energies (eV)		
	A	B	ΔA–B
2H-MoS_2	1.88	2.06	0.18
2H-$MoSe_2$	1.57	1.82	0.25
2H-$MoTe_2$	1.10	1.48	0.38
2H-WS_2	1.96	2.36	0.40
2H-WSe_2	1.62	2.19	0.57

Data collected from the following references: [43,72,74,165].

The absorption spectrum of TMDCs is well matched to the solar spectrum and more than 95% of the sunlight is absorbed in even polycrystalline films of sub-micrometre thickness, much thinner than the current photovoltaics standard [76]. Theoretical calculations and experiments indicate that a monolayer TMDC crystal can absorb ~5–10% of sunlight, corresponding to as much as 50 nm Si or 15 nm GaAs, and are able to generate about ten times higher photocurrent [25]. However, due to the complex electronic band structure of TMDCs, their absorption/reflectance is strongly dependent on the wavelength of the incident light [73,74,77], as demonstrated by the differential reflectance spectra in Fig. 2f. In contrast, monolayer graphene only absorbs ~2.3% of light, a value, solely defined by the coupling between light and the relativistic-like electrons in graphene, and independent of wavelength in the visible range [78]. The wavelength-specific transmission/absorption scales linearly with the number of layers for most thin 2D materials but this proportionality breaks down in thick crystals [63,78]. The absorption coefficient between the IR and near-UV is typically on the order of ~10^4–10^6 cm^{-1} [70,72–74,77,79] and is generally higher for the W-based than Mo-based TMDCs [73,74]. Furthermore, the equivalent absorption coefficients of monolayer MoS_2 and graphene are 2–3 times higher than that of the bulk crystals [25].

Mechanical properties of 2D materials have also been studied extensively. Monolayer MoS_2 withstands strain up to 11%, deformations up to several tens of nm without breaking, and has Young's modulus similar to that of steel, as found by the atomic force microscopy (AFM) measurement on crystals suspended over holes in an SiO_2 substrate, shown in Fig. 2g and h [80,81]. Such strength and elasticity makes it suitable for applications where sturdiness as well as flexibility is required. Ripples and wrinkles, which are known to form in 2D materials due to the localised strain and differing thermal expansion coefficient of the 2D material and substrate, were predicted to grow in size with temperature and decrease the size of the band gap in MoS_2 [82]. These ripples have typical height of 1–25 nm, periodicity of 40–300 nm, and have been shown to correlate with changes in the surface potential and charge [83]. Strong, thickness-dependent piezoelectricity, for the odd number of layers only, was observed in mono- and few-layer MoS_2 with the strongest effect and ~5% mechanical-to-electrical energy conversion efficiency observed in monolayer [84]. Frictional properties of MoS_2 in relation to surface oxidation, moisture, and temperature have been studied extensively because of its use as a lubricant [85]. The melting temperature of most 2D crystals generally decreases with the decreasing thickness, and, while sulphides and selenides tend to be thermodynamically stable, tellurides (and most metallic) TMDCs are not [14,86].

2.3. Preparation methods

Graphite, molybdenite (MoS_2), and mica are the most common layered crystals found naturally in appreciable quantities and high quality at multiple locations worldwide (Fig. 4a). These minerals typically contain small amounts of bulk impurities (~1 at% or less), and their surface is slightly oxidised [79,87–89]. Two distinct approaches exist for the preparation of 2D materials: a top-down exfoliation of bulk layered crystals and bottom-up synthesis from molecular precursors.

Mechanical exfoliation (ME) is a top-down preparation method of mono- or few-layer 2D materials from either natural or synthetic bulk crystals. Thin layers of MoS_2 (3–10 nm) were isolated by ME as early as 1960s [79,90,91]. The simple method of "peeling" or "cleaving" the bulk crystals using an adhesive tape or 'rubbing' bulk crystals against a solid surface, schematically shown in Fig. 4b, remains principally unchanged [6,9], and only minor modifications have been adopted to maximise the adhesion forces between

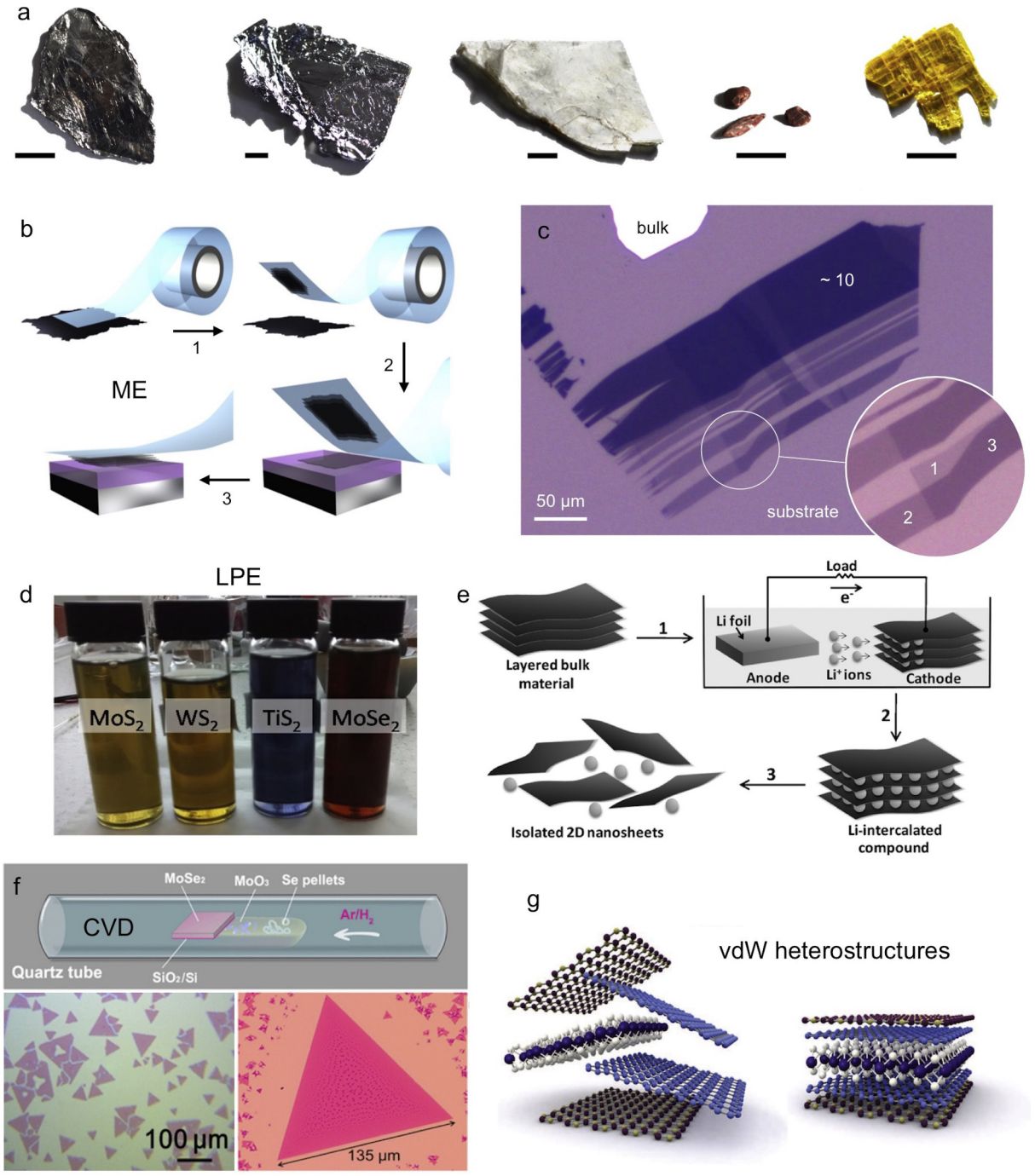

Fig. 4. Preparation of 2D materials. a, Photographs of (left-to-right) graphite, molybdenite (MoS_2), muscovite (mica), GaSe, and orpiment (As_2S_3) from the authors' collection. All crystals except GaSe were mined naturally, all scale bars correspond to 0.5 cm. b, ME of 2D materials using an adhesive tape and suitable substrate. c, Optical image of ME graphene/graphite crystals on an SiO_2/Si substrate, numerals indicate the number of graphene layers. d, Dispersions of various 2D materials in an organic solvent (NMP). e, Electrochemical exfoliation based on Li^+ intercalation into the bulk layered structure of TMDCs. f, top-panel: CVD growth of $MoSe_2$ crystals, bottom-left panel: nucleation of multiple $MoSe_2$ single crystals, bottom-right panel: large single crystal of monolayer $MoSe_2$. g, Construction of vdW heterostructures from individual 2D materials. Images in a, photographed by Julia Velický. Figures adapted with permission from: b, [135] © The Royal Swedish Academy of Sciences, reproduced by permission of IOP Publishing, all rights reserved. d, [97] published by Elsevier under CC-BY licence. e, [107] © 2011 John Wiley and Sons. f, [117] © 2013 American Chemical Society. g, [22] © 2016 The American Association for the Advancement of Science.

the crystal and substrate [51,92]. This technique produces a very clean, high quality basal surface suitable for fundamental research (Fig. 4c), and, when optimised, crystals with lateral dimensions of 0.1–1 mm can be made [1,13,93]. Crucially, virtually all the novel properties of 2D materials were discovered using ME crystals and, as such, it remains one the most important preparation techniques.

Ultrasonication-assisted liquid-phase exfoliation (LPE) has become a very popular top-down method for production of large quantities of thin 2D nanosheets dispersed in a solvent (Fig. 4d), following the pioneering work of Coleman's group [94–96]. It is based on forcible breaking of the vdW forces between the individual layers in a solvent whose surface energy matches well that of the 2D material. Most popular solvent, which is universal to exfoliation of

graphene and most TMDCs is *N*-methyl-pyrrolidone (NMP), other solvents such as N,N-dimethylacetamide, acetone, or isopropanol (IPA) were also used [94–98]. NMP potentially has a protective role against surface oxidation as recently suggested [97]. LPE was also successfully applied to produce the unstable 2D material phosphorene [99] and ~10 g quantities were achieved using benzonitrile under inert atmosphere [100]. Centrifugation is an effective way of selective separation of populations of 2D nanosheets with a certain lateral size and the typical LPE production times vary between 2 and 6 h.

Lithium intercalation of *n*-butyllithium and other organometallic compounds in organic solvents (typically hexane) into the group 4 and 6 TMDCs, and the subsequent reaction with water leading to hydrogen gas evolution, is an effective top-down exfoliation technique [101–103], which also alters the 2H to 1T phase [41]. This method requires a long time (days) and results in 2D nanosheets of a small lateral size. A derived method based on an expansion by thermal decomposition of hydrazine, intercalation using alkali-metal naphthalenides, and subsequent LPE was also successfully applied to a range of TMDCs and produced monolayer MoS_2 nanosheets with an impressive 10–30 μm lateral size [104].

Electrochemical methods have also been successfully applied to the liquid-based top-down exfoliation of 2D materials after the early success for graphene [105,106]. Electrochemical lithiation using a $LiPF_6$ in ethyl/dimethyl carbonate mixture followed by LPE (Fig. 4e) works well for exfoliation of several TMDCs, with an outstanding 92% yield of monolayer MoS_2 [107]. Liu et al. prepared large monolayer MoS_2 flakes up to 50 μm in lateral size by ultrasonication-free electrochemical oxidation of an aqueous solution of Na_2SO_4 at +10 V, with typical production times of 0.5–2 h [108]. Similar method based on an alternating anodic and cathodic DC voltage was recently demonstrated for exfoliation of topological insulators Bi_2Se_3 and Bi_2Te_3 [109].

The advantages of the solution-based exfoliation techniques (LPE, Li^+ intercalation, and electrochemistry) are the scalability and compatibility with the existing technologies such as inkjet printing, filtration, and centrifugation [22,97,104,110]. The disadvantages include limited control over the flake dimensions, unintentional chemical functionalisation, need for removal of the solvent or surfactant molecules, and restacking or agglomeration. Although these methods are not suitable for fundamental electrical, optical, or electrochemical measurements, they are a perfect match for applications in catalysis, supercapacitors, or sensors, where the compromised material quality is not an issue [111,112]. Laser ablation of bulk crystals is an example of a less common top-down method [93].

Chemical vapour deposition (CVD) is a very popular and fast-developing method for the bottom-up synthesis of graphene and TMDCs, with typical growth times of 10–20 min. Lateral size of the single crystal domains can reach more than 100 μm (Fig. 4f) and the overall substrate (typically SiO_2) coverage is limited only by the size of the active zone within the CVD furnace [113–115]. The method relies on a reaction between two molecular precursors in a vaporised state at high temperature (typically 700–900 °C). In the case of MoS_2, this is done by vaporising MoO_3 and S precursors under Ar or N_2 gas flow [51,116], preferably in a two-zone furnace for a separate temperature control of the two precursors [113]. A reducing hydrogen atmosphere has also been proven crucial for certain TMDCs [117]. Alternatively, thin layers of metal oxide, deposited on a substrate by vacuum thermal evaporation, are exposed to chalcogenide vapour and are let to react to form the desired material [118,119]. CVD crystals of TMDCs assume typical triangular shapes (Fig. 4f), either inherent to the TMDC crystallisation or adopted from the parent metal oxide crystals. Careful control of the nucleation rate, precursor concentration, substrate-treatment, and gas flow leads to large area single crystals of good quality and reproducible thickness [51,120–122]. Edge-terminated vertically-aligned MoS_2 and $MoSe_2$ nanosheets have also been grown on various substrates by sulfurisation and selenisation of Mo, respectively [123,124]. CVD is often thought to be the second best after ME in terms of the crystal quality and has the advantage of scalability and better control over thickness and size of the 2D crystals than other methods. It is also suitable for the in situ growth of lateral 2D heterostructures, as shown in Fig. 5e and f [13,121].

Chemical vapour transport (CVT), which is an artificial equivalent of geological mineral growth, is a related bottom-up method popular for growth or recrystallisation of bulk single crystals of TMDCs. It is based on a reaction between precursors compounds followed by transport using a halogen gas and re-crystallisation in a dual zone temperature-gradient glass or quartz tube [46,125,126]. Related Bridgman–Stockbarger method is used for synthesis of less common chalcogenides such as InSe or GaSe [127,128].

Epitaxial growth is popular for growing elemental 2D materials including graphene [129], silicene [130], germanene [131], stanene [132], vdW and lateral heterostructures [22], and 2D materials which do not normally form layered structures [13]. The crystallographic orientation of an epitaxial film is determined by the choice of substrate, typically Si(111), Ag(111), Au(111), or other layered materials. For example, an epitaxial film of mono- and few-layer stanene nano-islands with an average lateral size of 5 nm and surface coverage of ~90% were produced on a Bi_2Te_3(111) substrate [132].

Other bottom-up methods include a direct synthesis of TMDCs using stoichiometric mixtures of constituent elements at high temperature and low pressure [42,133], hydrothermal (or solvothermal) synthesis of MoS_2 from the aqueous solutions of ammonium molybdate and thiourea precursors at high temperature and pressure [2,13], or "flux" synthesis of 1T′-$MoTe_2$ based on mixing of a stoichiometric ratio of Mo and Te powders in liquid NaCl under vacuum at 1100 °C [134].

Transfer methods of 2D materials enable the use of an arbitrary target substrate, encapsulation of 2D materials in protective layers, or construction of vdW heterostructures, shown schematically in Fig. 4g [14,135–137]. Both wet transfer using a sacrificial membrane or dry "pick-and-lift" transfer techniques rely on the use of polymers, alignment of the 2D flakes, and use of adhesion forces between different 2D materials [27,52,93]. Vacuum or inert gas annealing of 2D materials and their heterostructures at elevated temperatures is very common way of obtaining pristine surfaces and interface with minimum contamination [138,139].

2.4. Characterisation techniques

A range of experimental techniques can be used to determine the structure, number of layers, chemical composition, and electrical, optical, and mechanical properties of 2D materials. These include optical, scanning probe, and electron microscopy, X-ray diffraction, X-ray photoelectron microscopy (XPS), electronic transport measurement, electrochemistry, Raman and PL spectroscopy, and UV–vis spectroscopy.

Optical visualisation and imaging of 2D materials on suitable substrates still remains one of the most popular ways of rapid identification of thin crystals. The wavelength-dependent contrast between monolayer graphene and an SiO_2/Si substrate reaches 10% for green light and 90/280 nm thick SiO_2 [140]. Hence monolayer flakes of large enough lateral dimensions (>1–2 μm) are easily detectable using a standard optical microscope as shown in Fig. 4c. Contrast of most TMDCs reaches 40% on similar substrates [141,142]. The absorption/transmission and therefore the apparent colour of 2D crystals is also thickness- and wavelength-dependent [79], and provides an additional optical aid. Interestingly, the termi-

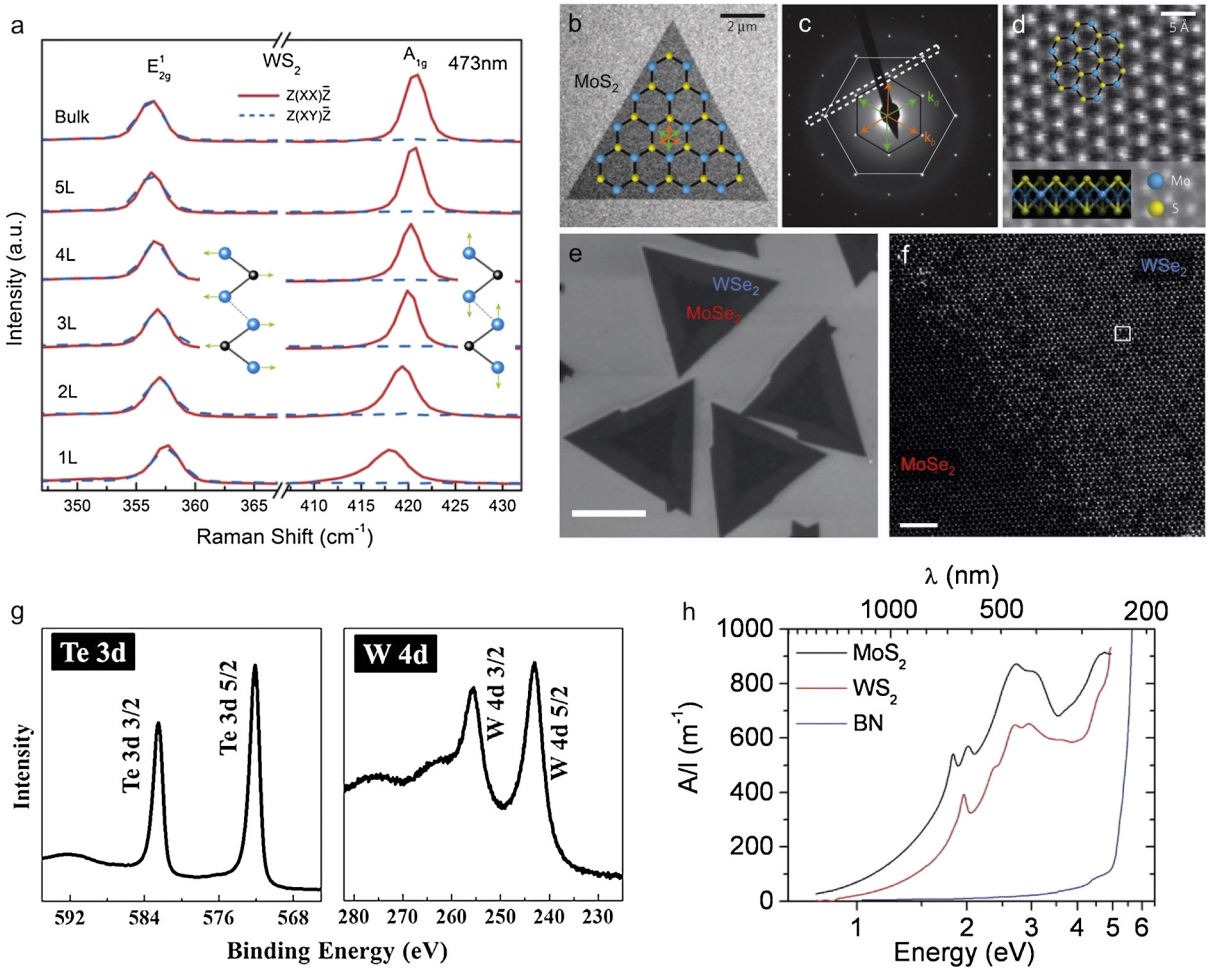

Fig. 5. Characterisation of 2D materials. a, Evolution of WS_2 Raman spectra with the number of layers using polarised 473 nm excitation, the inset schematics shows the vibrations of the E^1_{2g} and A_{1g} modes (left and right, respectively). b, Bright-field TEM image of a monolayer MoS_2 crystal with Mo-atom termination at the edge. c, diffraction pattern from b. d, Atomic-resolution ADF-STEM of monolayer MoS_2. e, SEM image of lateral heterostructures of monolayer MoS_2 and WSe_2. f, Atomic-resolution ADF-STEM of the MoS_2/WSe_2 heterostructure interface. g, High-resolution XPS spectra of the Te 3*d* (left) and W 4*d* (right) spectral regions of 1T′-WTe_2. h, Absorbance spectra of 2D nanosheets dispersions in NMP (MoS_2 and WS_2) and IPA (hBN) prepared by LPE. Figures adapted with permission from: a, [157] © 2013 The Royal Society of Chemistry. b–d, [115] © 2013 Nature Publishing Group. e–f, [181] © 2014 Nature Publishing Group. g, [44] published by Nature Publishing Group under CC-BY licence. h, [94] © 2011 The American Association for the Advancement of Science.

nation of triangular CVD crystals of MoS_2 (Fig. 5b) can be predicted from the shape of the crystal edge [115].

AFM is indispensable in determining the number of layers of 2D materials, especially for few-layer and thicker crystals (Fig. 2g). The step-height between a 2D surface and substrate is often 0.2–1 nm higher than expected due to the adsorption of ubiquitous organic molecules, water, surface oxidation, or interactions between the substrate and crystal, and the step-height measurement between different 2D layers is more reliable [143–148]. Other scanning probe microscopy techniques such as electrostatic force microscopy, ultrasonic force microscopy, Kelvin probe force microscopy, scanning tunnelling microscopy (STM), and scanning tunnelling spectroscopy (STS) are used to study the surface potential, charge distribution, and band structure in 2D materials [83,149–151], exemplified by Fig. 12.

Raman spectroscopy is a very powerful and rapid characterisation technique, which has successfully been applied to graphene and other 2D materials [143,152,153]. The two main active Raman modes in 2D materials, E^1_{2g} and A_{1g}, which correspond to the symmetric in-plane and out-of-plane vibrations lattice vibrations, respectively [133,154], strongly depend on the number of layers and can be selectively "switched on/off" using polarisation, as demonstrated in Figs. 5a and 17c. The A_{1g} mode softens (redshifts) with the decreasing number of layers due to the weakening of the restoring forces acting upon vibrations in few-layer MoS_2, $MoSe_2$, $MoTe_2$, and WS_2, whereas the E^1_{2g} mode stiffens (blueshifts) with the decreasing thickness, which is counterintuitive and indicative of additional interlayer interactions or a dependence of the intralayer bonding on thickness [69,143,155–158]. Raman spectrum of WSe_2 follows the same thickness-dependence trends but degeneracy is observed in monolayer and few-layer crystals [157]. The observed Raman shifts decrease with the increasing molecular weight of MX_2. The additional B^1_{2g} mode observed in group 6 selenides and tellurides corresponds to the asymmetric out-of-plane vibrations due to the symmetry breaking along the *c*-axis and can also be used to determine the number of layers [69,86,156,159]. The Raman spectra of group 6 semiconducting TMDCs show additional resonant modes, which appear when the excitation energy is close to the direct band gap transitions at the K (K′) point [29,133,157,160]. Furthermore, at low excitation energies the Raman spectrum also overlaps with the PL emission. Therefore, "off-resonance" laser excitation wavelengths, e.g. 514 and 532 nm for MoS_2 or 473 and 488 nm for WS_2 are preferred for a straightforward Raman characterisation. Group 4 TMDCs show no resonant Raman scattering [133]. The Raman spectra of other less common 2D materials such as phosphorene [99,144] or 1T′-PtS_2 [161] also

strongly depend on the number of layers (Fig. 17c). Finally, the Raman mode frequencies of some 2D materials such as 1T-HfS_2, 1T′-ReS_2, or 4H-SnS_2, do not depend on their thickness, indicating only weak electronic coupling between the individual layers [162–164].

The PL originating from the direct band gap transition (A exciton) at the K (K′) point in group 6 monolayer TMDCs is observed in all thicknesses but it is ∼2–3 orders of magnitude more intense in monolayer than in bulk due to the direct-indirect band gap transition discussed above (see Table 3 and Fig. 2c). The A exciton PL energy only slightly blueshifts (20–50 meV) with decreasing thickness, in comparison to the large blueshifts (340–380 meV) of the PL originating from the indirect band gap transition (Fig. 2b), indicating strong and weak interlayer coupling for the indirect and direct transition, respectively [63,69,90,165]. The W-based TMDCs generally have about an order of magnitude higher PL than the Mo-based ones. The shape and intensity of the PL spectra varies substantially due to the 2D material–substrate interactions [69,146,150], temperature [148], defect density [56,166], and surrounding media [167].

Both Raman and PL spectra intensities of mono- and few-layer 2D materials depend strongly on their thickness, identity of the substrate, and external strain and doping [83,168–172]. A strong enhancement is observed in few-layers, in comparison to monolayer and bulk, which originates from the optical interference effect in the multi-interface 2D material/SiO_2/Si system [98,143,147]. Raman spectrum of MoS_2 is sensitive to defects and crystallinity, albeit at high defect densities, as demonstrated by comparing the edge and basal surface [173], bombardment of monolayer MoS_2 by manganese ions [174] and growth of edge-terminated vertically-aligned MoS_2 [123,175].

Electron microscopy and diffraction techniques are routinely used for 2D materials characterisation as shown in Fig. 5b–f. These include electron diffraction, scanning electron microscopy (SEM), transmission electron microscopy (TEM) and annular dark-field (ADF) or high-angle annular dark-field (HAADF) scanning transmission electron microscopy (STEM), often combined with the energy-dispersive X-ray spectroscopy (EDXS). Despite their low-throughput, these methods are powerful for examination of atomic defects, grain boundaries, edge termination, and bonding in 2D materials [115,176–180], determination of the stacking sequence in TMDCs [158], or quantum dot phase engineering in monolayer MoS_2 [40]. High-resolution HAADF-STEM is especially useful for characterisation of lateral heterostructures (Fig. 5e and f) [121,181] and vertical vdW heterostructures in conjunction with cross-sectional analysis using focused-ion beam and electron energy loss spectroscopy [27,139].

XPS is a surface-sensitive technique, useful for the determination of the chemical composition of a 2D material (Fig. 5g), including the oxidation states of the elements [109,182–184]. It has also been used to determine the type of doping in MoS_2 [185] and VBM energy in tin sulphides [184]. XPS is particularly useful in quantification of 2D materials ageing through adsorption of impurities and surface oxidation [44,87,89], and defect density [173], as shown in Figs. 11c and 14d.

Other characterisation techniques also deserve a brief acknowledgement. UV–vis absorption spectroscopy (Fig. 5h) is used for the observation of excitonic transitions in the TMDCs spectra [51,94,97], determination of the band gap using the Tauc plot [186], and quantification of LPE 2D nanosheets' concentration [94]. Dynamic light scattering is used to determine the lateral size of 2D nanosheets in liquids [187]. X-ray diffraction is crucial in determining the crystal structure [44,187] and interlayer spacing of 2D materials, especially in intercalation experiments [104]. Fourier transform infrared spectroscopy (FTIR) and ellipsometry can identify thin contamination films on graphene, graphite, and MoS_2 [188,189]. Advances in determination and imaging of the electronic band structure using angle-resolved photoemission spectroscopy have been crucial for fundamental understanding of 2D materials, heterostructures, and some exotic properties [2,43]. Theoretical and computational approaches such as density functional theory (DFT) are invaluable in determining the electronic band structure of 2D materials and its dependence on factors such as number of layers, electric field, or strain [98,138,190,191], or the assignment of vibrational modes in Raman spectra [44]. Molecular dynamics simulations are a powerful tool to predict the interactions between 2D materials and liquids [192–195]. Electronic transport measurements are used to study the carrier transport and conductivity/resistivity behaviour [6,33,144]. Finally, electrochemical techniques, which will be the focus of the following chapters, assess the rate of electron transfer, capacitance, catalytic activity, or adsorption [146,173,196].

3. Electrochemistry of 2D materials

3.1. Basic concepts

Here, we review basic electrochemical concepts necessary to grasp the content of the following chapters. The arbitrary standard hydrogen electrode (SHE) potential scale used by electrochemists is shifted by −4.4 eV in respect to the absolute energy scale, on which zero is defined as the energy of an electron at rest in vacuum, as shown in Fig. 6a [197]. The potential (voltage) has the opposite "polarity" to the electron energy, so that e.g. an increase in potential corresponds to a decrease in energy. The electrochemical performance of a solid electrode is generally assessed by two key parameters, which are intimately linked to the electronic structure of the solid and properties of the surrounding liquid medium. These are the heterogeneous electron transfer (HET) rate (k^0) between the electrode and a molecule dissolved in the liquid (Fig. 6b), and the interfacial capacitance arising from the electric double-layer, established at the electrode/liquid interface due to the potential drop (Fig. 6c) [198]. Model redox mediators such as $[Ru(NH_3)_6]^{3+/2+}$ or $[Fe(CN)_6]^{3-/4-}$, i.e. molecules that can be both reduced and oxidised depending on the relative positions of their standard redox potential, E^0_{redox}, and the electrode Fermi level, E_F, are used to determine the HET. However, k^0 is always specific to a given redox reaction and should be assessed that way. In particular, inner-sphere redox mediators are (unlike the outer-sphere ones) sensitive to the electrode material and its surface chemical states [198]. Knowledge of the HET is essential for operation of batteries: the higher the k^0, the faster and more effective the battery performance. The interfacial capacitance describes the energy stored at the electrode/liquid interface and its knowledge is crucial for supercapacitors, which are devices with high power density, excellent stability during prolonged cycling, but low energy density. Battery-supercapacitor hybrid systems thus could be the future electrochemical energy storage solutions exploiting the fast charging of a supercapacitor and the high energy density of a battery. It is worth realising that while the HET is size-independent, the interfacial capacitance scales with the electroactive area of an electrode. Furthermore, slow charge carrier transport in bulk crystals at low mobilities ($<1\ cm^2\ V^{-1}\ s^{-1}$) can be limiting factor in electrochemical studies. 2D materials are uniquely suited for fundamental and applied electrochemical studies: due to the extreme thinness, their surface area is extremely large and the potential drop at the solid/liquid interface is "felt throughout the 2D interior" as well.

Most common electrochemical techniques employed to study the electrochemical properties are based on measurement of three variables: current, potential, and time. These include voltammetry, chronoamperometry, electrochemical impedance

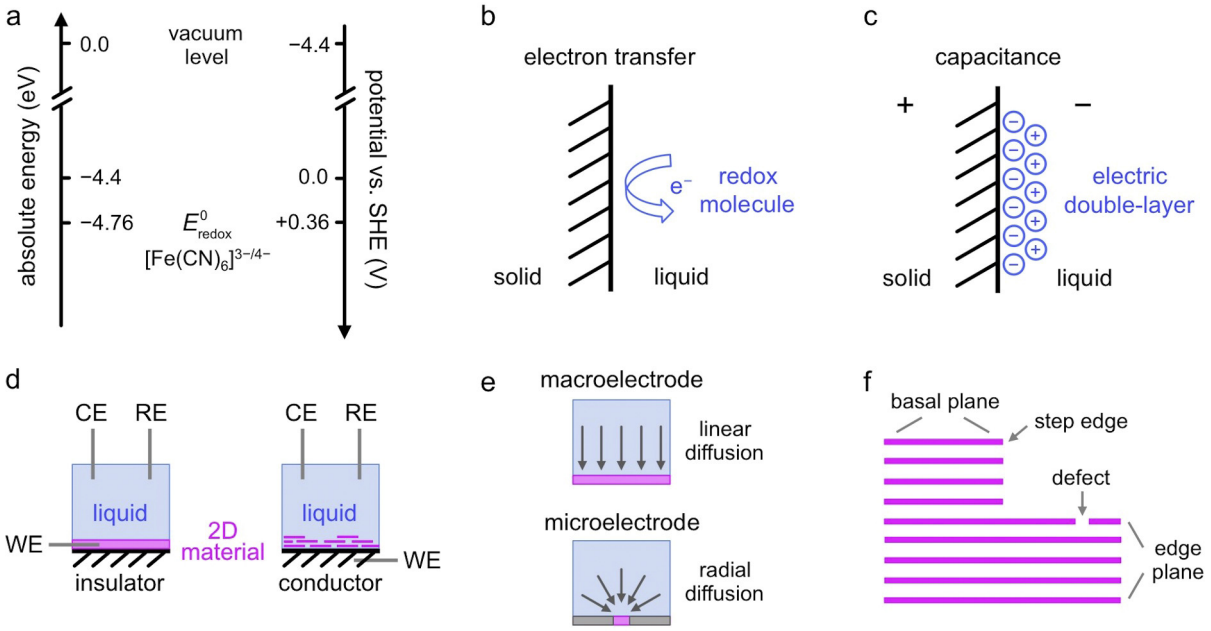

Fig. 6. Basic concepts in electrochemistry. a, Comparison of the absolute energy scale used in condensed matter physics with the SHE potential scale commonly used in electrochemistry. b, Schematic of the HET between a redox molecule (in liquid) and a solid electrode. c, Schematic of the electric double-layer giving rise to an interfacial capacitance. d, Two most common configurations for electrochemical characterisation of 2D materials. Left: 2D material on an insulating substrate is contacted directly, typical for ME and CVD crystals; right: 2D material is placed directly on a conducting underlying substrate, typical for LPE crystals. e, Two most common electrode geometry configurations. Top: macroelectrode resulting in linear diffusion in the liquid; bottom: microelectrode resulting in radial diffusion in the liquid. f, Description of the different surface types of layered and 2D materials.

spectroscopy, and scanning electrochemical microscopy [198]. Static, diffusion-limited measurements are a standard but hydrodynamic voltammetry using rotating-disc electrode has been also successfully applied for electrochemical studies of MoS_2 [199–201]. Two approaches are typically employed to fabricate electrodes from 2D materials: in first, the 2D material is placed on an insulating substrate and contacted directly (left of Fig. 6d); in second, the 2D material is placed on a conducting substrate, which itself acts as a contact (right of Fig. 6d). Both macro- and micro-electrode geometries can be used (Fig. 6e), the latter offering significant advantages in 2D materials' electrochemistry. The vdW surface of 2D materials perpendicular to the *c*-axis is referred to as the basal plane, the surface parallel to the *c*-axis is called the edge plane (Fig. 6f). Unlike in condensed matter physics measurements, where two electrode terminals are usually used, another, so called reference electrode (RE) is used in electrochemistry for an exact assignment of the applied potential on the SHE scale (Fig. 6d). Furthermore, in condensed matter physics experiments, the voltage is usually applied with respect to the gate electrode (equivalent of the counter electrode (CE) in electrochemistry). This is why changes in voltage directly correspond to changes in energy at the working electrode (WE), e.g. a positive change in voltage at the gate electrode corresponds to a positive change in energy at WE. This is exactly opposite to electrochemistry where potential (voltage) is applied directly to WE.

3.2. Semiconductor electrochemistry

Since the focus of this review is on semiconducting 2D materials, basic concepts of semiconductor electrochemistry will now be reviewed [202,203]. Electrons are the only effective charge carriers in metals but both electrons and holes contribute to conductivity in semiconductors. The Fermi level lies exactly in the middle of a band gap (E_g) in ideal intrinsic semiconductors leading to similar electron and hole concentrations (Fig. 7a). On the other hand, extrinsic semiconductors have majority and minority carriers, and the E_F is shifted accordingly due to the altered distribution of the electrons and holes. In n-type semiconductors, electrons are the majority carriers and the E_F lies just under the CBM (Fig. 7b) due to the presence of donor states, while in p-type semiconductors, holes are the majority carriers and the E_F lies just above the VBM (Fig. 7c) due to the presence of acceptor states. Another difference between metals and semiconductors is the voltage drop across the solid/liquid interface. In metals, this drop is very sharp and is confined within a few Å of the Helmholtz electric double-layer at the interface. In semiconductors, the space charge (SC) region with an in-built electric field (ΔE_{SC}) arises near the interface. This is due to the depletion of charge carriers in the semiconductor after equilibrium has been established through a charge transfer between the solid and liquid phase (Fig. 7d and e). This in turn leads to band bending (Fig. 7e), which has an opposite direction for n- and p-doped semiconductors. Only the donor (n-type) or acceptor (p-type) impurities contribute to the depletion, and the SC region can extend to 10–1000 nm inside the semiconductor. 2D semiconductors are very unique in this aspect because their thickness is several orders or magnitude smaller than the SC region width in conventional bulk semiconductors, which could provide new insights into these interfacial phenomena. The semiconductor-liquid interface is analogous to the rectifying Schottky barrier at metal-semiconductor solid interface, further discussed below.

We now proceed to outline the current-potential electrochemical behaviour of an n-type semiconductor. Under the so-called forward bias, the majority carriers are accumulated in the SC region (Fig. 7f), band bending is reversed, and a reductive cathodic current flows. This current is potential-dependent because it corresponds to the flow of electrons from the potential-dependent E_F in the semiconductor CB to the vacant states of the redox species in the liquid. The cathodic current is therefore same in dark as under illumination (Fig. 7h) and it is governed entirely by majority carriers, in this case electrons. On the other hand, under the so-called reverse bias, the majority carriers are depleted in the SC region (Fig. 7g), band bending is enhanced, and an anodic current flows. This current

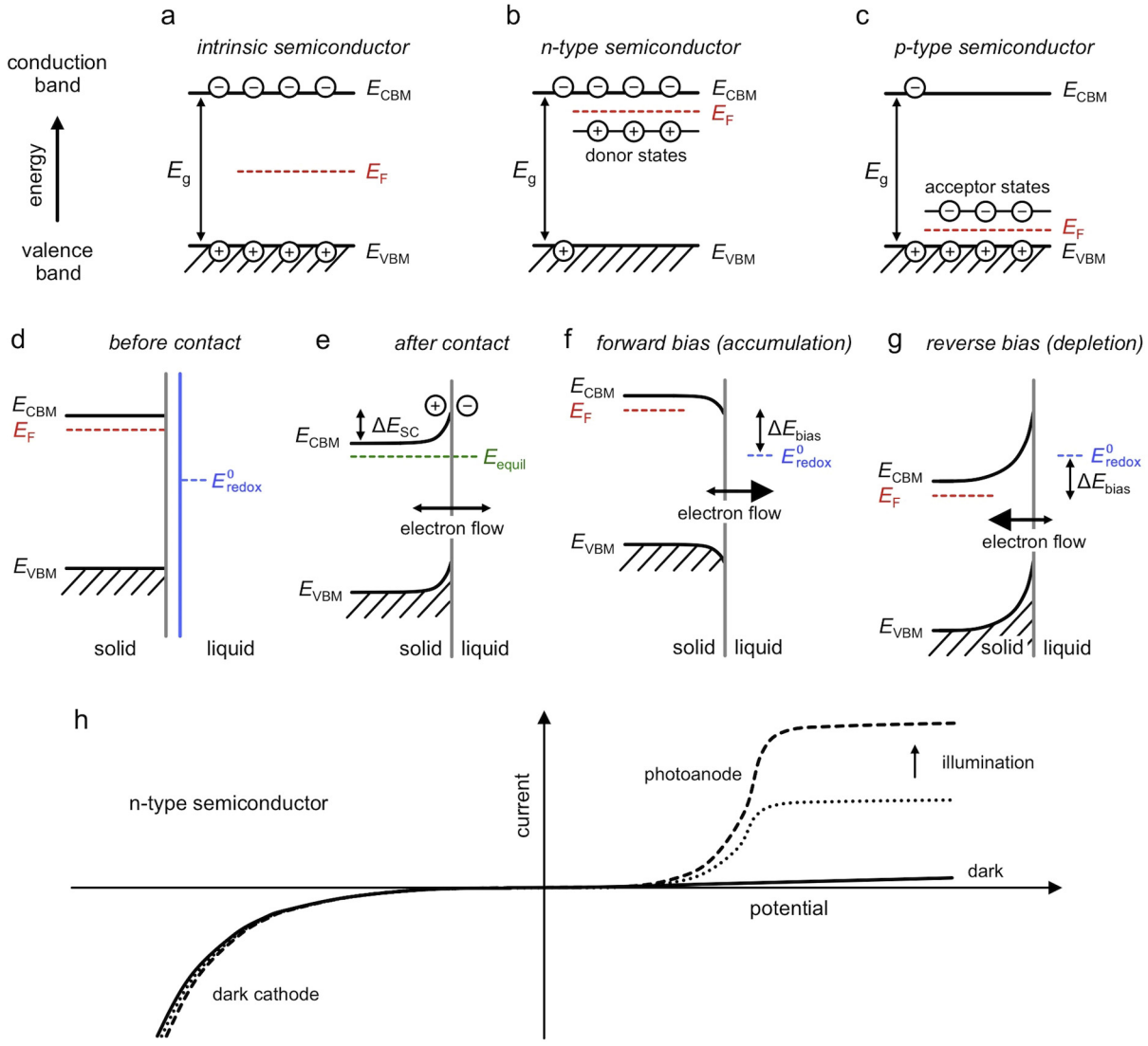

Fig. 7. Basic concepts in semiconductor electrochemistry. a–c, Schematic band diagrams of an intrinsic, n-type, and p-type semiconductor, respectively. d, Differing energy levels in an n-type semiconductor (E_F) and a liquid containing a redox mediator (E^0_{redox}) before their contact. e, After contact, an equilibrium energy level (E_{equil}) is established across both the phases (E^0_{redox} energy $< E_{equil} < E_F$) by the transfer of electrons from the donor states of the semiconductor to the unoccupied states of the redox mediator. Related majority charge carrier (electron) depletion results in a SC region of electric field gradient with the corresponding energy difference ΔE_{SC} and corresponding band structure bending near the semiconductor/liquid interface. f, n-type semiconductor under a forward bias voltage (ΔE_{bias}), where E_F is raised sufficiently to overcome the band bending and majority carrier accumulation occurs. g, n-type semiconductor under a reverse bias, where E_F is pushed lower, accentuating the majority carrier depletion and the extent of band bending. h, Characteristic current-voltage curve of an n-type semiconductor in dark and under illumination, with the potential-dependent cathodic and illumination-dependent anodic response.

reaches a potential-independent plateau because it corresponds to the flow of electrons from the "fixed" occupied states of the redox species to the CB of the semiconductor. The anodic photocurrent depends strongly on illumination (Fig. 7h) and is governed by minority carriers, in this case holes, and their diffusion from within a certain distance in the SC region, beyond which they recombine [204]. The anodic current is also proportional to the excitation energy and photon flux [146,204], as shown in Figs. 8b and 10a , respectively. Same trends of opposite directions involving VB instead of CB apply to a p-type semiconductor. Surface states can mediate the charge transfer or lead to E_F pinning, thus altering the idealised processes described above [8,65]. Because the position of the band edge at the interface is independent of the applied voltage (Fig. 7e–g), the direction and extent of the band bending can be tuned externally by applied potential. The above discussion describes direct injection of charge carriers from and to a semiconductor but other mechanisms such as photo-sensitised charge injection and photo-induced charge transfer are also important in photoelectrochemistry and photovoltaics [205,206]. Finally, note that so called flatband potential, corresponding to the E_F at which there is no band bending, can be measured from the Mott–Schottky relationship between the capacitance and potential [203,207,208].

The collection rate of photogenerated charge carriers depends on multitude of factors: carrier diffusion (itself a function of mobility, temperature, and life-time), carrier recombination (direct or via surface states or charge impurities), depletion layer thickness, light penetration depth, electron transfer, and redox mediator concentration. The carrier recombination, which reduces their lifetime is particularly important in 2D materials because of the quantum confinement and the Coulombic screening effects discussed in the previous chapters. The light penetration depths range significantly depending on the material, wavelength and nature of the electronic transition. Anodic (or cathodic) photocorrosion of a semiconductor can occur when the E^0_{redox} of the semiconductor decomposition

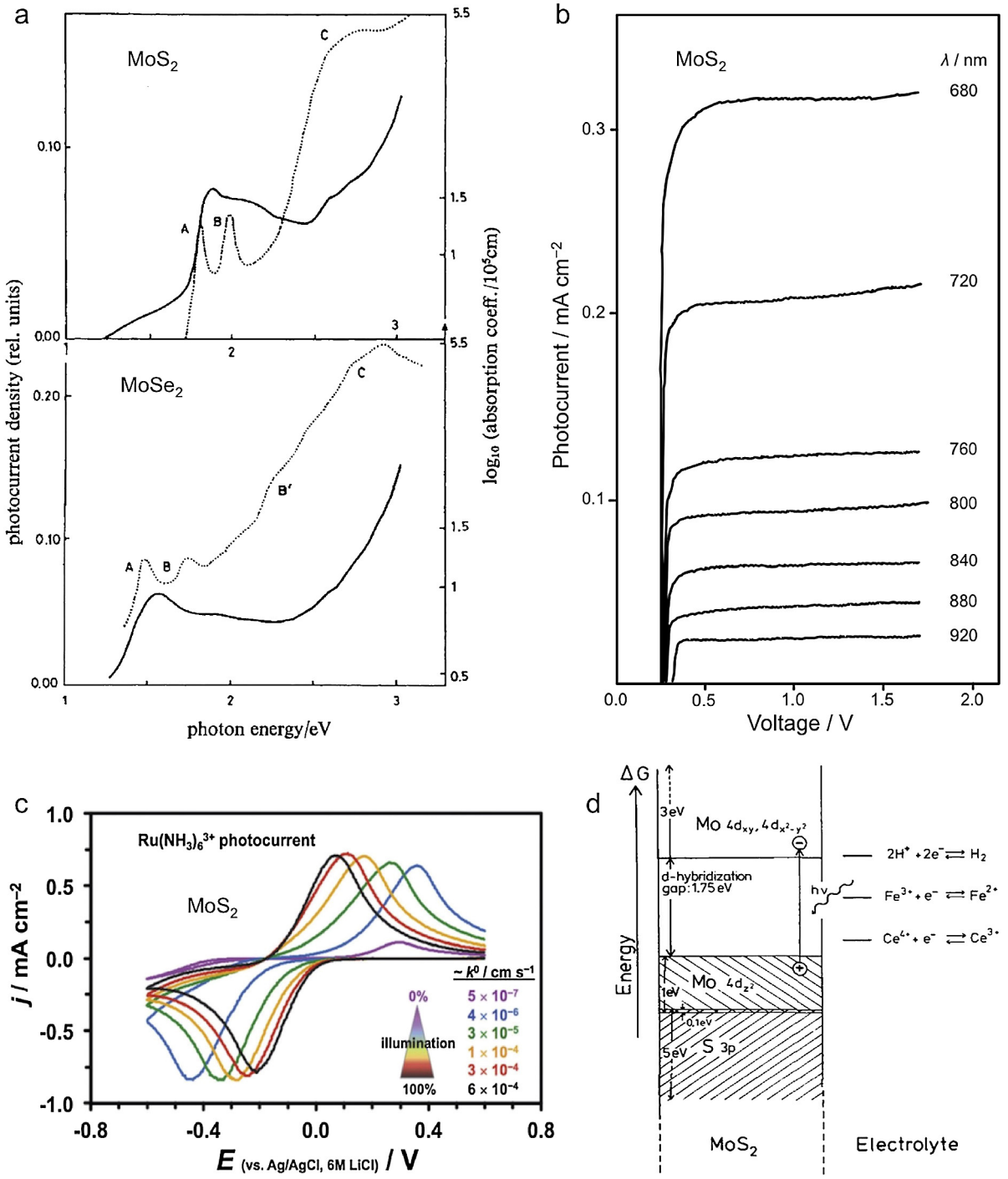

Fig. 8. Photoelectrochemistry of layered TMDCs. a, Graphs showing the correlation between the anodic photocurrent (solid curves) and absorption spectra (dotted curves) in n-MoS_2 (top) and n-$MoSe_2$ (bottom) using K_2SO_4 electrolyte at pH 1. b, Dependence of the n-MoS_2 anodic photocurrent on the excitation wavelength using KI redox meditator in KCl electrolyte at pH 1. c, Tuning of the effective HET rate (k^0) of $[Ru(NH_3)_6]^{3+/2+}$ reduction/oxidation on n-MoS_2 by illumination. d, Schematic diagram relating the band structure of MoS_2 with several redox reactions. Figures adapted with permission from: a, [217] © 1969 The Royal Society of Chemistry. c, [87] published by the PCCP Owner Societies under CC-BY licence. d, [3] © 1977 Elsevier. b, schematically re-drawn based on Fig. 1a in [204].

reaction is higher (or lower) on the energy scale than the VBM (or CBM) [209]. This is more pronounced when the band bending is large and the oxidising holes (or reducing electrons) remain at semiconductor's surface. In the case of a small band bending, the charge carriers recombine and do not contribute to anodic oxidation (or cathodic reduction) of the semiconductor. Photocorrosion of a semiconductor also depends on the reaction kinetics of all the processes involved, stability of the corrosion products, and presence of the mid-gap surface states [210].

It should now be clear that relative positions of the VBM, CBM, and E^0_{redox} determine whether the charge transfer to/from the semiconductor is feasible. However, it is worth pointing out that an efficient electron transfer only occurs when the energy of the semiconductor and redox states are approximately of the same energy, and although a higher overpotential should provide higher reducing/oxidising power, it will in fact result in slower electron transfer due to the so-called inverted region effect described for intra-molecular electron transfer [211,212]. A large proportion of

semiconductor electrochemistry is carried out in aqueous solutions [213–215] but organic solvents are also used for their advantages such as larger potential window, lower adsorption of impurities, lower rate of dissolution of inorganic electrodes, and larger selection of available redox mediators [101,207,216].

3.3. Electrochemistry of bulk layered materials

Bulk layered TMDCs have been at the forefront of electrochemistry research in the second half of 20th century, several decades before the graphene revolution [199,201,210]. The VBM and CBM energies vary significantly among TMDCs, but most of them have VBM low enough to oxidise water, either by lowering E_F or photogeneration of holes in the VB, and CBM lower than E^0_{redox} for hydrogen evolution, making direct water reduction unlikely [205]. Only loose correlation has been found between the A and B excitons in the visible absorption spectra and the observed anodic photocurrent in TMDCs (Fig. 8a) due to a number of contributing intermediate processes [3,217]. However, the photoanodic current in n-doped MoS_2, $MoSe_2$, and WSe_2 shows the typical minority charge carrier-driven plateau with a largely energy-independent potential, whose height increases with the energy of the excitation laser (Fig. 8b) [204].

Group 6 TMDCs exhibit a remarkable stability against photocorrosion [217,218]. This is attributed to the non-bonding character of the optical transitions in the visible and near-IR range originating from the M *d* orbitals (Fig. 8d) [3,66]. Transitions are possible from the p_z orbitals of the chalcogenide deeper in the VB but they lie in the UV range [219]. This stability is further enhanced in iodide solutions, which act as scavengers for the photogenerated holes that would otherwise cause oxidation of the metal and formation of sulphate or selenate [200,218–220]. Passivation of MoS_2 surface by photoanodically-generated elemental sulphur was also proposed [3]. Contrasting the iodide-induced stability, n-type $MoSe_2$ undergoes photoanodic decomposition in the aqueous chloride and bromide solutions but is stable their organic solutions, which highlights the important role of a solvent [219,221]. In group 4 TMDCs and conventional bulk semiconductors such as CdS, ZnO, or GaAs, the anodic hole formation can lead to photocorrosion by destruction of the *p* orbital mediated bonds [210,217,219].

Electron transfer on TMDCs using different redox mediators has been studied by several groups. Tributsch and Bennett measured $Fe^{3+/2+}$, Br^-/Br_2, and p-quinone HET, and water photoelectrolysis on MoS_2 [3]. Abruña et al. measured HET of $[Ru(NH_3)_6]^{3+/2+}$, $[Fe(CN)_6]^{3-/4-}$, $Fe^{3+/2+}$, I_3^-/I^-, methyl viologen, and others redox systems on WSe_2 [214] and $MoTe_2$ [208]. Dark current measurement on n- and p-doped WSe_2 revealed that while $[Ru(NH_3)_6]^{2+}$ oxidation has a unity transfer coefficient α, expected for a majority carrier driven irreversible reaction on a semiconductor in depletion, most of the other redox mediators show more reversible α of 0.1–0.4 [222]. A more recent study on natural MoS_2 crystals demonstrated tuning of the effective HET rate of $[Ru(NH_3)_6]^{3+/2+}$ over 3 orders of magnitude by white light illumination (Fig. 8c) [87]. This HET-illumination dependence was even stronger for $[Fe(CN)_6]^{3-/4-}$ and $[IrCl_6]^{2-/3-}$ mediators with more positive redox potential, falling into the photoanodic regime of n-MoS_2.

The triodide/iodide (I_3^-/I^-) redox reaction relevant to photoelectrochemical solar cells (PEC) has been studied intensely for group 6 TMDCs with the typical light-to-current conversion efficiencies of 5–10% [126,208,218,220]. Due to the small band gap size of bulk MoS_2, $MoSe_2$, and WSe_2 (1.0–1.2 eV), the maximum observed photovoltage was ~0.7 V [126,215], with ~0.5 V energy equivalent lost in the charge separation of the photogenerated charge carriers and electrochemical overpotential [204]. One of the most successful PEC implementation of these materials was demonstrated by Fan et al. for aqueous I_3^-/I^- redox reaction on n-WSe_2, showing impressive conversion efficiency of 14% and an open circuit photovoltage of 0.7 V using continuous light source with wavelengths >590 nm [215]. Furthermore, the effective quantum efficiency approaching 100% for water photoelectrolysis was suggested [3] and an effective "uphill" photooxidation (occuring at much smaller overpotentials than on a reversible electrode such as Pt) was found for chloride on n-MoS_2 and hexamethylbenzene on n-$MoSe_2$ in acetonitrile [216,221].

3.4. Electrochemistry of mono- and few-layer 2D materials

Fundamental understanding of 2D materials' electrochemistry has been lagging behind the rapid progress made in condensed matter physics and materials science, which is somewhat surprising given the extensive electrochemistry research activity on bulk layered TMDCs in the 1970–1980s. Therefore, huge gaps remain in the key aspects of 2D materials' electrochemistry, perhaps amplified by the variety of preparation methods and the lack of studies on well-defined surfaces. The advanced nanofabrication processing adopted by the physics and nanoscience communities, which stems from the highly evolved semiconductor industry, relies on the use of clean rooms, and ensures high standard of the fabricated devices, is not widespread within the physical chemistry community. Furthermore, many of the physical phenomena, which could be exploited in electrochemistry, are often observed only in the high-quality 2D materials prepared by ME or CVD. In contrast, most electrochemical studies use lesser quality 2D materials prepared by LPE or intercalation.

Naturally, there are fundamental size limitations to electrochemistry due to finite diffusion of molecules in solution, however, the recent significant advances in microscale electrochemistry including the scanning electrochemical microscopy (SECM), scanning electrochemical cell microscopy (SECCM) or microdroplet method demonstrated the feasibility of micro- and nano-scale measurements on graphene and other 2D materials [89,223–225]. Most groups focus on the HET using common redox mediators or specific catalytic reaction but there is a distinct lack of measurements of fundamental interfacial capacitance [146,226,227]. Also surprising is the fact that very few of the recent reports use illumination control when studying the electrochemistry of semiconducting 2D materials [87,146], given breadth of the photoelectrochemical studies on layered materials in 1980s [201,214,217].

It is important to realise that the application of 2D materials in electrochemistry, electronics, or photovoltaics, relies on good ohmic contacts. A useful strategy using a one-dimensional contact between the edge of a 2D material and a metal contact has demonstrated low contact resistance (~100 Ω μm for graphene and ~10 kΩ μm for 2D semiconductors) due to the large orbital overlap [137,228]. In the case of semiconducting 2D materials, a non-ohmic, rectifying Schottky barrier is established between the 2D materials and the metals contact. Similarly to the semiconductor/liquid interface, this occurs due to the band bending, which arises from the differing E_F in the metal and in the semiconductor. The Schottky barrier is defined as $\Phi_B = \Phi_M - \chi$, where Φ_M is the work function of the metal and χ is the electron affinity of the semiconductor. It has been shown that MoS_2 contacts with low Φ_M metals (Sc, Ti, or Al) lead to much higher charge carrier injection and effective mobilities due to the reduced Φ_B and the E_F pinning close to the CB (Fig. 9), than contacts with high Φ_M (Au, Ni, or Pt) [53,187], but low Φ_B, independent of Φ_M were also observed [185]. Near-ohmic contacts between MoS_2 and Ti were also achieved by vacuum annealing [229].

We now proceed to outline the state-of-the-art understanding of how various phenomena affect the electrochemistry of 2D materials.

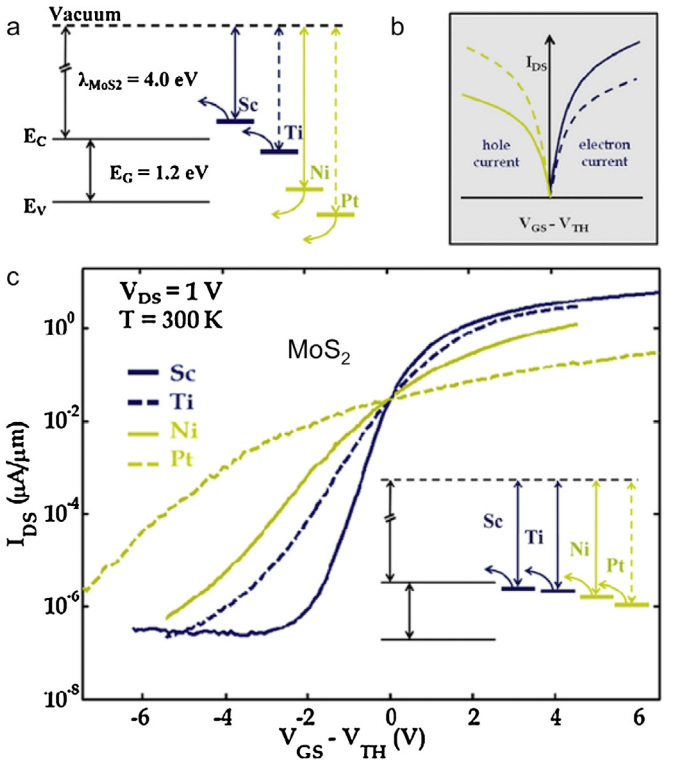

Fig. 9. The importance of metal contacts in semiconducting 2D materials. a, Comparison of the MoS2 electron affinity with the work functions of several metals used as contacts for electronic transport measurements. b, Expected electronic transport characteristics based on a. c, Current–voltage transport measurements of a 6 nm-thick MoS_2 indicating formation of Schottky barriers of various height across the metal–MoS_2 interface. Figure adapted with permission from [53] © 2013 American Chemical Society.

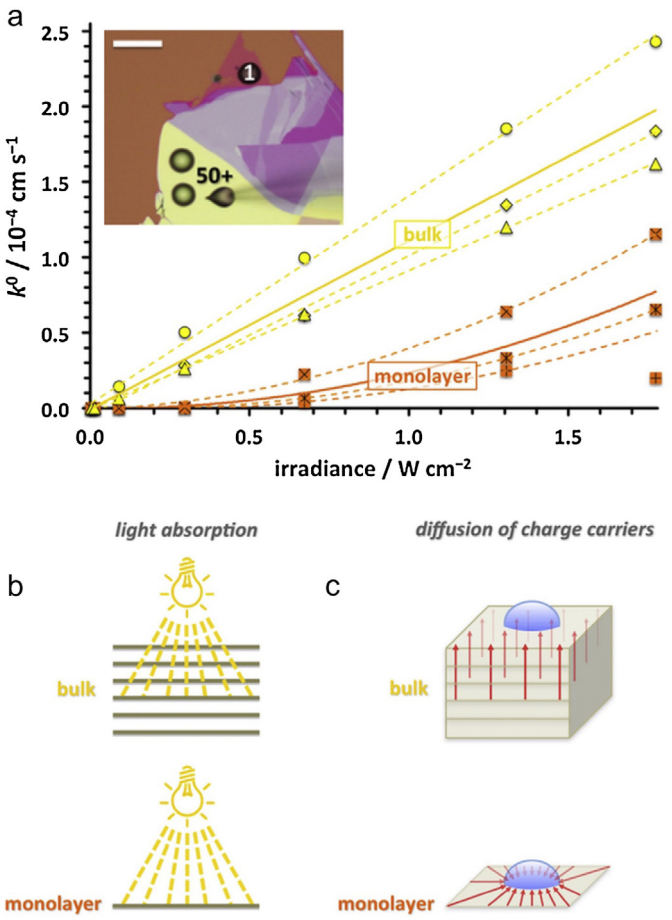

Fig. 10. Dependence of the electron transfer on the number of layers in MoS_2. a, The effective HET rate (k^0) as a function of the illumination intensity (irradiance) for monolayer and bulk natural MoS_2. Inset shows the microdroplet electrochemical cell used for the measurement. b, Schematic comparing the light absorption efficiency for bulk (top) and monolayer (bottom) MoS_2. c, Schematic showing the corresponding linear interlayer (top) and radial intralayer (bottom) diffusion of charge carriers in bulk and monolayer MoS_2, respectively. Figure adapted from [146] published by the American Chemical Society under CC-BY licence.

3.5. Dependence on the number of layers

Several factors influence the dependence of the photocurrent on the thickness of a 2D material and their effective interplay determines the dominating or limiting electrochemical mechanism. These factors include: charge carrier density, in-plane carrier mobility, interlayer charge transfer or mobility, and, in the case of semiconductors, thickness-dependent light absorption and band structure-dependent photogeneration of charge carriers. The dependence of HET and capacitance on the number of graphene layers was studied extensively for several years but large discrepancies and contradicting results from different groups mean that no satisfactory consensus on this matter currently exists [89,230–234]. Velický et al. have recently observed a monotonous increase of the photocurrent and capacitance with the increasing number of layers in a photoelectrochemical experiment using ME crystals of natural molybdenite deposited on a poly(methyl methacrylate) (PMMA) substrate and a localised microdroplet measurement [146]. The authors also showed that the effective k^0 depends linearly on the illumination intensity for bulk MoS_2, but has non-linear dependence for monolayer MoS_2, which was rationalised by a linear interlayer diffusion of charge carriers in bulk in comparison to a non-linear intralayer diffusion of charge carriers in monolayer (Fig. 10). These findings prove an effective interlayer charge transfer, which was also observed in bulk TMDCs using rear illumination geometry [204]. The general increase in mobility of TMDCs with the increasing number of layers discussed above (Table 2) also supports these observations. In contrast, recent AFM-spectroscopy measurements of MoS_2 on ITO substrate showed that the photocurrent decreases with increasing thickness up to 4 layers and then increases again in bulk MoS_2, which was explained by two competing mechanisms: the direct-to-indirect band gap transition from monolayer to bulk MoS_2 versus the increased light absorption in thicker samples [235].

3.6. Role of defects and crystal quality

The role of defects, steps, and edge plane in electrochemistry of layered materials has been long recognised. Significant body of knowledge has been accumulated for graphite and graphene and the general consensus assumes an increased electrochemical activity of the edge plane in comparison to the basal plane [223,236,237], although the exact nature of these differences is still being challenged [87,238]. One of the best recent attempts to quantify the correlation between the HET and defect density in graphene was achieved by controlled Ar^+ irradiation and characterisation by SECM and Raman spectroscopy (Fig. 11a) [239]. It is also accepted that the pristine basal plane of MoS_2 exhibits slower electron transfer than the edge plane or defects as demonstrated for several redox systems, including $[Cu(NH_3)_x]^{2+/1+}$, $[Fe(CN)_6]^{3-/4-}$, $Fe^{3+/2+}$, I_3^-/I^- and oxygen reduction reaction [199,201,217]. The $[Fe(CN)_6]^{3-}$ reduction was found to proceed much faster than the reverse oxidation due to the alignment of the redox potential and electronic band structure. A study by Velický et al. using $[Fe(CN)_6]^{3-/4-}$, $[Ru(NH_3)_6]^{3+/2+}$, and $[IrCl_6]^{2-/3-}$ redox meditators

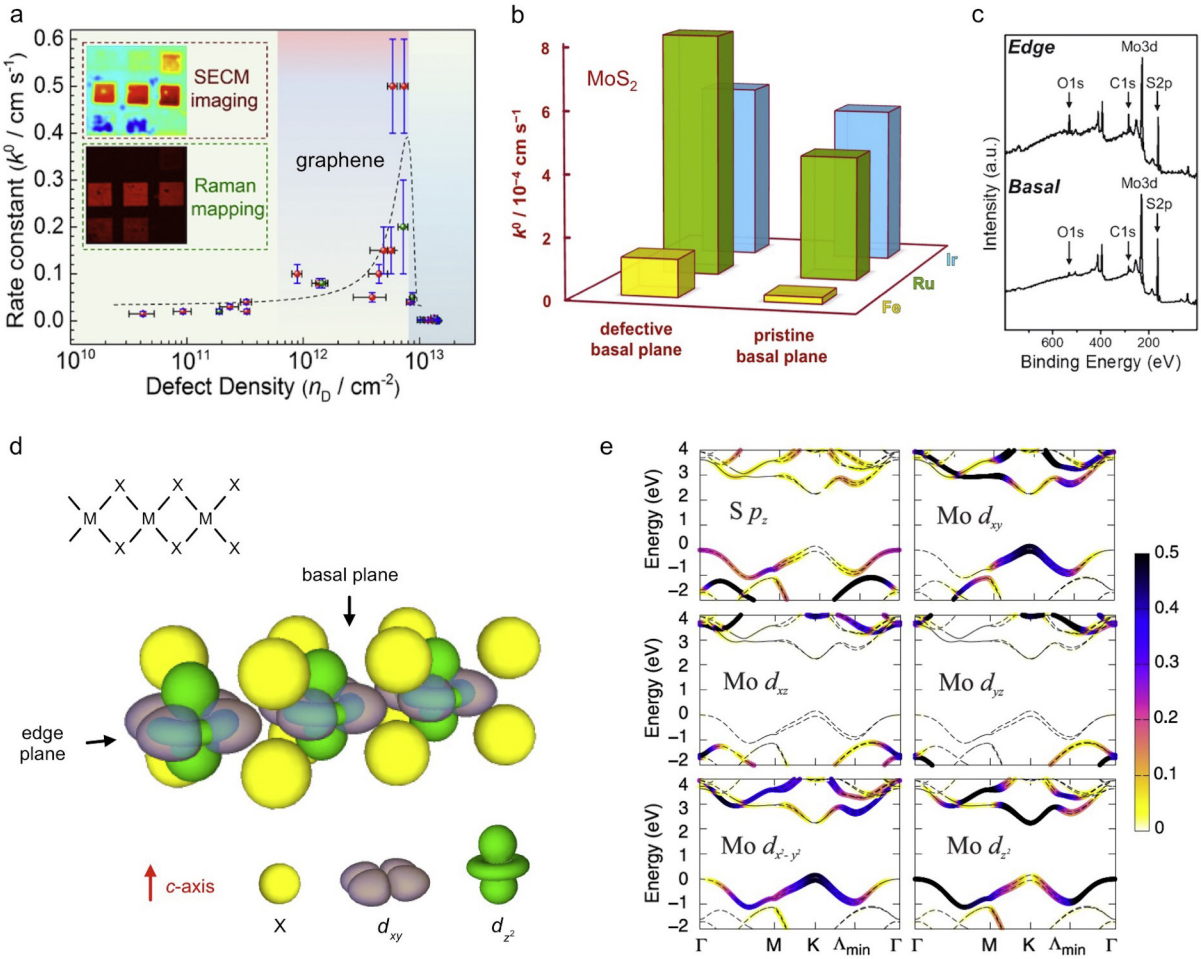

Fig. 11. Role of defects in electrochemistry of 2D materials. a, Quantitative correlation between the HET rate (k^0) and defect density in monolayer graphene induced by Ar^+ ion irradiation. The inset shows the SECM and Raman (defect-induced D mode intensity) activity for different irradiation doses. b, Comparison of k^0 for pristine and defective basal plane of MoS_2. c, Comparison of the XPS spectra for the edge and basal plane of MoS_2. d, Schematic of the orientation of the VBM and CBM *d* orbitals in 2H-TMDCs ($3d_{xy}$ and $3d_{z^2}$ orbitals shown). e, Projection of S $3p_z$ orbital and Mo 4*d* orbitals contributions to the electronic states in monolayer MoS_2. Figures adapted with permission from: a, [239] © 2014 American Chemical Society. b, [87] published by the PCCP Owner Societies under CC-BY licence. c, [173] © 2015 John Wiley and Sons. e, [241] © 2014 American Physical Society.

under illumination control has shown that a small amount of defects on the basal plane of MoS_2 increases the HET up to 6-fold depending on a redox mediator (Fig. 11b), an effect, which was not observed for natural graphite [87]. Furthermore, the HET of $[Fe(CN)_6]^{3-/4-}$ was shown to be more sensitive to the edge/basal plane ratio than $[Ru(NH_3)_6]^{3+/2+}$. This was confirmed in parallel work by Tan et al. who further revealed that proton reduction and electrochemical corrosion are more pronounced on the edge plane of natural MoS_2, due to the edge plane being more oxidised (Fig. 11c) and having higher density of electronic states (DOS) at E_F than the basal plane [173]. Electronic transport measurements, both in-plane and tunnelling, are also known to be very sensitive to defects and disorder, much more than other methods such as Raman, optical microscopy, or AFM [14,98]

Differing steric accessibility of the *d* orbitals of the transition metal was argued as the reason for the increased edge plane activity of MoS_2 [199]. We now expand this somewhat simplistic view further. Fig. 11d shows that the d_{xy} (and the not shown $d_{x^2-y^2}$) orbitals of the metal are aligned along the layers and are fully obstructed by the chalcogenide atoms in the *c*-axis direction. These orbitals are therefore less likely to take part in electrochemical reactions except when present at the edges, where they are not obstructed due to the metal termination and chalcogenide vacancies common at the edge plane. It is therefore thought that the out-of-plane charge transfer occurs purely by electron tunnelling via the d_{z^2} metal orbital, which, despite also being obstructed by the chalcogenides atoms, extends significantly in the *c*-axis direction [219,240]. This anisotropy should have further implications for cathodic vs. anodic reactions due to the fact that d_{z^2} has been assumed to be a purely VB orbital and the $d_{xy}/d_{x^2-y^2}$ purely CB orbitals (Fig. 8d) [199,219]. If that were the case, the cathodic reactions involving the $d_{xy}/d_{x^2-y^2}$ orbitals should show much higher sensitivity to the basal/edge plane ratio than anodic reactions involving d_{z^2} orbitals, a hypothesis, which has not yet been conclusively supported or disproved. In fact, detailed theoretical calculations show that all of the d_{z^2}, d_{xy}, and $d_{x^2-y^2}$ orbitals of the metal contribute significantly to both the VBM and CBM (unlike d_{xz} and d_{yz}), depending on the charge carrier momentum in the Brillouin zone, as shown in Fig. 11e [240,241]. Further complexities arise from the intrinsic doping of TMDCs, Fermi level pinning by surface states, and inner vs. outer sphere nature of redox mediators.

Several non-electrochemical observations also support the increased edge reactivity. Preferential oxidation of the edge plane of MoS_2 was observed in wet air at 545–590 °C by SEM [180]. A metallic state at the edge of monolayer MoS_2 on graphite substrate with significant band bending of ~0.6 eV within 5 nm from the interface was directly observed by STM and STS (Fig. 12) [242]. The edge of CVD monolayer WS_2 exhibits almost two orders of magnitude

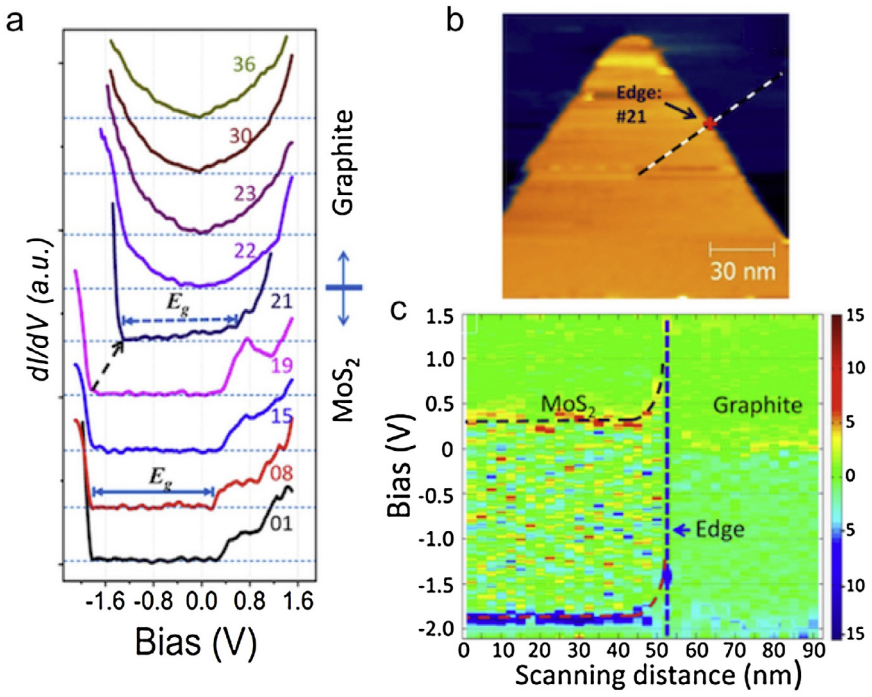

Fig. 12. Direct imaging of the electronic band structure of monolayer MoS_2. a, STS differential current–voltage curves scanned from the monolayer MoS_2 crystal interior, pass the crystal edge, to the graphite substrate. b, Corresponding STM image of the device indicating the scan direction. c, Real space imaging of the electronic band structure at the MoS_2/graphite interface using a current–voltage differential function. Figure adapted with permission from [242] © 2014 American Chemical Society.

higher PL in comparison to the crystal interior due to the accumulation of excitons [118]. Introducing defects by argon or oxygen plasma detectable by Raman spectroscopy decreased the contact angle with water to as low as 9 °C for highly-ordered pyrolitic graphite (HOPG) [243] and 55 °C for epitaxial graphene [244].

Despite the apparent higher edge plane activity, the basal plane of bulk TMDCs was studied extensively. In fact, it was proposed that defects, edge plane, and dangling bonds attract adsorbates, which create surface states within the band gap acting as major recombination centres for the photogenerated charge carriers and enabling parasitic reactions pathways. This is inherently related to the fast in-plane carrier mobility; the minority carriers find it easier to travel along the layers towards the edge surface than to tunnel through the layers towards the basal surface (Fig. 13). This in turn leads to a reduction in the photovoltage and conversion efficiency on the edge plane, both of which have detrimental impact on all of the photoelectrochemical applications of TMDCs [65]. Comparison of the pristine and photocorroded basal plane of MoS_2 also showed that while the photocurrent plateau is defect-insensitive, the overpotential increases markedly at high defect density [204]. Furthermore, surface states introduced within the band gap by defects were found to increase the carrier photogeneration for lower-than-band gap photons but also severely reduced the conversion efficiency [245]. A temporary improvement was achieved by pushing the surface state energies outside the band gap through adsorption and partial intercalation of organic molecules at the edges [88]. The edge plane and defects in TMDCs were also found to suffer from significant photocorrosion [210], and a comparative study by Chen et al. confirmed that the reduced photoelectrochemical efficiency at MoS_2 defects due to recombination are accompanied by an increased HER activity [246].

Major issue with the fundamental electrochemical studies of 2D materials is the vast variation of different preparation methods. Only ME crystals characterised by microscale electrochemical methods are suitable for fundamental studies. CVD-grown crystals are often though of as second best in terms of quality, provided that polycrystallinity and grain boundaries can be controlled. For example, the charge carrier mobility in HOPG, often deemed a very suitable material for fundamental studies is almost one magnitude lower than that of natural graphite [247]. Despite their high quality, ME and CVD crystals also contain impurity elements or defects. For example, MoS_2 is known to harbour a large number of sulphur vacancies [176], which are thought to lead to its n-doped character [151], and to mediate hopping transport under low charge carrier density conditions [34]. However, both n- and p-type doping related to compositional changes have been observed on the surface of the same MoS_2 crystal [185] and p-doping due to Na and O impurities on SiO_2 substrates was suggested by DFT [248]. Substrate cleanliness is crucial for preparation using ME and CVD, typically achieved by O_2 plasma cleaning, which removes the adsorbates, alters termination of the surface Si atoms, and therefore increases the adhesion between the 2D material and substrate [51,92,249]. LPE and other solution-based method remain very popular due to the ease of preparation and scalability, especially for sensing applications or catalysis. However, an accurate control of the 2D nanosheet size and thickness is challenging and the resulting electrode is always a mixture of many different surfaces types. The use of these poorly-defined materials often leads to artificially inflated capacitance values, due to the large mismatch between the active and geometric surface area [186]. Furthermore, the LPE flakes are usually place on a conductive substrate (Fig. 6d) such as glassy carbon or metal, which is itself electrochemically active and can interfere with the electrochemical signal [112].

3.7. Role of surface ageing

The role of surface ageing of layered and 2D materials has been somewhat neglected in literature until recent years. Electrochemistry is particularly sensitive to any such changes because the majority of electrochemical processes occur on the surface, which is exactly what 2D crystals are: surface-only materials. Their surface is readily contaminated by organic molecules, water, and other

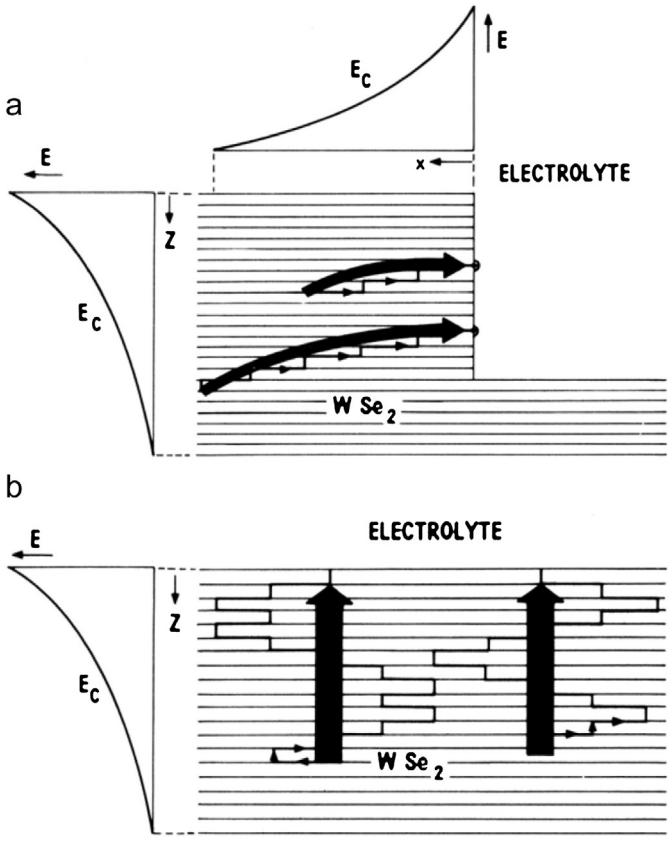

Fig. 13. Carrier diffusion in layered crystals. a, Crystals with high edge presence: fast intralayer carrier transport results in a direct path between their photogeneration and recombination and therefore faster carrier diffusion. b, Crystals with pristine basal plane surface only: slow interlayer transport of carriers results in a less direct path between their photogeneration and recombination and therefore slower carrier diffusion. Figure adapted with permission from [65] © 1980 American Chemical Society.

adsorbates, which is manifested in deterioration of their electrochemical and electronic properties and in the change of the contact angle between the 2D surface and water [87,119,189,250]. Some of these adsorbates can act as charge trappers, affecting the electronic transport in 2D materials [139,145,251]. The effect of ageing on graphite in the context of electrochemistry was first noted in 1990s [252], but it was not until two decades later that it was determined as the limiting factor for HET of $[Fe(CN)_6]^{3-/4-}$ [250]. A recent study extended this observation to natural graphite and molybdenite, by comparison of an aged surface and freshly cleaved surface, prepared by in situ exfoliation of the layered material [87]. The HET on graphite decreased by up to two orders magnitude on the aged surface in comparison to the freshly cleaved surface (Fig. 14a) and up to one order of magnitude for MoS_2 (Fig. 14b), also dependent on the redox mediator. HET on MoS_2 has also been shown to deteriorate upon consecutive voltammetric cycling using $[Ru(NH_3)_6]^{3+/2+}$, which was surprising given the previously presumed outer-sphere nature of this mediator (Fig. 14c). The ageing was attributed to the adsorption of airborne hydrocarbons and, in the case of MoS_2, also to the surface oxidation evidenced by XPS (Fig. 14d). Another study proposed ageing by impurities from ultrapure water with high (~20 ppb) carbon content [253], and offered a surface-protection strategy based on low-temperature water treatment [254].

Surface ageing is manifested by significant changes in wetting by liquids. 2D and layered materials' surfaces have been long thought to be hydrophobic but observations of the surface/water contact angles have shown that this is not the case. The native angle of the freshly exfoliated/prepared surface of 44°–69° increases upon exposure to air and saturates at 80°–100° on the aged surface [188,189,244,255]. These changes reflect the initially hydrophilic surface becoming more hydrophobic upon contamination by airborne organic molecules. Time scales of the surface ageing vary, but most significant changes for monolayer/bulk graphene, MoS_2, and WS_2 occur within 20–60 min and the contact angle reaches almost complete saturation within 1 day after exfoliation/preparation (Fig. 14e). XPS, FTIR, STEM, and ellipsometry measurements confirm the hydrocarbon nature of the adsorbed species (Fig. 14d), indicate that their thickness is around 0.5–2.0 nm, and show that the ageing can be slowed down by covering the surface with chloroform and that the contamination can be partially removed by annealing at low pressure and inert atmosphere [87,188,189,243]. Polymer residues such as PMMA, leftover on the surface of 2D materials after transfer procedures, are also notoriously hard to remove, even by well-established methods such as inert-atmosphere annealing or solvent cleaning [256–258], and their exact role in electrochemistry, i.e. a mere reduction of accessible surface area versus qualitative changes in the surface DOS, remains uncertain [259].

Graphite and MoS_2 are thermodynamically very stable but they do partially oxidise in air, especially in high temperature and humidity environment [29,196]. Colourimetry and XPS revealed that oxidation of MoS_2 is only limited to the outermost layer, protecting the interior for up to several days at 110 °C and for almost two years at room temperature [183,260]. Gravimetric and titration experiments determined that surface sulphates and oxides promote physisorption and chemisorption of water molecules, respectively [261]. Many other 2D materials are known to oxidise strongly in air, which is symptomatic of their low natural abundance.

4. Modification of 2D materials

4.1. Substrate effects

The effects of an underlying substrate on the properties of 2D materials are complex and not fully understood. Scanning probe microscopy and PL spectroscopy reveal that the surface roughness, termination, variations in physical separation, and trapped charges all have an effect on the doping, electronic coupling, and charge transfer between a 2D material and its substrate. It was shown that the charge carriers photogenerated in Si and diffusing into SiO_2 effectively dope graphene [149]. The enhanced mechanical coupling between MoS_2 and SiO_2 substrate in dielectric-encapsulated samples leads to more consistent n-type doping of MoS_2 originating from an increased negative trion concentration [150]. The PL in monolayer MoS_2 suspended over a hole was found to be more than 4 orders of magnitude stronger than on an SiO_2 substrate [63], but little changes were observed in the Raman spectra of suspended/bound mono- and few-layer MoS_2 and $MoTe_2$ [143,156]. Buscema et al. found that monolayer MoS_2 has the lowest PL intensity on an SiO_2 substrate in comparison to graphene, mica, hBN, and gold [172]. Finally, DFT calculations suggest that the orientation of MoS_2 on an SiO_2 substrate has only marginal effect on the electronic structure [248].

The use dielectric gate such as HfO_2 was shown to increase the room temperature charge carrier mobility in monolayer MoS_2 from 0.1–10 to 200 $cm^2 V^{-1} s^{--1}$ [33]. Bao et al. have discovered that while the mobility of multilayer MoS_2 on an SiO_2 substrate was moderate (30–60 $cm^2 V^{-1} s^{-1}$) and relatively independent of MoS_2 thickness, PMMA substrate led to thickness-dependent mobility with a maximum of ~480 $cm^2 V^{-1} s^{-1}$ in bulk MoS_2 [262]. Enhanced dielectric screening in multilayer MoS_2 on PMMA was proposed as the dominating mechanism for these surprising long-

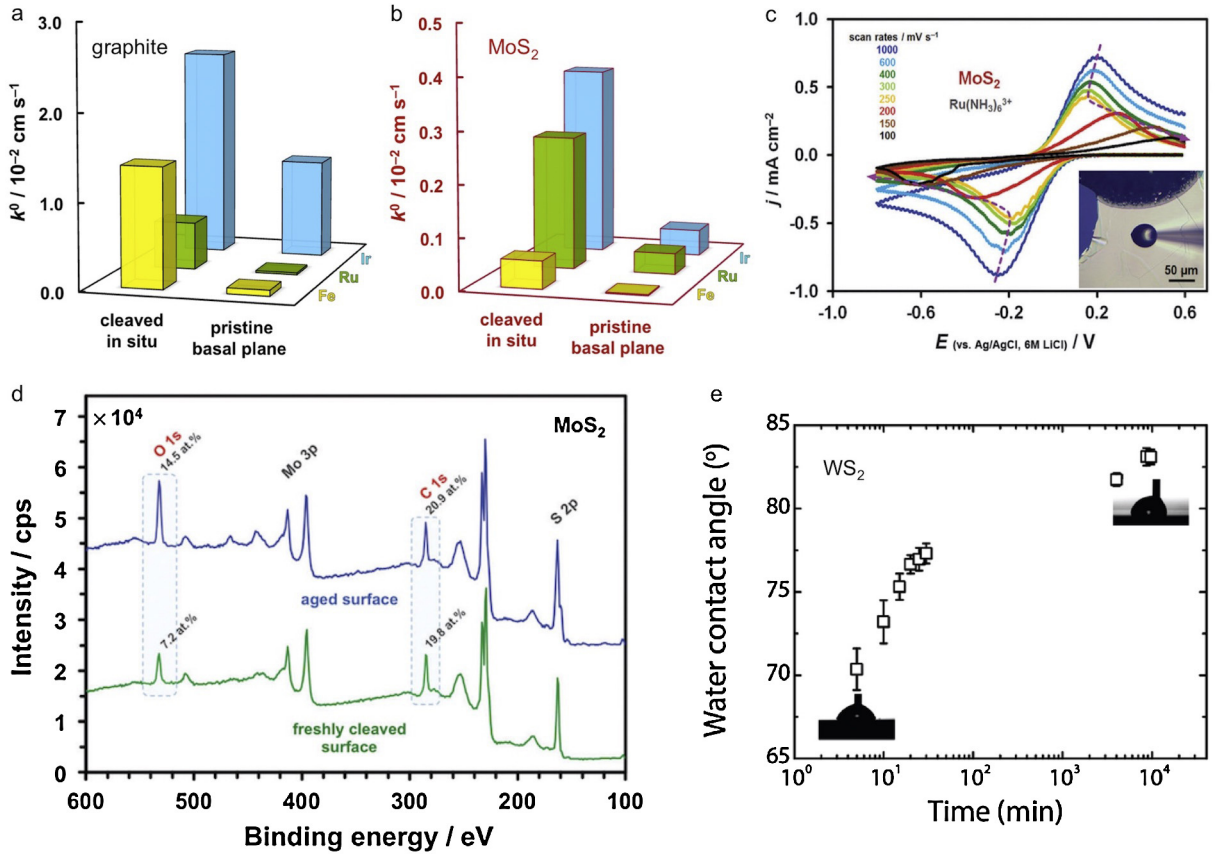

Fig. 14. Surface ageing of layered and 2D materials. a–b, Comparison of the HET rate (k^0) between the freshly cleaved (exfoliated) and pristine basal plane surface of graphite and MoS_2, respectively. c, Deterioration of the HET on MoS_2 with consecutive voltammetric cycling, expressed by the increase in the peak-to-peak separation of $[Ru(NH_3)_6]^{3+/2+}$ reduction/oxidation. d, Comparison of the XPS spectra between the aged and freshly cleaved surface of MoS_2. e, Surface ageing of monolayer WS_2 manifested by the increase in the 2D surface/water contact angle (and therefore hydrophobicity). Figures adapted with permission from: a–d, [87] published by the PCCP Owner Societies under CC-BY licence, e, [119] © 2015 American Chemical Society.

range effects (up to 50 nm thick MoS_2) in contrast to the short-range disorder such as chemical bonding or interface roughness dominating the mobility in MoS_2 on SiO_2. These finding were confirmed by a two orders of magnitude increase in the carrier mobility of thin InSe on a PMMA substrate in comparison to an SiO_2 substrate [263]. In contrast, Withers et al. studied WS_2 on different dielectric substrates and proposed that the electronic transport is limited by the intrinsic disorder rather than extrinsic factors [52]. Insulating hBN has been used widely as a substrate and encapsulating layer for other 2D materials. This approach both prevents degradation of thin layers and increases carrier mobility in graphene to >100,000 $cm^2\ V^{-1}\ s^{-1}$ at room temperature [14,137,264]. The important role of solvents used in contact with 2D materials was revealed through changes in the PL peak energy between 1.78 and 1.90 eV and enhanced PL intensity when halogenated solvents were used with monolayer MoS_2 [167]. Most relevant to electrochemistry, Hui et al. have recently shown that an underlying Au substrate alters the effective DOS in bilayer graphene, manifested by ~5-fold increase in the HET kinetics of $[Fe(CN)_6]^{3-/4-}$ reduction/oxidation measured by SECM [265]. Such a demonstration of the substrate effect holds promise for a new-generation of tuneable electrochemical devices based on "electronically-transparent" 2D materials.

4.2. Hydrogen evolution reaction and phase engineering

2D materials were soon considered as potential candidates for the energy storage and conversion applications, such as batteries, fuel cells, and supercapacitors [17]. The use of hydrogen as energy carrier is one of the most promising long-term solution for renewable energy, due to its low environmental impact and high energy density [266]. Finding novel catalyst materials for the hydrogen evolution reaction (HER) is therefore one of the major frontiers of the 2D materials research [28].

The HER process consists of two steps in acidic media: adsorption of protons at the catalytic sites of the electrode, and reduction of protons by to monoatomic hydrogen (H) and subsequently hydrogen molecule (H_2). Briefly, it can be divided into three operative reaction mechanisms [267]: first, the initial adsorption discharge step (Volmer reaction, where the Tafel slope, $b \approx 120$ mV dec^{-1}), which can be followed by either an electrochemical desorption step (Heyrovsky reaction, $b \approx 40$ mV dec^{-1}) or a recombination step (Tafel reaction, $b \approx 30$ mV dec^{-1}). The Tafel slopes and exchange current densities obtained from the hydrogen evolution voltammetric curves therefore determine the HER performance of a material. The best HER catalyst to date is platinum with the exchange current density of $\sim 4.5 \times 10^{-4}$ A cm^{-2}, and b as low as 30 mV dec^{-1} [267]. Because of their low cost, chemical stability, and electrocatalytic properties, TMDCs have been of an increasing interest as possible substitutes for the expensive Pt in HER catalysis, both in their pristine and modified forms. The typical b values of unmodified natural, LPE, CVD or solvothermally-grown TMDCs are between 90 and 170 mV dec^{-1} [268–272]. Significantly increased HER activity reaching b of 40–80 mV dec^{-1} is observed for the edge plane of natural crystals, vertically-aligned synthetic crystals, and thin crystals exfoliated by organolithium intercalation method [173,268,272–275]. For example, b of 60 and 77 mV dec^{-1} has been found in the case of vertically-aligned $MoSe_2$ and WSe_2 nanofilms, respectively, grown on carbon fibres (Fig. 15a–f) [276].

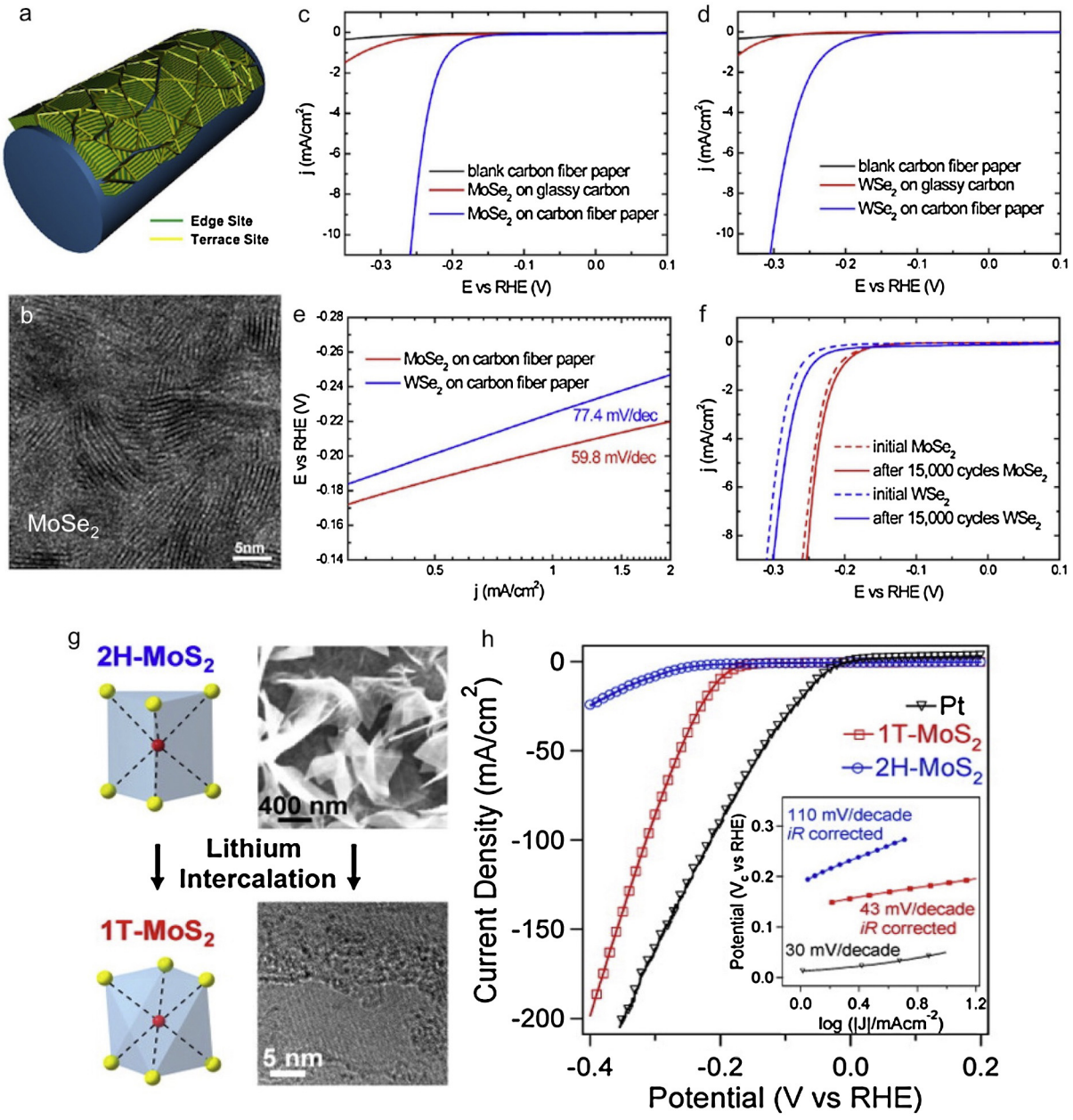

Fig. 15. HER and phase engineering in TMDCs. a, Schematic of vertically-aligned edge-terminated TMDC film on a curved surface. b, TEM image of such $MoSe_2$ film on a Si nanowire of ~100 nm in diameter. c–d, HER polarisation curves for vertically-aligned $MoSe_2$ and WSe_2 films on flat glassy carbon and curved carbon fibre paper substrates. e, Corresponding Tafel analysis. f, Polarisation cycling stability of the films. g, Schematics and SEM/TEM images of the 2H–1T phase engineering of MoS_2 by lithium intercalation. h, Polarisation curves showing the superior HER catalytic activity of the metallic 1T phase of MoS_2 in comparison to the semiconducting 2H phase. Figures adapted with permission from: a–f, [276] © 2013 American Chemical Society, g–h, [268] © 2013 American Chemical Society.

Photoelectrochemically driven HER was also reported for LPE WSe_2 nanosheets [277].

Crucially, the lithium intercalation method transforms the stable semiconducting 2H phase of group 6 TMDCs into the metallic 1T phase, which has significantly higher HER activity. This has been demonstrated by Lukowski et al. for MoS_2, with more than a two-fold difference in *b* between the 1T and 2H phase, as shown in Fig. 15g–h [268]. The same approach was used recently to prepare 1T-WS_2 with excellent HER Tafel slopes of ~60 mV dec^{-1}, comparable with MoS_2 [278]. FETs with locally engineered 1T phase MoS_2 regions have revealed contact resistance over one order of magnitude smaller than for the 2H phase [41] and the associated differences in the 1T and 2H electronic structure were also examined by the DFT calculations for a range of different TMDCs [279,280]. The HER activity of several TMDCs was shown to increase significantly when butyllithium was used for their exfoliation, in comparison to the lower enhancement achieved by methyllithium [281]. Furthermore, a reductive and oxidative electrochemical pretreatment has been shown to affect the HER on MoS_2 and was proposed to be related to the 2H to 1T phase transition [282]. Other technologically relevant electrochemical processes such as the oxygen reduction reaction (ORR) and oxygen evolution reaction (OER) were studied to a much smaller extent [283,284].

4.3. Intercalation into layered materials

Intercalation of various chemicals into layered crystals has been studied extensively and is epitomised by the success of the

graphite-based Li-ion battery and related energy technologies. Intercalation is also a suitable answer to the search for a scalable production of 2D materials in a liquid phase, due to the direct applicability of the resulting dispersions of 2D nanosheets of varied lateral sizes and thicknesses in ink-based technologies [110,285]. Negatively charged graphene oxide (GO) nanosheets as a product of acid (typical sulphuric) intercalation into graphite was studied early on [286,287]. The epoxy, hydroxy, carbonyl, and carboxyl groups at the GO surface lead to enhanced interactions between individual nanosheets, a property resulting in a reinforcement of its mechanical properties [288]. Therefore, GO and reduced GO have been widely studied over the past decade, due to the their potential use as fillers in polymer-based composites [289,290]. Exfoliation of bulk TMDCs to negatively-charge 2D nanosheets by intercalation is also widely reported in literature [5]. The most commonly used intercalating agents are alkali metals, i.e. Li, K, Na, and Rb [32,104,291], or tetraalkylammonium cations [10,292]. Intercalation with lithium compounds can yield large quantities of 2D materials, however, the as-produced nanosheets are defected and functionalised, which requires further purification steps in the production [107,281]. Development of optical and spectroscopic methods for in situ monitoring of lithium intercalation into layered materials is also an area of active research [32,293]. For example, a method of controlling the PL in LPE few-layer MoS_2 nanosheets by intercalation and de-intercalation of Li^+, Na^+, and K^+ has been developed [294]. Capacitance of bulk Mo/W/S/Se TMDCs increases upon lithium intercalation-assisted exfoliation and it also depends on the nature of the intercalating agent, with an anomalously high capacitance obtained for WS_2 and *tert*-butyllithium [103]. Lithium intercalation was also successfully applied to exfoliation of less common vanadium dichalcogenides [295]. These recent developments play an important role in novel optoelectronic technologies, photodetection, and energy conversion/storage [296,297].

4.4. Functionalisation of 2D materials

Chemical or physical functionalisation of 2D materials is also extensively researched area. The former is achieved by attaching various chemical groups, either covalently or non-covalently, to the 2D surface, whereas the latter refers to decoration of the 2D surface with nanoparticles (NP) or construction of heterostructures by combining different 2D materials together [5,298–300]. The most common process to achieve chemical modification of graphene or graphite, which was also used to study the HET, is the reductive functionalisation using aryl diazonium chemistry [196,301,302]. The early work on the covalent functionalisation of TMDCs focused on the reaction of organoiodine compounds or diazonium salts with Li intercalation-exfoliated 1T-MoS_2, 1T-WS_2, and 1T-$MoSe_2$ [303,304]. Importantly, this functionalisation occurs on the more reactive edge plane as well as on the less reactive basal plane of TMDCs. The use of thiol linking groups is becoming popular in covalent functionalisation of MoS_2 [305]. Utilisation of the lone pair electrons, common in most metal chalcogenides, for the functionalisation using Lewis acid-based reaction has been shown to have potential in photovoltaics and photodetection [306]. Spontaneous aryl diazonium functionalisation of thin layered black phosphorus (Fig. 16a–c) has been shown to induce p-doping and to improve FET mobility, on/off ratio, and material stability in ambient environment [307]. Recent efforts have also been aimed at fabrication of heterojunctions and heterostructures of 2D materials and organic molecules, such as perylene-diimide or phthalocyanine, with diverse applicability [308,309].

Raman and PL spectra are both affected by functionalisation. A strong enhancement of the Raman spectra of copper phthalocyanine placed on the surface of graphene was observed in comparison to MoS_2 and hBN [310]. PL of MoS_2 can be enhanced by more than

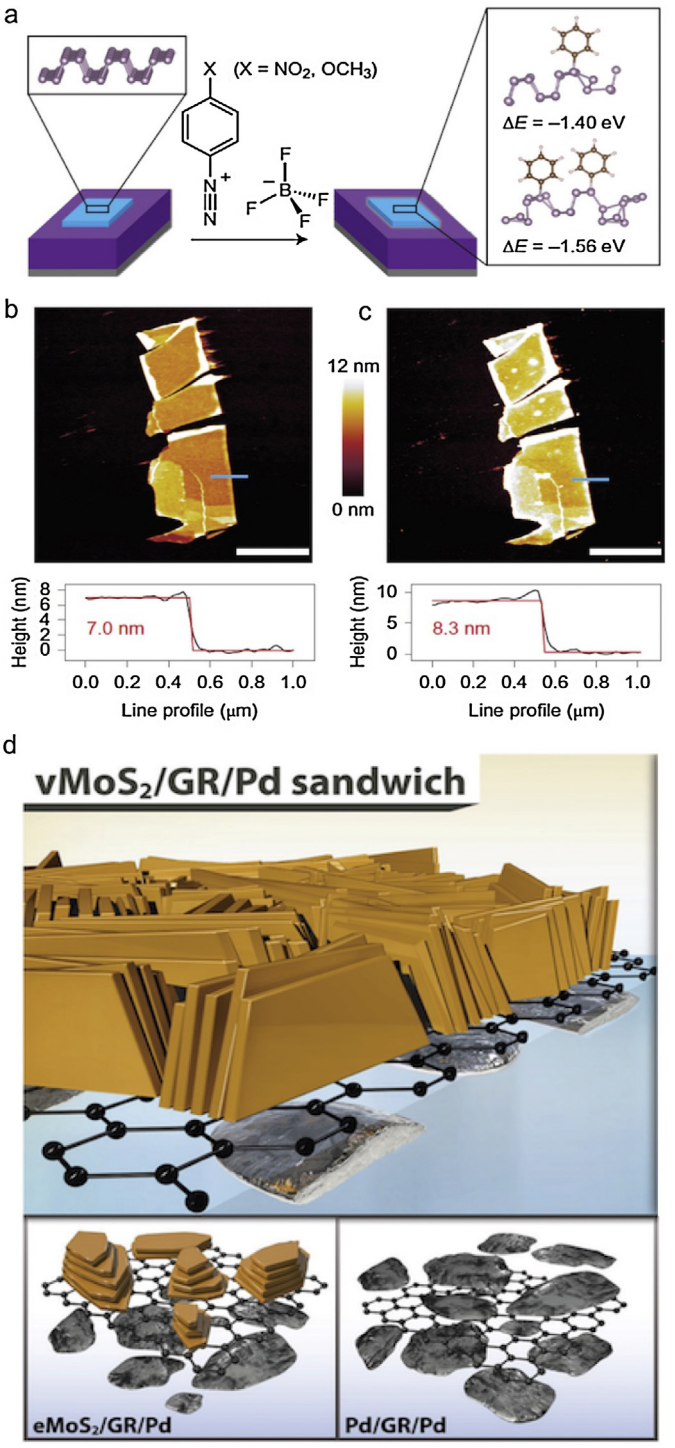

Fig. 16. Functionalisation of 2D materials and their composites. a, Aryl diazonium functionalisation of thin black phosphorus. Left: schematic of pristine black phosphorus structure on an SiO_2/Si substrate, right: schematic of functionalised black phosphorus. b–c, Corresponding AFM images of thin black phosphorus before and after functionalisation, respectively, showing the increase in height due to the aryl diazonium layer. d, Schematics of various composites of MoS_2, graphene (GR), and metal NPs, prepared using ITIES, top: asymmetric vMoS_2/GR/Pd NP composite, bottom-left: asymmetric eMoS_2/GR/Pd NP composite, bottom-right: symmetric Pd NP/GR/Pd NP composite. Figures adapted with permission from: a–c, [307] © 2014 Nature Publishing Group. d, [314] published by John Wiley and Sons under CC-BY licence.

two orders of magnitude by chemical treatment using an organic acid bis(trifluoromethane) sulphonimide, leading to more than 95% quantum yield and long (~11 ns) exciton lifetime [311]. It was proposed that this treatment passivates defects in MoS_2 and therefore suppresses the defect-mediated non-radiative recombination of the photogenerated electron-hole pairs. Similar approach was adopted to repair the ubiquitous sulphur vacancies in MoS_2 by chemical treatment with thiosilanes [179]. Furthermore, an asymmetric Janus functionalisation of both sides of a 2D material has been conceived for development of thin devices with multiple functionalities, showing that modification of one side significantly affects behaviour of the other [312].

Another avenue to enhance the performance of TMDCs is through heterostructures or composite materials. Combining TMDCs with other materials of high available surface area and high conductivity, such as graphene or carbon nanofibres, is used to produce composite materials with high HER activity ($b \sim 38–77$ mV dec^{-1}) [270,271,276] and good supercapacitive performance [111]. Metal NPs were also employed in functionalisation of 2D materials with focus on applications in fuel cells, supercapacitors, and catalysis [313–316]. In contrast to the "conventional" solid/liquid electrochemical configuration, an assembly of a 2D material and/or NPs at polarisable liquid/liquid interface can also be used for the HER. The interface between two immiscible electrolyte solutions (ITIES) is a special class of a liquid/liquid interface, where the presence of electrolytes, redox mediators, and the relative hydrophilicity and hydrophobicity of the two liquid phases, provide an accurate control over both electron and ion transfer [317]. ITIES has initially been employed for the assembly and HER/capacitance evaluation of MoS_2 and WS_2 nanosheets [318,319], and further advances have been made by Toth et al. towards asymmetric functionalisation of graphene with several metal NPs [315]. This work has been recently extended to various composites based on LPE MoS_2 (eMoS_2), vertically-aligned edge-terminated MoS_2 (vMoS_2), graphene, and metal NPs as shown in Fig. 16d [314]. Electrochemical assessment of these various "sandwich-like" composites revealed that the vMoS_2/graphene/Pd NP composite exhibits the highest HER activity and capacitance, in comparison to other configurations.

MoS_2 has been extensively studied for application in supercapacitors using various media and electrolytes [97,111,186], including vertically-aligned MoS_2 nanosheets, which exhibited high capacitance values sustained up to 100 Hz [175]. Recent work by Bissett et al. compared performance of MoS_2, $MoSe_2$, WS_2, and 1T-TiS_2 in a supercapacitor coin-cell using cyclic voltammetry and electrochemical impedance spectroscopy, pinpointing the semimetallic 1T-TiS_2 as the most promising material due to the highest capacitance and low mass density [97]. Significant advances in inkjet printing using 2D materials and their heterostructures are underway for fabrication of flexible electronics, dielectric capacitors, photosensor arrays, and logic memory devices [320–322].

5. Future perspectives

5.1. Exotic 2D materials

Here we will review less common 2D materials, which have been studied either experimentally or theoretically and show potential in a range of applications including electrochemistry. Table 5 compares the charge carrier mobilities of some of these materials. Group 4 TMDCs were of initial interest for PECs due to the high abundance of group 4 metals but their photoanodic instability, related to the mixed hybridisation of the *d* and *p* valence orbitals of the metal and chalcogenide, deems them less attractive [217]. 1T-HfS_2 has a bulk indirect band gap of 2.0–2.1 eV [70,323], which is predicted to decrease to 1.2 eV in monolayer [71], and has successfully been used in ~6-layer FET device with $>10^4$ on/off ratio [162]. 1T′-ReS_2 is a direct band gap semiconductor, in which the individual 2D layers are electronically decoupled, leading to only negligible shifts in the Raman and PL spectra [163]. Vanadium-based TMDCs, which are metallic, exhibit general electrochemical instability and somewhat poor HER activity, correlated with the chalcogenide size [295]. 1T′-PtS_2 has recently been shown to be extremely sensitive to the number of layers, with the band gap changing from 0.25 eV in bulk to 1.6 eV in monolayer (Fig. 17a and b) [161], showing inconsistency with earlier reported values [213,324]. Interestingly, the E^1_{2g} and A_{1g} mode thickness dependence in 1T′-PtS_2 is exactly reversed to that of MoS_2 as shown in Fig. 17c. Photoelectrochemical potential of 1T′-PtS_2 was also recognised early, with both HER and OER activity, remarkable photoanodic stability, and negligible platinum and sulphur "leaching" into the surrounding solution [217]. In dark, 1T′-PtS_2 behaves similarly to Pt metal with the obvious advantage of much lower density. Electrochemistry of Pt-based chalcogenides depends on the chalcogenide size (HER is shown in Fig. 17d–f), following the semiconducting/semimetallic/metallic progression in PtS_2/$PtSe_2$/$PtTe_2$ [325]. Temperature-dependent transitions between semiconducting, metallic, and superconducting phases are common for many TMDCs such as TaS_2 and $NbSe_2$, or $MoTe_2$ [24,46,134], which limits a direct comparison of different studies.

Table 5
Band gaps and charge carrier mobilities of less common 2D materials.

2D material	Band gap (eV)		Mobility (cm^2 V^{-1} s^{-1})	
	Bulk (>10 layers)	1–2 layers	Bulk (>10 layers)	1–3 layers
1T'-PtS_2	0.25	1.60	80	0.1
Phosphorene	0.31	1.45	>4000	1–1200
SnS	0.92	1.69	20	–
InSe	1.26	1.87	~2000	~1000
1T-HfS_2	1.96	1.23	0.1[a]	1833
4H-SnS_2	2.28	2.03	1.5–230	50

Data collected from the following references: [70,71,144,161,162,164,184,228,328–330,334]. All values were obtained at room temperature except for the phosphorene mobility (4 K).
[a] 6 layers.

Chalogenides of group 13–15 post-transition metals and metalloids have also been studied. Tin sulphides with potential for photocatalysis and photovoltaics have recently been prepared by CVT and LPE [326–328] but questions remain about the detrimental effects of the band alignment in mixed-valence tin states on their photovoltaic efficiency [184]. 4H-SnS_2 was shown to be an indirect semiconductor for all thicknesses, with only a weak dependence of the electronic band structure on the number of layers [164,329]. SnS is also an indirect semiconductor but it has a band gap increasing by >0.7 eV in bilayer in comparison to bulk and exhibits an anisotropic mobility transport [328,330] also observed for phosphorene (below). SnS_2 and SnS both have a low HER activity and suffer from significant non-stoichiometry due to the different oxidation states of Sn, as revealed by the XPS [283]. GaS nanosheets were also prepared by LPE and HER activity ($b \sim 85–106$ mV dec^{-1}) dependent on their lateral size was observed [96]. Bulk GeS and GaSe exhibit much poorer HER activity ($b > 150$ mV dec^{-1}) and no OER activity, however, bulk GaSe possesses some ORR activity, fast HET for $[Ru(NH_3)_6]^{3+/2+}$ and $[Fe(CN)_6]^{3-/4-}$, and remarkable electrochemical stability over a large potential window, attributed to surface passivation by oxidation [284]. Topological insulators (TIs) are materials whose bulk interiors are insulating but their surface or edges harbour metallic states due to the strong spin-orbit effects [2]. They have a vast potential for a range of applications, where no charge transfer is required in the *c*-axis direction but surface or edge conductivity needs to be maintained, such as deposition smart

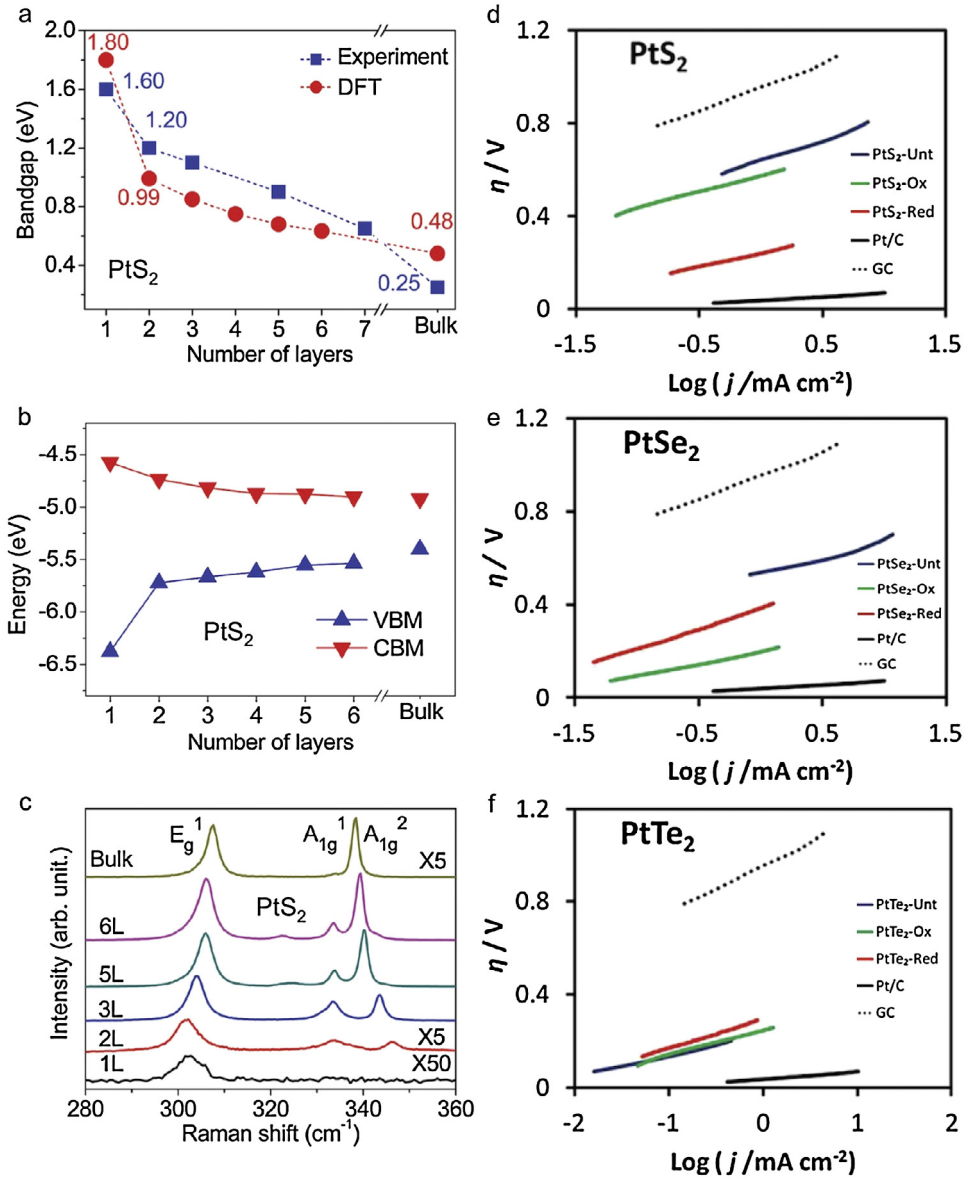

Fig. 17. Platinum-based TMDCs. a, Dependence of the 1T′-PtS_2 band gap on the number of layers determined from the Tauc plot (blue) and DFT calculations (red). b, Dependence of the VBM and CBM of 1T′-PtS_2 on the number of layers calculated using DFT. c, Evolution of the 1T′-PtS_2 Raman spectrum with thickness. d–f, Tafel plots of the HER activity of 1T′-PtS_2, 1T′-$PtSe_2$, 1T′-$PtTe_2$, respectively. The -Unt, -Red, and -Ox suffixes correspond to the untreated, reductively pretreated, and oxidatively pretreated crystals. Figures adapted with permission from: a–c, [161] © 2016 John Wiley and Sons. d–f, [325] © 2016 John Wiley and Sons.

paints, corrosion protection, and transparent conductive layers. Bi_2Se_2 and Bi_2Te_3 are examples of TIs with complex electrochemical redox activity and poor HER activity [109]. A simple chemical functionalisation of a bulk, mixed-element TI $Bi_{2-x}Sb_xTe_{3-y}Se_y$ using a fluoro-derivate of quinone allowed to create in-plane p-n junctions on its surface [331].

The elemental 2D materials from group 14 (beyond carbon), which include silicene, germanene, stanene, and plumbene, are notoriously hard to isolate and/or synthesise, although their crystal and electronic band structures were predicted by theory [12,332,333]. The limited efforts to synthesise these materials suggest that low yield, small lateral size, and poor stability currently deems them unsuitable for other than fundamental research [130–132]. Stanene and plumbene have also been identified as TIs, with their electronic structure being tuneable by chemical functionalisation [332,333].

Many layered materials are unstable in their mono- and few-layer form and suffer from degradation when exfoliated in air. Phosphorene, $NbSe_2$, $MoTe_2$, or 1T′-WTe_2 are examples of such 2D materials [86,100,249,334]. Cao et al. developed a fully motorised process of 2D materials exfoliation and their encapsulation by protective hBN layers under an inert atmosphere [334]. The authors detected superconductivity in $NbSe_2$ all the way down to a monolayer thickness, which was previously impossible due to its degradation in air. The same approach was used to study otherwise unstable few-layer InSe to find its very high mobility of $\sim$1000 $cm^2\ V^{-1}\ s^{-1}$ at room temperature [228]. InSe monolayer, which is four-atom thick, was not conductive due to degradation or increased Schottky barrier at the contact, however, strong increase of the band gap size in monolayer and bilayer in comparison to bulk (>0.6 eV) was observed in the PL spectra. A separate study in air revealed that this direct-to-indirect band crossover commences in as many as 20 InSe layers [128,335], much thicker than in most TMDCs (<5 layers) [63]. Phosphorene, which forms buckled zig-zag layers (Fig. 1c), also degrades strongly in air. The large increase of the direct band gap from $\sim$0.3 eV in bulk black phos-

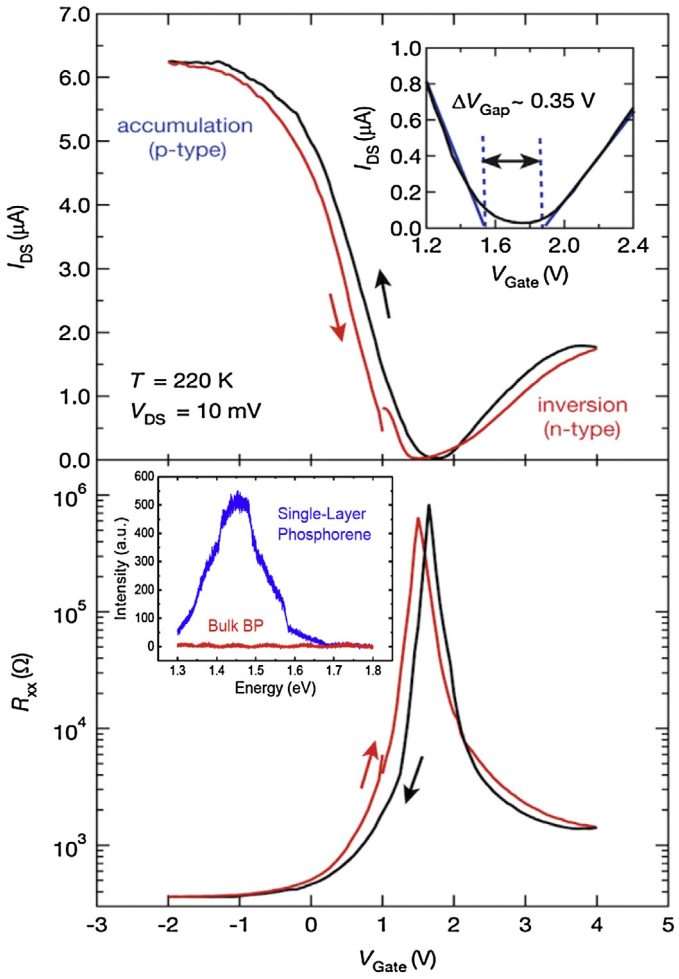

Fig. 18. Black phosphorus and phosphorene. Transport characteristics of bulk black phosphorus (20 nm thickness) by ionic liquid gating showing its ambipolar behaviour. Top panel: current–voltage curves, top inset: band gap determination from the threshold voltage, bottom panel: 4-probe resistance curves, bottom inset: comparison of the bulk and monolayer PL spectra indicating the direct band gap in monolayer phosphorene. Figure reproduced with permission from: [337] © 2015 American Chemical Society, the bottom inset reproduced from [144] © 2014 American Chemical Society.

phorus to ~1–2 eV in mono- and few-layer phosphorene, which is caused by the lack of interlayer hybridisation in thin layers, is reflected in the thickness-dependent Raman spectrum and monolayer PL emission in the near-IR region (bottom inset in Fig. 18) [99,144,336]. Unusually, the changes in the electronic band structure also begin in a relatively thick material, >20 layers [100]. Phosphorene exhibits a unique anisotropic mobility behaviour, in which the electrons and holes have different masses depending on the direction in the Brillouin zone [144]. Related strong absorption along the armchair lattice direction in contrast to optical transparency along the zig-zag lattice direction was predicted by the theory [336]. Electrochemically-gated FET of bulk phosphorus reveals an ambipolar behaviour, similar to graphene, with both p-type and n-type conductivity depending on the voltage polarity as shown in Fig. 18 [337]. Furthermore, few-layer LPE phosphorene acts as a spontaneous PEC when mediated by suitable organic molecules and the lifetime of its photogenerated excitons increases linearly with the lateral size of the nanosheets [338].

Other layered materials proposed for future preparation in 2D include transition metal oxides, metal halides, covalent organic frameworks, and perovskites [10–12,14].

5.2. Heterostructures of 2D materials

The research on heterostructures of 2D materials is driven by the potential of creating enormous diversity in properties and functionality on a vanishingly small scale. Synergistic effects in these heterostructures are promising both for improvements of existing applications and for discoveries of completely new phenomena [22,38,93]. Traditionally, alloys of different materials have been used in electronic structure engineering but the high defect density in such devices is very challenging. Continuous tuning of the PL peak energy in $MoS_2/MoSe_2$ alloys between 670 and 795 nm is an example of such approach [114].

Vertical vdW heterostructures are formed by stacking of different 2D materials on top of each other and are held together by the same vdW forces, which act in naturally layered materials. Resulting ultrathin, smooth material junctions are crucial for the operation of devices with sub-nanometre thickness, charge transfer across the vdW interface, and observation of interlayer excitons. The lack of SC depletion/accumulation regions due the lack of physical material space in the *c*-axis direction makes these structures very unique. For example, the spatial proximity of two graphene sheets separated by monolayer hBN implies that individual tuning of the electronic structure of two charge carrier populations occupying virtually the same plane is achievable [14]. Furthermore, the typical distance between charge carriers in graphene is ~10 nm and so their vertical proximity between the two different layers is much smaller [22]. The molecular orbitals of 2D materials extending in the *c*-axis direction imply that the effective electronic band structure of vdW heterostructures is highly sensitive to the crystallographic alignment between the individual 2D layers, i.e. the "twist-angle", also manifested in a moiré pattern in the case of small (<2%) lattice mismatch [14,136]. Crucially, a self-cleaning of vdW heterostructures was found, whereby the ubiquitous carbonaceous contamination is "squeezed" out to microscopic bubbles thanks to the strong affinity between the 2D layers [14,22,139].

Construction of vertical p-n junctions with a sharp voltage drop at the interface of the two materials leads to tunnelling-mediated recombination between majority charge carriers as demonstrated for MoS_2/WSe_2 vdW heterostructures [339]. Flexible photovoltaic device based on graphene/TMDC/graphene vdW heterostructure with external quantum efficiency of 30% were constructed by Britnell et al. [138]. Withers et al. engineered light-emitting devices with TMDCs quantum wells encapsulated by hBN as a tunnelling barrier and graphene as a transparent conductive layer for the charge extraction and demonstrated efficient PL and electroluminescence, as well as the use of elastic polymer substrates for applications in flexible optoelectronics [27]. Effective charge collection was achieved in InSe/graphene heterostructures with a strong photocurrent response across the visible and near-IR spectra [340]. InSe/GaSe heterojuctions with strong electroluminescence emission at room temperature were also fabricated [127].

Separation of the photoexcited electron-hole pairs into interlayer excitons is observed in $MoSe_2/WSe_2$ heterostructures (Fig. 19a–d) with much longer lifetime (~1.8 ns) than in the individual 2D materials [341]. With the application of a negative gate voltage, the band alignment offset is suppressed (Fig. 19e–f), and hence the resulting exciton energy increases and charge injection becomes more efficient, as shown in Fig. 19g by the increase in PL energy and intensity. Hong et al. demonstrated very fast (~50 fs) carrier separation in photo-excited MoS_2/WS_2 vdW heterostructures, which was made possible by the suitable alignment of the electronic band structure of the individual 2D materials [342]. A similar concept of PL tuning by hBN mono- and few-layer tunnelling barriers was shown for MoS_2/WSe_2 [136]. Theoretical calculations suggest that sub-nanometre thick MoS_2/graphene and MoS_2/WS_2 heterostructures can be effective Schottky barrier- and excitonic-

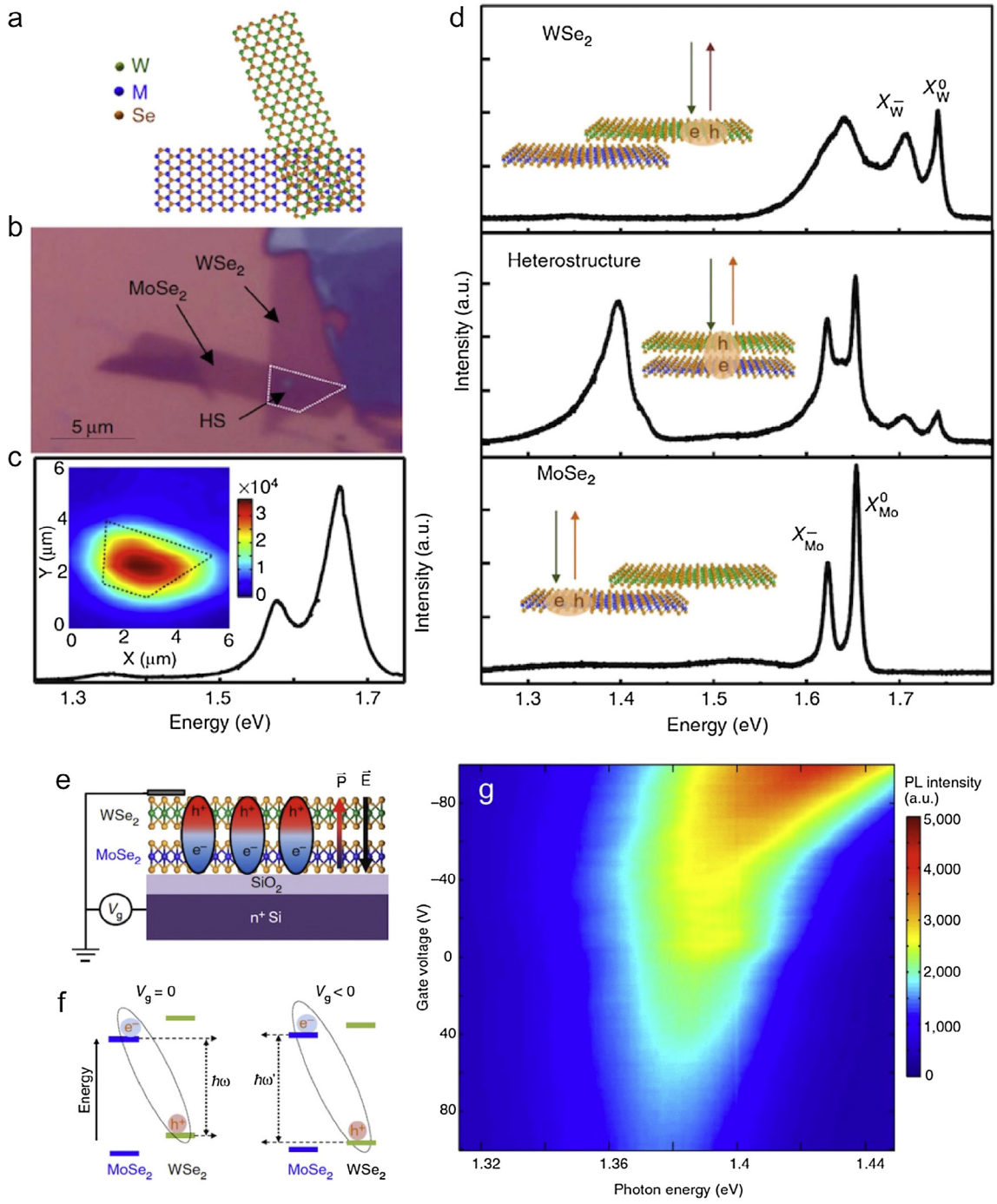

Fig. 19. Vertical vdW heterostructures of 2D materials. a, Schematic of a vdW heterostructure composed of $MoSe_2$ and WSe_2 monolayers. b, Optical image of the heterostructure. c, Room temperature PL spectrum (2.33 eV excitation) of the heterostructure with the inset showing a spatial map of the PL intensity. d, Comparison of the PL spectra from monolayer WSe_2 (top), heterostructure (middle), and monolayer $MoSe_2$ (bottom) at 20 K. e, Schematic showing the electrostatic back-gate tuning of the interlayer excitons. f, Schematic showing the corresponding tuning of the $MoSe_2/WSe_2$ band alignment. g, PL spectra intensity/energy plotted as a function of the gate voltage. Figure adapted with permission from [341] © 2015 Nature Publishing Group.

photovoltaic cells, respectively, with the conversion efficiency of ~1%, further increased by multiple stacking [25].

In-plane lateral 2D heterostructures of several TMDCs, where all the 2D materials occupy the same plane, were also successfully synthesised [121,181] and PL emission spatially tuneable between 760 and 790 nm within a monolayer of $MoSe_2$–WSe_2 with the maximum integrated intensity at the heterostructure interface due to defect-mediated recombination (Fig. 20a and b) was realised [181]. Another study has shown a characteristic diode behaviour with an opposite, voltage-dependent photoresponse in monolayer WSe_2–MoS_2 lateral heterostructures using a photocurrent spectral AFM (Fig. 20c and d) [343].

A special group of vdW heterostructures are newly emerging naturally occurring mixed-metal chalcogenides. These include rare minerals such as franckeite ($Pb_5Sn_2FeSb_2S_{14}$), cylindrite ($Pb_3Sn_4FeSb_2S_{14}$), and menghinite ($Pb_{13}CuSb_7S_{24}$), with band gaps of 0.65–1.44 eV lying between the band gaps of their binary sulphide constituents [344]. A recent work by two different groups have shown that franckeite natural heterostructure consists of a repeated pattern of two distinct layers (Fig. 21a–c) and it is possible

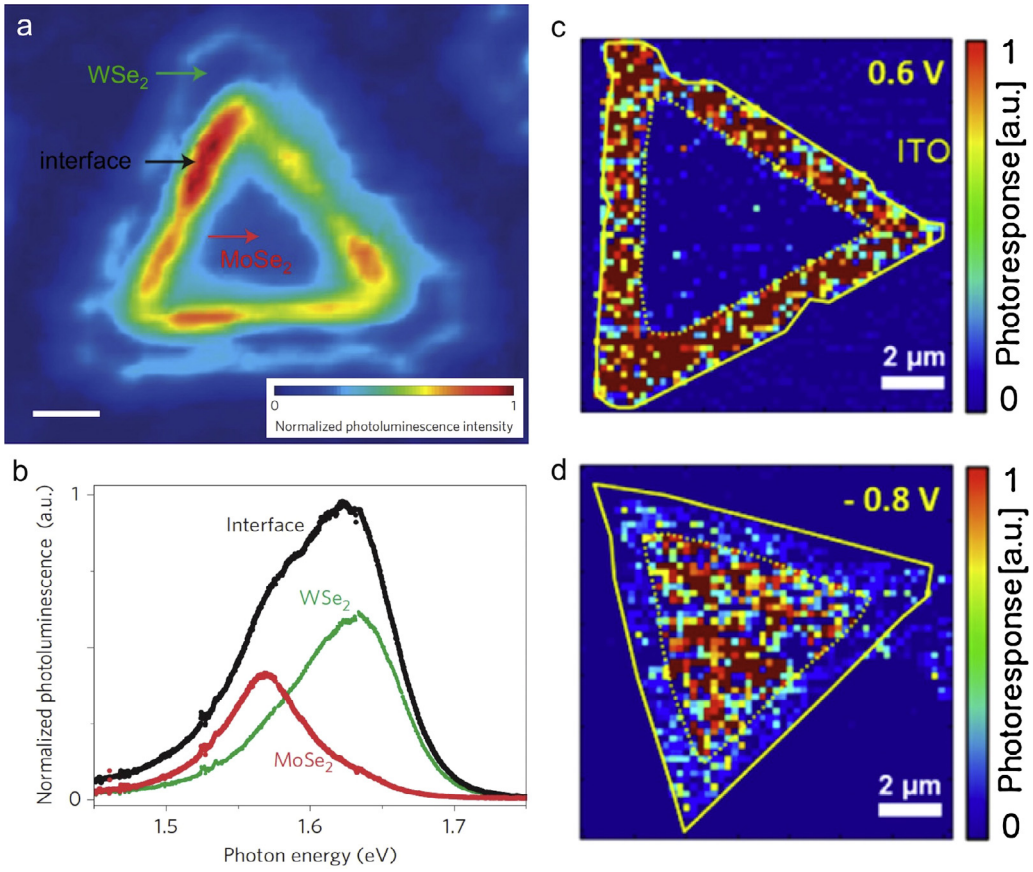

Fig. 20. Lateral heterostructures of 2D materials. a, Room temperature PL intensity map of a WSe_2–$MoSe_2$ lateral heterostructure (SEM and TEM images of which are shown in Fig. 5e and 5f, respectively) using 2.33 eV excitation. b, Corresponding PL spectra from monolayer WSe_2, monolayer $MoSe_2$, and their interface. c–d, Photoresponse of a WSe_2–MoS_2 lateral heterostructure at forward (+0.6 V) and reversed (−0.8 V) bias voltage, respectively. Figures adapted with permission from: a–b, [181] © 2014 Nature Publishing Group. c–d, [343] © 2016 American Chemical Society.

to exfoliate it down to a monolayer thickness [98,345]. The extensive characterisation revealed a p-type semiconducting nature of franckeite (Fig. 21d) and a narrow band gap of ~0.7 eV. Furthermore, its inherently high capacitance (Fig. 21e) and HET rate could be exploited in the electrochemical storage and conversion applications.

5.3. Tuneability of 2D materials

The sub-nanometre dimensions of 2D materials imply that their properties, unlike those of their bulk counterparts, are strongly sensitive to external electrical, mechanical, and optical factors, which offers new attractive strategies in the engineering of tuneable devices [135].

Electric field offers an effective way of tuning the electronic structure of 2D materials. While only limited band gap engineering has been achieved in bilayer and trilayer graphene [346,347], theoretical calculations predict that electric fields larger than 2 V Å^{-1} decrease the band gap in monolayer group 6 TMDCs until finally rendering the material metallic for fields >4.5 V Å^{-1}, as it is shown in Fig. 22a [191]. Sulphides require larger fields than selenides to induce similar changes while much smaller difference is observed between Mo and W. These effects also depend on the direction of the electric field and number of layers [348]. The dielectric constant of trilayer and thicker MoS_2 was also predicted to increase with the increasing electric field (>0.01 V Å^{-1}) and MoS_2 thickness [349]. Band gap tuning of bilayer MoS_2 was achieved experimentally in a dual-gate FET with an indirect band gap reduction of ~260 meV per 1 V nm^{-1} observed by PL [350]. In contrast, the direct band gap of monolayer MoS_2 remained constant.

Reduction of the exciton binding energies was achieved in a monolayer WS_2 FET device operating at high carrier densities (~10^{13} cm^{-2}), leading to an increase in the effective dielectric screening and suppression of the interaction between the charge carriers [55]. The absorption, reflectance, and PL spectra composed of excitons and trions (stable at room temperature) can therefore be tuned by the gate voltage as shown in Fig. 22b–e for MoS_2 [55,58]. At high optical fluxes and positive bias voltage, the excess of photogenerated excitons binds to electrons to form negative trions, thus increasing the effective mass of the charge carriers. This also leads to negative photoconductivity as observed by terahertz spectroscopy [351]. These effects are short-lived in low-quality materials due to scattering and non-radiative losses but are of increasing importance in high-quality 2D materials.

Electrochemical top-gating is becoming a popular way of controlling transport measurements in 2D materials. The main advantage of the electrochemical gating is the large electric field up to 10^7 V cm^{-1} condensed at the 2D material/liquid interface due to the sharp and localised voltage drop, which is not affected by the losses due to scattering or charge trapping as it is the case in conventional back-gate dielectrics such as SiO_2 [352]. In the case of semiconductors, the Schottky barrier is squashed to a nanometre width and the electron tunnelling becomes the main charge injection mechanism [353]. Due to the large electric double-layer capacitance, C (typically between 1 and 10 μF cm^{-2}), the applied gate voltage, ΔV_{gate}, is virtually equal to the change in the Fermi level, ΔE_F [337,352]:

$$e\Delta V_{gate} = \Delta E_F + \Delta\phi = \Delta E_F + \frac{e^2 n}{C} \quad (2)$$

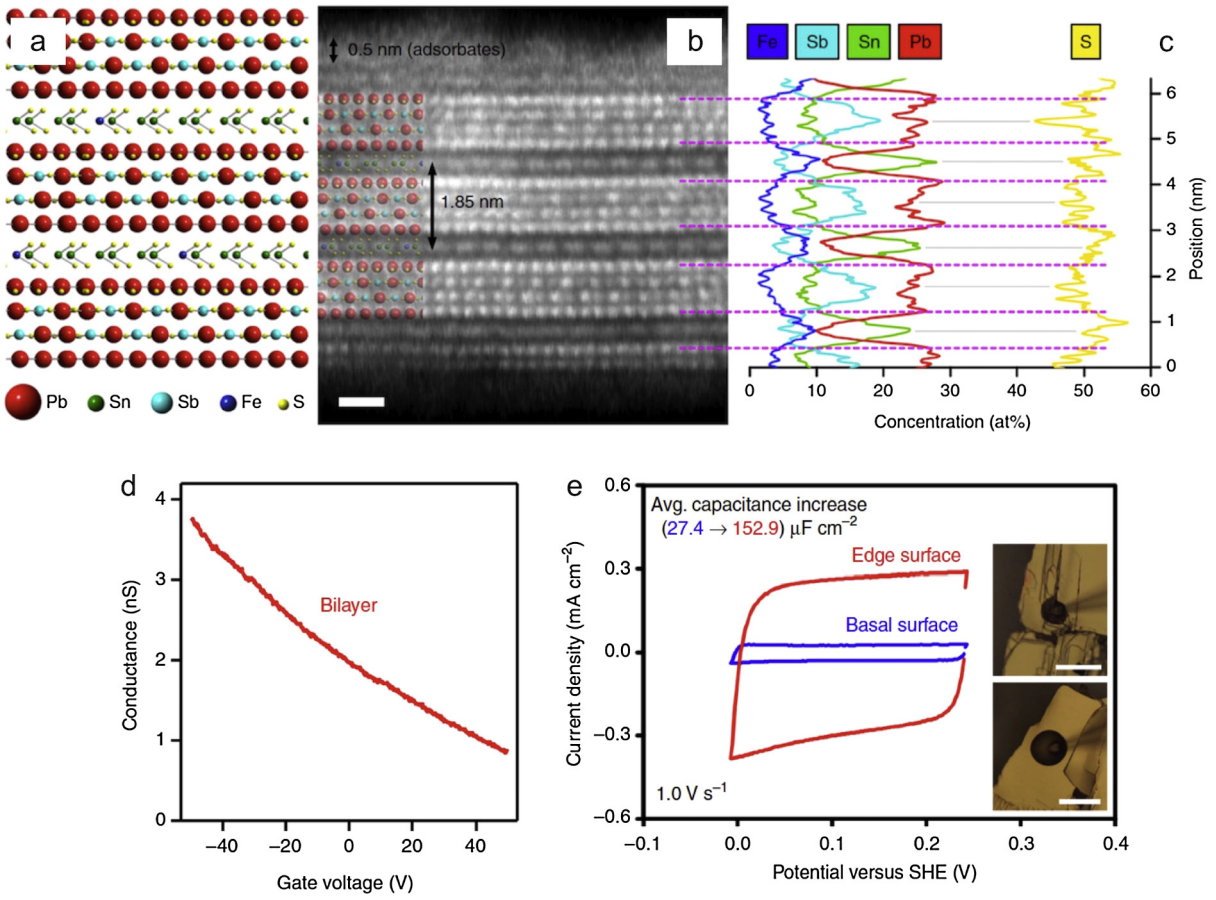

Fig. 21. Natural vdW heterostructures. a, Schematic side-view of franckeite heterostructure. b, Atomic-resolution HAADF-STEM image of franckeite showing the layered heterostructure composed of alternating Pb-/Sb-rich and Sn-/Fe-rich sulphide layers. c, Corresponding elemental concentration profile determined from STEM-EDXS. d, Conductance of bilayer franckeite as a function of gate voltage showing its p-type semiconducting nature. e, Comparison of the interfacial capacitance between the edge and basal plane surface of franckeite determined by cyclic voltammetry (microdroplet electrochemical cells used for the measurement are shown in the insets). Figure adapted from [98], published by Nature Publishing Group under CC-BY licence.

where $\Delta\phi$ is the change in the electrostatic potential and all other symbols have the meaning defined previously. This further means that high charge carrier densities of 10^{13}–10^{14} cm^{-2} can be achieved using a relatively small voltage, typically up to ~4–6 V, and the carrier mobility can be greatly enhanced by several orders of magnitude through dielectric screening of Coulomb scattering on charged impurities [50,54,162,353]. Ionic liquids or polymer electrolytes such as $LiClO_4$ in polyethylene glycol electrolyte are the most commonly used gate liquids, which withstand the application of large voltages up to 6 V [35,54,337]. Low-temperature measurements by "gate-freezing" of the electrolyte at certain voltage, previously applied at room temperature, were also performed [354]. Evidence suggests that aqueous systems improve both on/off ratios and mobilities in FETs [35,164] providing the water evaporation is overcome by the use concentrated electrolytes [89,355]. Electrochemical gating has also been successful in tuning of the PL intensity and makeup, from the negative trions at positive gate voltage, to neutral excitons near neutrality point, and finally positive trions at negative gate voltage using an ionic liquid gel on monolayer WSe_2 [352]. Similar strategy was employed for an MoS_2/graphene heterostructure, where the PL intensity was tuned by two orders of magnitude and the exciton/trion intensity ratio changed 30-fold using voltage of ~4.5 V [356].

The extreme thinness of 2D materials renders them very sensitive to strain/stress and the new concept of "straintronics" has been probed both theoretically and experimentally [62,135,170,190]. The effect of strain in 2D materials on a suitable flexible polymer substrate can directly be observed by Raman spectroscopy. Applying uniaxial tensile strain, Rice et al. observed only a negligible redshift in the A_{1g} out-of-plane Raman mode frequency of mono- and few-layer MoS_2 in contrast to significant redshifts (−2.1 cm^{-1}/1% strain) in the E^1_{2g} in-plane mode, in agreement with the theoretical prediction [169]. Much larger Raman blueshifts were observed for biaxially, compressively strained trilayer MoS_2 on a piezoelectric substrate along with a large increase in the PL energy and intensity of the direct transition PL peak (300 meV/1% strain) due to the increased radiative recombination of the charge carriers [168]. Conley et al. found that the uniaxial strain in monolayer MoS_2 reduced the PL intensity and redshifted the PL peak energy by 45 meV/1% strain, while the bilayer PL intensity stayed constant and its PL peak energy redshifted by 120 meV/1% strain (Fig. 23a and b) [357]. This indicates that the indirect band gap closes faster than the direct one and that monolayer MoS_2 becomes an indirect semiconductor even when only small strain is applied. Peña-Álvarez et al. used an anvil cell to induce vertical compressive stress in monolayer MoS_2 without the need of stress transfer media, which normally reduces the efficiency of the process [171]. The E^1_{2g} and A_{1g} Raman modes of MoS_2 significantly broadened and their frequencies increased by 20 cm^{-1} when ~5 GPa of pressure is applied (Fig. 23c), and the PL was shut down almost immediately after the initial compression. These largely reversible effects, confirmed by the DFT calculations, suggested a direct-to-indirect band gap transition for pressures as low as ~0.5 GPa (Fig. 23c), eventually leading to completely metallic character at ~3 GPa, confirming the previous study [357]. Prediction for monolayer $MoSe_2$ showed

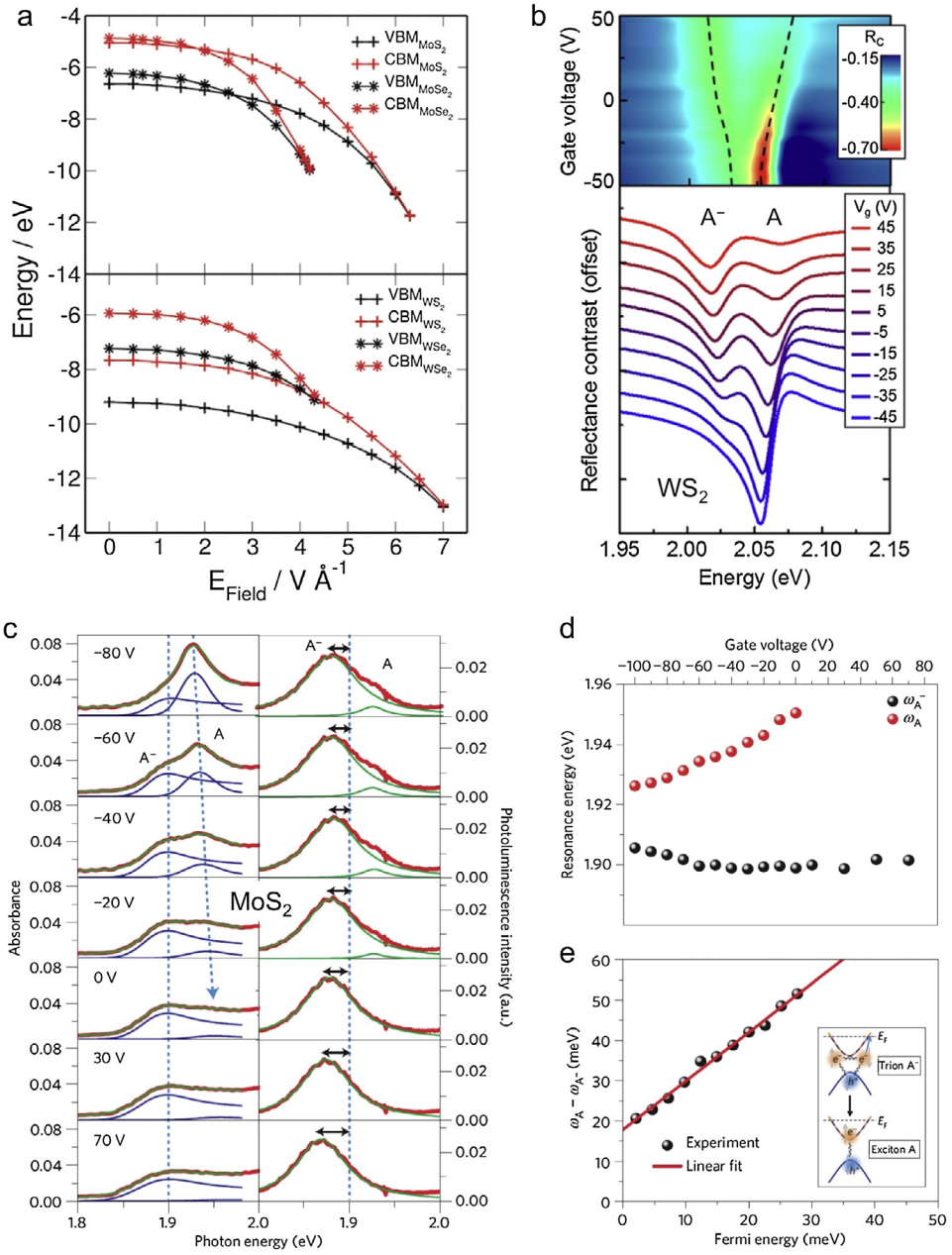

Fig. 22. Tuning of 2D materials' properties by electric field. a, Changes in the electronic band structure of TMDCs with the increasing strength of the external electric field, expressed by the VBM and CBM. b, Tuning of the neutral exciton (A) and negative trion (A^-) ratio in monolayer WS_2 by the gate voltage, expressed by the reflectance contrast spectra. c, Tuning of the A and A^- ratio in monolayer MoS_2 by the gate voltage, expressed by the absorbance and PL spectra. d, Resonant energies of the exciton and trion determined from the absorbance spectra, e, Trion binding energy determination from the exciton-trion energy difference. Figures adapted with permission from: a, [191] © 2014 The Royal Society of Chemistry. b, [55] © 2015 American Physical Society. c–e, [58] © 2012 Nature Publishing Group.

that although its band gap decreases with biaxial tensile strain, it remains direct until ~3% strain followed by a crossover towards an indirect band gap of ~0.9 eV at 7% strain [358]. Furthermore, simple bending of bilayer MoS_2 has been predicted to electronically decouple its two monolayers, which then become individually tuneable by the applied strain [19].

Tunnelling current control is an important challenge for the ever-decreasing size of transistors and other circuit elements in modern electronics. The use of high permittivity materials such as HfO_2 or Al_2O_3 is necessary to prevent leakage currents, which occur when the thickness of conventional transistors is reduced [13]. Insulating hBN with its 5.8–6.0 eV band gap also falls into this high-permittivity category. hBN has already been used as an atomically-thin tunnelling barrier with few inherent defects and high breakdown voltage, and as an encapsulating dielectric leading to a significant increase in mobility of 2D materials [359–362]. Tunnelling FETs based on electron tunnelling through a quantum mechanical barrier rather than thermionic emission are therefore of increasing interest due to the shorter on/off switching times and low leakage current [38]. The use of a 2D insulator as a tunnelling barrier on a conducting substrate is particularly interesting for electrochemistry since it can "shut-down" the surface chemistry yet still allow for an effective HET through the 2D insulator.

Sensitivity of 2D materials to external stimuli can be exploited to tune their electronic properties, create on-demand functionalities, and harness or convert energy. There is no reason why the outlined approaches should not be attempted in exploration of tuneable electrochemical applications, given that the manipulation of the electronic band structure directly affects key electrochemical properties, such as electron transfer, capacitance, and electrocatalytic

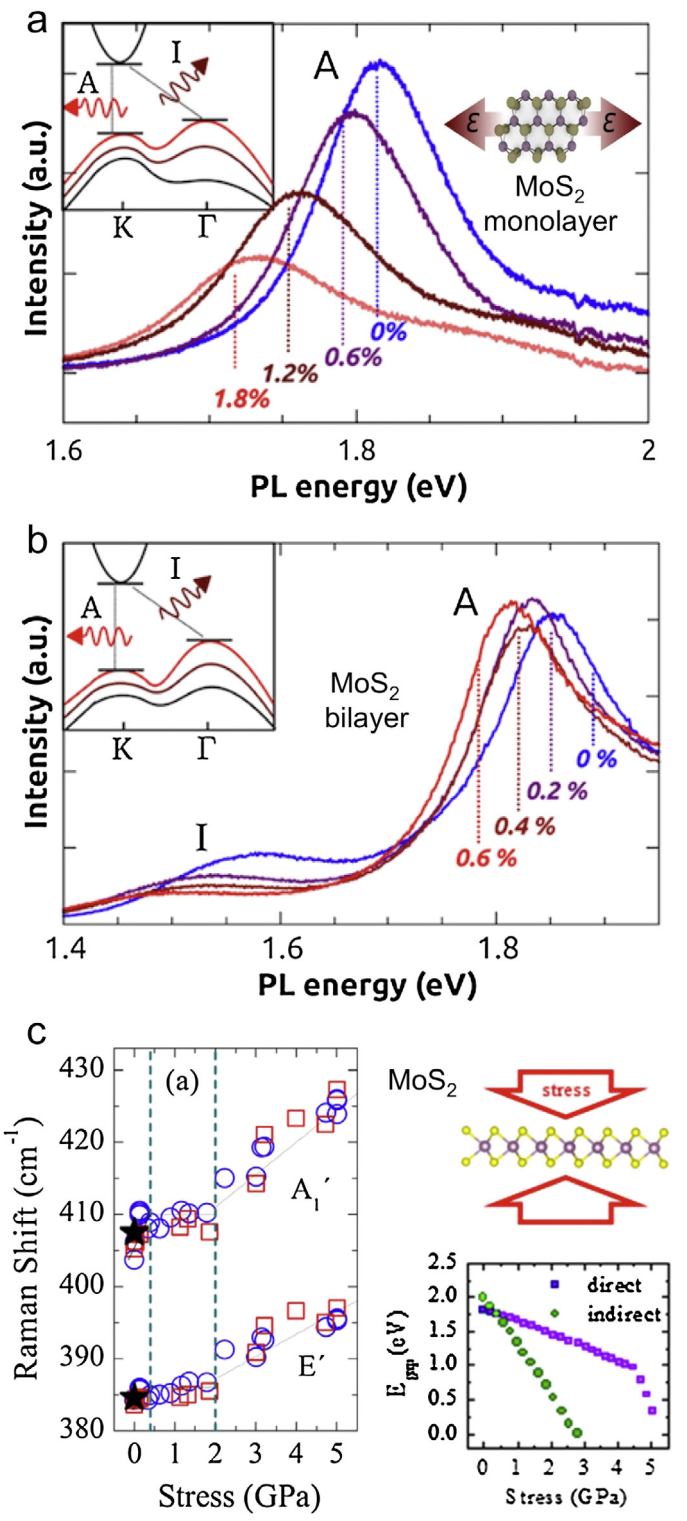

Fig. 23. Tuning of 2D materials' properties by strain. a–b, Tuning of the PL spectrum using tensile strength in monolayer and bilayer MoS_2. c, Raman spectra shifts in monolayer MoS_2 (left), and the direct and indirect band gap determined from DFT (bottom-right) as a function of vertical compression stress (schematically shown in top-right of the figure). Figures adapted with permission from: a–b, [357] © 2013 American Physical Society. c, [171] © 2015 American Physical Society.

activity. Advances in these research frontiers could likely lead to a development of new branches of electrochemistry.

5.4. Wetting and electrowetting

Wetting refers to the interaction between a liquid and solid phase and is described by the contact angle between the two. The lower the contact angle, the more the solid and liquid "like each other". In the case of a large contact angle, the liquid is repulsed by the surface of the solid and their contact area is minimised.

Significant debate surrounds the so-called "wetting-transparency" of graphene, referring to a phenomenon in which the contact angle of an ultrathin solid is affected by the underlying substrate. In other words, the liquid "feels" the substrate through a wetting-transparent material and the surface tension and contact angle adjust accordingly. Theoretical, computational, and experimental arguments both for [193] and against [195,244] this hypothesis, as well as an evidence of the wetting transparency breakdown at high and low contact angles [363] have been reported. Little is known about the contact angle dependence on thickness as both its increase [119,193] and decrease [194,364] with the increasing number of layers was observed or predicted for graphene, MoS_2, and WS_2. Strong hysteresis between the receding and advancing contact angles and surface pinning of the liquid suggest that static measurements alone are unreliable and dynamic measurements should be also employed [195]. The analysis of the interplay between the interaction potentials and relative hydrophobicity vs. hydrophilicity in the water-graphene-substrate system has led to a term "wetting-translucency", which more accurately grasps the complex nature of the wetting phenomenon on atomically-thin materials [194].

Electrowetting is a dynamic phenomenon, which occurs when the voltage is applied between a solid electrode and liquid phase. This increases the interfacial capacitance, which "pulls" the liquid closer to the solid, thus decreasing the contact angle and increasing the wetting. Traditionally, a layer of dielectric on the surface of a metallic electrode was used to prevent unwanted chemical reactions such as water electrolysis, however, this approach requires large voltages (10–100 V). Electrowetting between two liquids was also proposed theoretically [365]. A simple approach using renewable graphite surface as a chemically inert interface has recently been introduced, with only small voltages (1–1.5 V) required to induce significant changes in the contact angle (50° and 100° using aqueous/air and aqueous/organic/air configurations, respectively) [255]. Furthermore, it has been shown that the electrowetting is also strongly affected by the surface ageing and the crystallinity of graphene and graphite [366]. Zhang et al. presented electrowetting measurements utilising an SECCM technique and a TEM grid, showing stronger wetting on Cu-bound graphene in comparison to suspended graphene [367].

Wetting and electrowetting phenomena on 2D materials are applicable to a range of technologies from lubrication, microfluidics, to liquid-cell displays. Reverse electrowetting, i.e. alteration of the contact angle accompanied by an accumulation of charge, could be also used for energy harnessing.

6. Conclusions

More than a decade after graphene discovery, the world of 2D materials is reaching its "teenage years", especially in the fast developing condensed matter physics, material science, and nanotechnology research. In contrast, the electrochemistry of graphene and other 2D materials is still in its "infancy". This actually provides electrochemists with a unique opportunity to reap the fundamental knowledge on 2D materials accumulated in other scientific disciplines. At present, the fundamental electrochemical understanding

of 2D materials is overshadowed by a hasty pursuit of their use in energy storage/conversion, catalysis, and sensing. There is no denying of the fact that rapid advances in these applications are invaluable but it should not be done entirely at the expense of the basic scientific understanding, which will, in a long term, lead to much smarter and more efficient ways of harnessing 2D materials' potential. What we need now is to establish the key electrochemical properties such as the electron transfer, capacitance, or tunnelling, and to "brainstorm" on how the unique, tuneable electronic structure of 2D materials can be exploited in electrochemistry. Looking forward, reliable production methods of 2D materials are likely to dominate the transition from the fundamental findings to scalable technologies. While the high-quality crystals produced by ME will continue to be indispensable in fundamental research, CVD and LPE hold great promise for applications. It is evident that overcoming the challenges, which await the future generations of electrochemists, could bring about a new era of tuneable electrochemical devices of 2D materials and their heterostructures with extremely high surface-to-mass ratio and seemingly endless functionalities. It would be unfortunate if electrochemistry remained on the sidelines of the main research activity on 2D materials.

Acknowledgements

M.V. and P.S.T. thank EPSRC (Grants EP/N025938/1 and EP/K016954/1) and EC Horizon 2020 GrapheneCore1 program (Grant 696656) for funding, Julia Velický for obtaining photographs and drawing schematics, and Manchester Nanomaterials Ltd. for the generous donation of layered crystals.

References

[1] K.S. Novoselov, V.I. Fal'ko, L. Colombo, P.R. Gellert, M.G. Schwab, K. Kim, A roadmap for graphene, Nature 490 (2012) 192–200.
[2] S.Z. Butler, S.M. Hollen, L. Cao, Y. Cui, J.A. Gupta, H.R. Gutiérrez, T.F. Heinz, S.S. Hong, J. Huang, A.F. Ismach, E. Johnston-Halperin, M. Kuno, V.V. Plashnitsa, R.D. Robinson, R.S. Ruoff, S. Salahuddin, J. Shan, L. Shi, M.G. Spencer, M. Terrones, W. Windl, J.E. Goldberger, Progress, challenges, and opportunities in two-dimensional materials beyond graphene, ACS Nano 7 (2013) 2898–2926.
[3] H. Tributsch, J.C. Bennett, Electrochemistry and photochemistry of MoS_2 layer crystals. I, J. Electroanal. Chem. 81 (1977) 97–111.
[4] R. Fivaz, E. Mooser, Mobility of charge carriers in semiconducting layer structures, Phys. Rev. 163 (1967) 743–755.
[5] M. Chhowalla, H.S. Shin, G. Eda, L.J. Li, K.P. Loh, H. Zhang, The chemistry of two-dimensional layered transition metal dichalcogenide nanosheets, Nat. Chem. 5 (2013) 263–275.
[6] K.S. Novoselov, A.K. Geim, S.V. Morozov, D. Jiang, Y. Zhang, S.V. Dubonos, I.V. Grigorieva, A.A. Firsov, Electric field in atomically thin carbon films, Science 306 (2004) 666–669.
[7] A.K. Geim, Nobel lecture: random walk to graphene, Rev. Mod. Phys. 83 (2011) 851–862.
[8] J.A. Wilson, A.D. Yoffe, The transition metal dichalcogenides discussion and interpretation of the observed optical, electrical and structural properties, Adv. Phys. 18 (1969) 193–335.
[9] K.S. Novoselov, D. Jiang, F. Schedin, T.J. Booth, V.V. Khotkevich, S.V. Morozov, A.K. Geim, Two-dimensional atomic crystals, Proc. Natl. Acad. Sci. U. S. A. 102 (2005) 10451–10453.
[10] R. Mas-Ballesté, C. Gómez-Navarro, J. Gómez-Herrero, F. Zamora, 2D materials: to graphene and beyond, Nanoscale 3 (2011) 20–30.
[11] M. Osada, T. Sasaki, Two-dimensional dielectric nanosheets: novel nanoelectronics from nanocrystal building blocks, Adv. Mater. 24 (2012) 210–228.
[12] P. Miró, M. Audiffred, T. Heine, An atlas of two-dimensional materials, Chem. Soc. Rev. 43 (2014) 6537–6554.
[13] F. Wang, Z. Wang, Q. Wang, F. Wang, L. Yin, K. Xu, Y. Huang, J. He, Synthesis, properties and applications of 2D non-graphene materials, Nanotechnology 26 (2015) 292001.
[14] A.K. Geim, I.V. Grigorieva, Van der Waals heterostructures, Nature 499 (2013) 419–425.
[15] H. Kim, C.M. Gilmore, A. Piqué, J.S. Horwitz, H. Mattoussi, H. Murata, Z.H. Kafafi, D.B. Chrisey, Electrical, optical, and structural properties of indium–tin–oxide thin films for organic light-emitting devices, J. Appl. Phys. 86 (1999) 6451–6461.
[16] CRC Handbook of Chemistry and Physics, in: W.M. Haynes (Ed.), CRC Press, 2016 http://www.hbcponline.com.
[17] M. Pumera, Z. Sofer, A. Ambrosi, Layered transition metal dichalcogenides for electrochemical energy generation and storage, J. Mater. Chem. A 2 (2014) 8981–8987.
[18] H. Li, Z. Yin, Q. He, H. Li, X. Huang, G. Lu, D.W.H. Fam, A.I.Y. Tok, Q. Zhang, H. Zhang, Fabrication of single- and multilayer MoS_2 film-based field-effect transistors for sensing NO at room temperature, Small 8 (2012) 63–67.
[19] P. Koskinen, I. Fampiou, A. Ramasubramaniam, Density-functional tight-binding simulations of curvature-controlled layer decoupling and band-gap tuning in bilayer MoS_2, Phys. Rev. Lett. 112 (2014) 186802.
[20] H.S. Lee, D.H. Luong, M.S. Kim, Y. Jin, H. Kim, S. Yun, Y.H. Lee, Reconfigurable exciton-plasmon interconversion for nanophotonic circuits, Nat. Commun. 7 (2016) 13663.
[21] K.F. Mak, K. He, J. Shan, T.F. Heinz, Control of valley polarization in monolayer MoS_2 by optical helicity, Nat. Nanotechnol. 7 (2012) 494–498.
[22] K.S. Novoselov, A. Mishchenko, A. Carvalho, A.H. Castro Neto, 2D materials and van der Waals heterostructures, Science 353 (2016) aac9439.
[23] Q.H. Wang, K. Kalantar-Zadeh, A. Kis, J.N. Coleman, M.S. Strano, Electronics and optoelectronics of two-dimensional transition metal dichalcogenides, Nat. Nanotechnol. 7 (2012) 699–712.
[24] L.F. Mattheiss, Band structures of transition-metal-dichalcogenide layer compounds, Phys. Rev. B 8 (1973) 3719–3740.
[25] M. Bernardi, M. Palummo, J.C. Grossman, Extraordinary sunlight absorption and one nanometer thick photovoltaics using two-dimensional monolayer materials, Nano Lett. 13 (2013) 3664–3670.
[26] H.S. Lee, S.-W. Min, Y.-G. Chang, M.K. Park, T. Nam, H. Kim, J.H. Kim, S. Ryu, S. Im, MoS_2 nanosheet phototransistors with thickness-modulated optical energy gap, Nano Lett. 12 (2012) 3695–3700.
[27] F. Withers, O. Del Pozo-Zamudio, A. Mishchenko, A.P. Rooney, A. Gholinia, K. Watanabe, T. Taniguchi, S.J. Haigh, A.K. Geim, A.I. Tartakovskii, K.S. Novoselov, Light-emitting diodes by band-structure engineering in van der Waals heterostructures, Nat. Mater. 14 (2015) 301–306.
[28] X. Chia, A.Y.S. Eng, A. Ambrosi, S.M. Tan, M. Pumera, Electrochemistry of nanostructured layered transition-metal dichalcogenides, Chem. Rev. (Washington, DC, US) 115 (2015) 11941–11966.
[29] B.C. Windom, W.G. Sawyer, D.W. Hahn, A Raman spectroscopic study of MoS_2 and MoO_3: applications to tribological systems, Tribol. Lett. 42 (2011) 301–310.
[30] P.D. Fleischauer, J.R. Lince, P.A. Bertrand, R. Bauer, Electronic structure and lubrication properties of MoS_2: a qualitative molecular orbital approach, Langmuir 5 (1989) 1009–1015.
[31] G. Salomon, A.W.J. De Gee, J.H. Zaat, Mechano-chemical factors in MoS_2-film lubrication, Wear 7 (1964) 87–101.
[32] M. Azhagurajan, T. Kajita, T. Itoh, Y.-G. Kim, K. Itaya, In situ visualization of lithium ion intercalation into MoS_2 single crystals using differential optical microscopy with atomic layer resolution, J. Am. Chem. Soc. 138 (2016) 3355–3361.
[33] B. Radisavljevic, A. Radenovic, J. Brivio, V. Giacometti, A. Kis, Single-layer MoS_2 transistors, Nat. Nanotechnol. 6 (2011) 147–150.
[34] H. Qiu, T. Xu, Z. Wang, W. Ren, H. Nan, Z. Ni, Q. Chen, S. Yuan, F. Miao, F. Song, G. Long, Y. Shi, L. Sun, J. Wang, X. Wang, Hopping transport through defect-induced localized states in molybdenum disulphide, Nat. Commun. 4 (2013) 2642.
[35] A. Das, S. Pisana, B. Chakraborty, S. Piscanec, S.K. Saha, U.V. Waghmare, K.S. Novoselov, H.R. Krishnamurthy, A.K. Geim, A.C. Ferrari, A.K. Sood, Monitoring dopants by Raman scattering in an electrochemically top-gated graphene transistor, Nat. Nanotechnol. 3 (2008) 210–215.
[36] Z. Yin, H. Li, H. Li, L. Jiang, Y. Shi, Y. Sun, G. Lu, Q. Zhang, X. Chen, H. Zhang, Single-layer MoS_2 phototransistors, ACS Nano 6 (2012) 74–80.
[37] X. Zhu, N.R. Monahan, Z. Gong, H. Zhu, K.W. Williams, C.A. Nelson, Charge transfer excitons at van der Waals interfaces, J. Am. Chem. Soc. 137 (2015) 8313–8320.
[38] P. Ajayan, P. Kim, K. Banerjee, Two-dimensional van der Waals materials, Phys. Today 69 (2016) 38–44.
[39] R.A. Bromley, R.B. Murray, A.D. Yoffe, The band structures of some transition metal dichalcogenides. III. Group VIA: trigonal prism materials, J. Phys. C: Solid State Phys. 5 (1972) 759–778.
[40] Y.-C. Lin, D.O. Dumcenco, Y.-S. Huang, K. Suenaga, Atomic mechanism of the semiconducting-to-metallic phase transition in single-layered MoS_2, Nat. Nanotechnol. 9 (2014) 391–396.
[41] R. Kappera, D. Voiry, S.E. Yalcin, B. Branch, G. Gupta, A.D. Mohite, M. Chhowalla, Phase-engineered low-resistance contacts for ultrathin MoS_2 transistors, Nat. Mater. 13 (2014) 1128–1134.
[42] O. Knop, R.D. MacDonald, Chalkogenides of the transition elements: III. Molybdenum ditelluride, Can. J. Chem. 39 (1961) 897–904.
[43] J. Augustin, V. Eyert, T. Böker, W. Frentrup, H. Dwelk, C. Janowitz, R. Manzke, Electronic band structure of the layered compound Td-WTe_2, Phys. Rev. B 62 (2000) 10812–10823.
[44] C.-H. Lee, E.C. Silva, L. Calderin, M.A.T. Nguyen, M.J. Hollander, B. Bersch, T.E. Mallouk, J.A. Robinson, Tungsten ditelluride: a layered semimetal, Sci. Rep. 5 (2015) 10013.
[45] W.G. Dawson, D.W. Bullett, Electronic structure and crystallography of $MoTe_2$ and WTe_2, J. Phys. C: Solid State Phys. 20 (1987) 6159–6174.
[46] B.E. Brown, The crystal structures of WTe_2 and high-temperature $MoTe_2$, Acta Crystallogr. 20 (1966) 268–274.
[47] K.S. Novoselov, Nobel lecture: graphene: materials in the flatland, Rev. Mod. Phys. 83 (2011) 837–849.

[48] K.S. Novoselov, A.K. Geim, S.V. Morozov, D. Jiang, M.I. Katsnelson, I.V. Grigorieva, S.V. Dubonos, A.A. Firsov, Two-dimensional gas of massless Dirac fermions in graphene, Nature 438 (2005) 197–200.
[49] S. Kim, A. Konar, W.S. Hwang, J.H. Lee, J. Lee, J. Yang, C. Jung, H. Kim, J.B. Yoo, J.Y. Choi, Y.W. Jin, S.Y. Lee, D. Jena, W. Choi, K. Kim, High-mobility and low-power thin-film transistors based on multilayer MoS_2 crystals, Nat. Commun. 3 (2012) 1011.
[50] X. Cui, G.-H. Lee, Y.D. Kim, G. Arefe, P.Y. Huang, C.-H. Lee, D.A. Chenet, X. Zhang, L. Wang, F. Ye, F. Pizzocchero, B.S. Jessen, K. Watanabe, T. Taniguchi, D.A. Muller, T. Low, P. Kim, J. Hone, Multi-terminal transport measurements of MoS_2 using a van der Waals heterostructure device platform, Nat. Nano 10 (2015) 534–540.
[51] J. Jeon, S.K. Jang, S.M. Jeon, G. Yoo, Y.H. Jang, J.-H. Park, S. Lee, Layer-controlled CVD growth of large-area two-dimensional MoS_2 films, Nanoscale 7 (2015) 1688–1695.
[52] F. Withers, T.H. Bointon, D.C. Hudson, M.F. Craciun, S. Russo, Electron transport of WS_2 transistors in a hexagonal boron nitride dielectric environment, Sci. Rep. 4 (2014) 4967.
[53] S. Das, H.-Y. Chen, A.V. Penumatcha, J. Appenzeller, High performance multilayer MoS_2 transistors with scandium contacts, Nano Lett. 13 (2013) 100–105.
[54] D. Braga, I. Gutiérrez Lezama, H. Berger, A.F. Morpurgo, Quantitative determination of the band gap of WS_2 with ambipolar ionic liquid-gated transistors, Nano Lett. 12 (2012) 5218–5223.
[55] A. Chernikov, A.M. van der Zande, H.M. Hill, A.F. Rigosi, A. Velauthapillai, J. Hone, T.F. Heinz, Electrical tuning of exciton binding energies in monolayer WS_2, Phys. Rev. Lett. 115 (2015) 126802.
[56] S. Tongay, J. Suh, C. Ataca, W. Fan, A. Luce, J.S. Kang, J. Liu, C. Ko, R. Raghunathanan, J. Zhou, F. Ogletree, J. Li, J.C. Grossman, J. Wu, Defects activated photoluminescence in two-dimensional semiconductors: interplay between bound, charged, and free excitons, Sci. Rep. 3 (2013) 2657.
[57] A. Chernikov, T.C. Berkelbach, H.M. Hill, A. Rigosi, Y. Li, O.B. Aslan, D.R. Reichman, M.S. Hybertsen, T.F. Heinz, Exciton binding energy and nonhydrogenic Rydberg series in monolayer WS_2, Phys. Rev. Lett. 113 (2014) 076802.
[58] K.F. Mak, K. He, C. Lee, G.H. Lee, J. Hone, T.F. Heinz, J. Shan, Tightly bound trions in monolayer MoS_2, Nat. Mater. 12 (2013) 207–211.
[59] Y. You, X.-X. Zhang, T.C. Berkelbach, M.S. Hybertsen, D.R. Reichman, T.F. Heinz, Observation of biexcitons in monolayer WSe_2, Nat. Phys. 11 (2015) 477–481.
[60] K. Kheng, R.T. Cox, M.Y. d' Aubigné, F. Bassani, K. Saminadayar, S. Tatarenko, Observation of negatively charged excitons X^- in semiconductor quantum wells, Phys. Rev. Lett. 71 (1993) 1752–1755.
[61] A.A. High, E.E. Novitskaya, L.V. Butov, M. Hanson, A.C. Gossard, Control of exciton fluxes in an excitonic integrated circuit, Science 321 (2008) 229–231.
[62] W.S. Yun, S.W. Han, S.C. Hong, I.G. Kim, J.D. Lee, Thickness and strain effects on electronic structures of transition metal dichalcogenides: 2H-MX_2 semiconductors (M = Mo, W; X = S, Se, Te), Phys. Rev. B 85 (2012) 033305.
[63] K.F. Mak, C. Lee, J. Hone, J. Shan, T.F. Heinz, Atomically thin MoS_2: a new direct-gap semiconductor, Phys. Rev. Lett. 105 (2010) 136805.
[64] R. Coehoorn, C. Haas, J. Dijkstra, C.J.F. Flipse, R.A. de Groot, A. Wold, Electronic structure of $MoSe_2$, MoS_2, and WSe_2. I. Band-structure calculations and photoelectron spectroscopy, Phys. Rev. B 35 (1987) 6195–6202.
[65] H.J. Lewerenz, A. Heller, F.J. DiSalvo, Relationship between surface morphology and solar conversion efficiency of tungsten diselenide photoanodes, J. Am. Chem. Soc. 102 (1980) 1877–1880.
[66] R. Coehoorn, C. Haas, R.A. de Groot, Electronic structure of $MoSe_2$, MoS_2, and WSe_2. II. The nature of the optical band gaps, Phys. Rev. B 35 (1987) 6203–6206.
[67] E.S. Kadantsev, P. Hawrylak, Electronic structure of a single MoS_2 monolayer, Solid State Commun. 152 (2012) 909–913.
[68] A. Splendiani, L. Sun, Y. Zhang, T. Li, J. Kim, C.-Y. Chim, G. Galli, F. Wang, Emerging photoluminescence in monolayer MoS_2, Nano Lett. 10 (2010) 1271–1275.
[69] P. Tonndorf, R. Schmidt, P. Böttger, X. Zhang, J. Börner, A. Liebig, M. Albrecht, C. Kloc, O. Gordan, D.R.T. Zahn, S.M. De Vasconcellos, R. Bratschitsch, Photoluminescence emission and Raman response of monolayer MoS_2, $MoSe_2$, and WSe_2, Opt. Express 21 (2013) 4908–4916.
[70] D.L. Greenaway, R. Nitsche, Preparation and optical properties of group IV–VI_2 chalcogenides having the CdI_2 structure, J. Phys. Chem. Solids 26 (1965) 1445–1458.
[71] C. Gong, H. Zhang, W. Wang, L. Colombo, R.M. Wallace, K. Cho, Band alignment of two-dimensional transition metal dichalcogenides: application in tunnel field effect transistors, Appl. Phys. Lett. 103 (2013) 053513.
[72] R.F. Frindt, The optical properties of single crystals of WSe_2 and $MoTe_2$, J. Phys. Chem. Solids 24 (1963) 1107–1108.
[73] A.R. Beal, W.Y. Liang, H.P. Hughes, Kramers-Kronig analysis of the reflectivity spectra of 3R-WS_2 and 2H-WSe_2, J. Phys. C: Solid State Phys. 9 (1976) 2449–2457.
[74] A.R. Beal, H.P. Hughes, Kramers-Kronig analysis of the reflectivity spectra of 2H-MoS_2, 2H-$MoSe_2$ and 2H-$MoTe_2$, J. Phys. C: Solid State Phys. 12 (1979) 881–890.
[75] H.Y. Lv, W.J. Lu, D.F. Shao, Y. Liu, S.G. Tan, Y.P. Sun, Perfect charge compensation in WTe_2 for the extraordinary magnetoresistance: from bulk to monolayer, Europhys. Lett. 110 (2015) 37004.
[76] A. Jäger-Waldau, M.C. Lux-Steiner, E. Bucher, MoS_2, $MoSe_2$, WS_2 and WSe_2 thin films for photovoltaics, in: H.P. Strunk, J.H. Werner, B. Fortin, O. Bonnaud (Eds.), Solid State Phenomena, Scitec Publications, Switzerland, 1994, pp. 479–484.
[77] A.R. Beal, H.P. Hughes, W.Y. Liang, The reflectivity spectra of some group VA transition metal dichalcogenides, J. Phys. C: Solid State Phys. 8 (1975) 4236–4248.
[78] R.R. Nair, P. Blake, A.N. Grigorenko, K.S. Novoselov, T.J. Booth, T. Stauber, N.M.R. Peres, A.K. Geim, Fine structure constant defines visual transparency of graphene, Science 320 (2008) 1308.
[79] R.F. Frindt, A.D. Yoffe, Physical properties of layer structures: optical properties and photoconductivity of thin crystals of molybdenum disulphide, Proc. R. Soc. Lond. Ser. A: Math. Phys. Eng. Sci. 273 (1963) 69–83.
[80] S. Bertolazzi, J. Brivio, A. Kis, Stretching and breaking of ultrathin MoS_2, ACS Nano 5 (2011) 9703–9709.
[81] A. Castellanos-Gomez, M. Poot, G.A. Steele, H.S.J. van der Zant, N. Agraït, G. Rubio-Bollinger, Elastic properties of freely suspended MoS_2 nanosheets, Adv. Mater. 24 (2012) 772–775.
[82] P. Mirõ, M. Ghorbani-Asl, T. Heine, Spontaneous ripple formation in MoS_2 monolayers: electronic structure and transport effects, Adv. Mater. 25 (2013) 5473–5475.
[83] S. Luo, G. Hao, Y. Fan, L. Kou, C. He, X. Qi, C. Tang, J. Li, K. Huang, J. Zhong, Formation of ripples in atomically thin MoS_2 and local strain engineering of electrostatic properties, Nanotechnology 26 (2015) 105705.
[84] W. Wu, L. Wang, Y. Li, F. Zhang, L. Lin, S. Niu, D. Chenet, X. Zhang, Y. Hao, T.F. Heinz, J. Hone, Z.L. Wang, Piezoelectricity of single-atomic-layer MoS_2 for energy conversion and piezotronics, Nature 514 (2014) 470–474.
[85] H.S. Khare, D.L. Burris, The effects of environmental water and oxygen on the temperature-dependent friction of sputtered molybdenum disulfide, Tribol. Lett. 52 (2013) 485–493.
[86] Y. Kim, Y.I. Jhon, J. Park, J.H. Kim, S. Lee, Y.M. Jhon, Anomalous Raman scattering and lattice dynamics in mono- and few-layer WTe_2, Nanoscale 8 (2016) 2309–2316.
[87] M. Velický, M.A. Bissett, P.S. Toth, H.V. Patten, S.D. Worrall, A.N.J. Rodgers, E.W. Hill, I.A. Kinloch, K.S. Novoselov, T. Georgiou, L. Britnell, R.A.W. Dryfe, Electron transfer kinetics on natural crystals of MoS_2 and graphite, Phys. Chem. Chem. Phys. 17 (2015) 17844–17853.
[88] B.A. Parkinson, T.E. Furtak, D. Canfield, K. Kam, G. Kline, Evaluation and reduction of efficiency losses at tungsten diselenide photoanodes, Faraday Discuss. Chem. Soc. 70 (1980) 233–245.
[89] M. Velický, D.F. Bradley, A.J. Cooper, E.W. Hill, I.A. Kinloch, A. Mishchenko, K.S. Novoselov, H.V. Patten, P.S. Toth, A.T. Valota, S.D. Worrall, R.A.W. Dryfe, Electron transfer kinetics on mono- and multilayer graphene, ACS Nano 8 (2014) 10089–10100.
[90] R.F. Frindt, Optical absorption of a few unit-cell layers of MoS_2, Phys. Rev. 140 (1965) A536–A539.
[91] R.F. Frindt, Single crystals of MoS_2 several molecular layers thick, J. Appl. Phys. 37 (1966) 1928–1929.
[92] Y. Huang, E. Sutter, N.N. Shi, J. Zheng, T. Yang, D. Englund, H.-J. Gao, P. Sutter, Reliable exfoliation of large-area high-quality flakes of graphene and other two-dimensional materials, ACS Nano 9 (2015) 10612–10620.
[93] F. Bonaccorso, A. Lombardo, T. Hasan, Z. Sun, L. Colombo, A.C. Ferrari, Production and processing of graphene and 2D crystals, Mater. Today 15 (2012) 564–589.
[94] J.N. Coleman, M. Lotya, A. O'Neill, S.D. Bergin, P.J. King, U. Khan, K. Young, A. Gaucher, S. De, R.J. Smith, I.V. Shvets, S.K. Arora, G. Stanton, H.Y. Kim, K. Lee, G.T. Kim, G.S. Duesberg, T. Hallam, J.J. Boland, J.J. Wang, J.F. Donegan, J.C. Grunlan, G. Moriarty, A. Shmeliov, R.J. Nicholls, J.M. Perkins, E.M. Grieveson, K. Theuwissen, D.W. McComb, P.D. Nellist, V. Nicolosi, Two-dimensional nanosheets produced by liquid exfoliation of layered materials, Science 331 (2011) 568–571.
[95] Y. Hernandez, V. Nicolosi, M. Lotya, F.M. Blighe, Z. Sun, S. De, I.T. McGovern, B. Holland, M. Byrne, Y.K. Gun'ko, J.J. Boland, P. Niraj, G. Duesberg, S. Krishnamurthy, R. Goodhue, J. Hutchison, V. Scardaci, A.C. Ferrari, J.N. Coleman, High-yield production of graphene by liquid-phase exfoliation of graphite, Nat. Nanotechnol. 3 (2008) 563–568.
[96] A. Harvey, C. Backes, Z. Gholamvand, D. Hanlon, D. McAteer, H.C. Nerl, E. McGuire, A. Seral-Ascaso, Q.M. Ramasse, N. McEvoy, S. Winters, N.C. Berner, D. McCloskey, J.F. Donegan, G.S. Duesberg, V. Nicolosi, J.N. Coleman, Preparation of gallium sulfide nanosheets by liquid exfoliation and their application as hydrogen evolution catalysts, Chem. Mater. 27 (2015) 3483–3493.
[97] M.A. Bissett, S.D. Worrall, I.A. Kinloch, R.A.W. Dryfe, Comparison of two-dimensional transition metal dichalcogenides for electrochemical supercapacitors, Electrochim. Acta 201 (2016) 30–37.
[98] M. Velický, P.S. Toth, A.M. Rakowski, A.P. Rooney, A. Kozikov, C.R. Woods, A. Mishchenko, L. Fumagalli, J. Yin, V. Zólyomi, T. Georgiou, S.J. Haigh, K.S. Novoselov, R.A.W. Dryfe, Exfoliation of natural van der Waals heterostructures to a single unit cell thickness, Nat. Commun. 8 (2017) 14410.
[99] Z. Guo, H. Zhang, S. Lu, Z. Wang, S. Tang, J. Shao, Z. Sun, H. Xie, H. Wang, X.-F. Yu, P.K. Chu, From black phosphorus to phosphorene: basic solvent exfoliation, evolution of Raman scattering, and applications to ultrafast photonics, Adv. Funct. Mater. 25 (2015) 6996–7002.
[100] A.H. Woomer, T.W. Farnsworth, J. Hu, R.A. Wells, C.L. Donley, S.C. Warren, Phosphorene: synthesis, scale-up, and quantitative optical spectroscopy, ACS Nano 9 (2015) 8869–8884.

[101] Y. Santiago, C.R. Cabrera, Surface analysis and electrochemistry of MoS_2 thin films prepared by intercalation-exfoliation techniques, J. Electrochem. Soc. 141 (1994) 629–635.
[102] P. Joensen, R.F. Frindt, S.R. Morrison, Single-layer MoS_2, Mater. Res. Bull. 21 (1986) 457–461.
[103] C.C. Mayorga-Martinez, A. Ambrosi, A.Y.S. Eng, Z. Sofer, M. Pumera, Transition metal dichalcogenides (MoS_2, $MoSe_2$, WS_2 and WSe_2) exfoliation technique has strong influence upon their capacitance, Electrochem. Commun. 56 (2015) 24–28.
[104] J. Zheng, H. Zhang, S. Dong, Y. Liu, C. Tai Nai, H. Suk Shin, H. Young Jeong, B. Liu, K. Ping Loh, High yield exfoliation of two-dimensional chalcogenides using sodium naphthalenide, Nat. Commun. 5 (2014) 2995.
[105] A.J. Cooper, M. Velický, I.A. Kinloch, R.A.W. Dryfe, On the controlled electrochemical preparation of R_4N^+ graphite intercalation compounds and their host structural deformation effects, J. Electroanal. Chem. 730 (2014) 34–40.
[106] A.J. Cooper, N.R. Wilson, I.A. Kinloch, R.A.W. Dryfe, Single stage electrochemical exfoliation method for the production of few-layer graphene via intercalation of tetraalkylammonium cations, Carbon 66 (2014) 340–350.
[107] Z. Zeng, Z. Yin, X. Huang, H. Li, Q. He, G. Lu, F. Boey, H. Zhang, Single-layer semiconducting nanosheets: high-yield preparation and device fabrication, Angew. Chem. Int. Ed. 50 (2011) 11093–11097.
[108] N. Liu, P. Kim, J.H. Kim, J.H. Ye, S. Kim, C.J. Lee, Large-area atomically thin MoS_2 nanosheets prepared using electrochemical exfoliation, ACS Nano 8 (2014) 6902–6910.
[109] A. Ambrosi, Z. Sofer, J. Luxa, M. Pumera, Exfoliation of Layered Topological Insulators Bi_2Se_3 and Bi_2Te_3 via Electrochemistry, ACS Nano 10 (2016) 11442–11448.
[110] F. Bonaccorso, A. Bartolotta, J.N. Coleman, C. Backes, 2D-crystal-based functional inks, Adv. Mater. 28 (2016) 6136–6166.
[111] M.A. Bissett, I.A. Kinloch, R.A.W. Dryfe, Characterization of MoS_2-graphene composites for high-performance coin cell supercapacitors, ACS Appl. Mater. Interfaces 7 (2015) 17388–17398.
[112] S. Wu, Z. Zeng, Q. He, Z. Wang, S.J. Wang, Y. Du, Z. Yin, X. Sun, W. Chen, H. Zhang, Electrochemically reduced single-layer MoS_2 nanosheets: characterization, properties, and sensing applications, Small 8 (2012) 2264–2270.
[113] S. Wang, Y. Rong, Y. Fan, M. Pacios, H. Bhaskaran, K. He, J.H. Warner, Shape evolution of monolayer MoS_2 crystals grown by chemical vapor deposition, Chem. Mater. 26 (2014) 6371–6379.
[114] H. Li, X. Duan, X. Wu, X. Zhuang, H. Zhou, Q. Zhang, X. Zhu, W. Hu, P. Ren, P. Guo, L. Ma, X. Fan, X. Wang, J. Xu, A. Pan, X. Duan, Growth of alloy $MoS_{2x}Se_{2(1-x)}$ nanosheets with fully tunable chemical compositions and optical properties, J. Am. Chem. Soc. 136 (2014) 3756–3759.
[115] A.M. Van Der Zande, P.Y. Huang, D.A. Chenet, T.C. Berkelbach, Y. You, G.H. Lee, T.F. Heinz, D.R. Reichman, D.A. Muller, J.C. Hone, Grains and grain boundaries in highly crystalline monolayer molybdenum disulphide, Nat. Mater. 12 (2013) 554–561.
[116] Y.-H. Lee, X.-Q. Zhang, W. Zhang, M.-T. Chang, C.-T. Lin, K.-D. Chang, Y.-C. Yu, J.T.-W. Wang, C.-S. Chang, L.-J. Li, T.-W. Lin, Synthesis of large-area MoS_2 atomic layers with chemical vapor deposition, Adv. Mater. 24 (2012) 2320–2325.
[117] X. Wang, Y. Gong, G. Shi, W.L. Chow, K. Keyshar, G. Ye, R. Vajtai, J. Lou, Z. Liu, E. Ringe, B.K. Tay, P.M. Ajayan, Chemical vapor deposition growth of crystalline monolayer $MoSe_2$, ACS Nano 8 (2014) 5125–5131.
[118] H.R. Gutiérrez, N. Perea-López, A.L. Elías, A. Berkdemir, B. Wang, R. Lv, F. López-Urías, V.H. Crespi, H. Terrones, M. Terrones, Extraordinary room-temperature photoluminescence in triangular WS_2 monolayers, Nano Lett. 13 (2013) 3447–3454.
[119] P.K. Chow, E. Singh, B.C. Viana, J. Gao, J. Luo, J. Li, Z. Lin, A.L. Elías, Y. Shi, Z. Wang, M. Terrones, N. Koratkar, Wetting of mono and few-layered WS_2 and MoS_2 films supported on Si/SiO_2 substrates, ACS Nano 9 (2015) 3023–3031.
[120] S. Najmaei, Z. Liu, W. Zhou, X. Zou, G. Shi, S. Lei, B.I. Yakobson, J.-C. Idrobo, P.M. Ajayan, J. Lou, Vapour phase growth and grain boundary structure of molybdenum disulphide atomic layers, Nat. Mater. 12 (2013) 754–759.
[121] X.-Q. Zhang, C.-H. Lin, Y.-W. Tseng, K.-H. Huang, Y.-H. Lee, Synthesis of lateral heterostructures of semiconducting atomic layers, Nano Lett. 15 (2015) 410–415.
[122] G. Eres, M. Regmi, C.M. Rouleau, J. Chen, I.N. Ivanov, A.A. Puretzky, D.B. Geohegan, Cooperative island growth of large-area single-crystal graphene on copper using chemical vapor deposition, ACS Nano 8 (2014) 5657–5669.
[123] A.P.S. Gaur, S. Sahoo, M. Ahmadi, M.J.F. Guinel, S.K. Gupta, R. Pandey, S.K. Dey, R.S. Katiyar, Optical and vibrational studies of partially edge-terminated vertically aligned nanocrystalline MoS_2 thin films, J. Phys. Chem. C 117 (2013) 26262–26268.
[124] D. Kong, H. Wang, J.J. Cha, M. Pasta, K.J. Koski, J. Yao, Y. Cui, Synthesis of MoS_2 and $MoSe_2$ films with vertically aligned layers, Nano Lett. 13 (2013) 1341–1347.
[125] L.H. Brixner, Preparation and properties of the single crystalline AB2-type selenides and tellurides of niobium, tantalum, molybdenum and tungsten, J. Inorg. Nucl. Chem. 24 (1962) 257–263.
[126] G. Kline, K. Kam, D. Canfield, B.A. Parkinson, Efficient and stable photoelectrochemical cells constructed with WSe_2 and $MoSe_2$ photoanodes, Sol. Energy Mater. 4 (1981) 301–308.
[127] N. Balakrishnan, Z.R. Kudrynskyi, M.W. Fay, G.W. Mudd, S.A. Svatek, O. Makarovsky, Z.D. Kovalyuk, L. Eaves, P.H. Beton, A. Patanè, Room temperature electroluminescence from mechanically formed van der Waals III–VI homojunctions and heterojunctions, Adv. Opt. Mater. 2 (2014) 1064–1069.
[128] G.W. Mudd, S.A. Svatek, T. Ren, A. Patanè, O. Makarovsky, L. Eaves, P.H. Beton, Z.D. Kovalyuk, G.V. Lashkarev, Z.R. Kudrynskyi, A.I. Dmitriev, Tuning the bandgap of exfoliated InSe nanosheets by quantum confinement, Adv. Mater. 25 (2013) 5714–5718.
[129] W. Yang, G. Chen, Z. Shi, C.-C. Liu, L. Zhang, G. Xie, M. Cheng, D. Wang, R. Yang, D. Shi, K. Watanabe, T. Taniguchi, Y. Yao, Y. Zhang, G. Zhang, Epitaxial growth of single-domain graphene on hexagonal boron nitride, Nat. Mater. 12 (2013) 792–797.
[130] L. Zhi-Long, W. Mei-Xiao, X. Jin-Peng, G. Jian-Feng, L. Guy Le, V. Patrick, Q. Dong, G. Chun-Lei, L. Canhua, J. Jin-Feng, Various atomic structures of monolayer silicene fabricated on Ag(111), New J. Phys. 16 (2014) 075006.
[131] M.E. Dávila, L. Xian, S. Cahangirov, A. Rubio, G. Le Lay, Germanene: a novel two-dimensional germanium allotrope akin to graphene and silicene, New J. Phys. 16 (2014) 095002.
[132] F.-F. Zhu, W.-J. Chen, Y. Xu, C.-L. Gao, D.-D. Guan, C.-H. Liu, D. Qian, S.-C. Zhang, J.-F. Jia, Epitaxial growth of two-dimensional stanene, Nat. Mater. 14 (2015) 1020–1025.
[133] A.M. Stacy, D.T. Hodul, Raman spectra of IVB and VIB transition metal disulfides using laser energies near the absorption edges, J. Phys. Chem. Solids 46 (1985) 405–409.
[134] D.H. Keum, S. Cho, J.H. Kim, D.-H. Choe, H.-J. Sung, M. Kan, H. Kang, J.-Y. Hwang, S.W. Kim, H. Yang, K.J. Chang, Y.H. Lee, Bandgap opening in few-layered monoclinic $MoTe_2$, Nat. Phys. 11 (2015) 482–486.
[135] K.S. Novoselov, A.H. Castro Neto, Two-dimensional crystals-based heterostructures: materials with tailored properties, Phys. Scr. 2012 (2012) 014006.
[136] H. Fang, C. Battaglia, C. Carraro, S. Nemsak, B. Ozdol, J.S. Kang, H.A. Bechtel, S.B. Desai, F. Kronast, A.A. Unal, G. Conti, C. Conlon, G.K. Palsson, M.C. Martin, A.M. Minor, C.S. Fadley, E. Yablonovitch, R. Maboudian, A. Javey, Strong interlayer coupling in van der Waals heterostructures built from single-layer chalcogenides, Proc. Natl. Acad. Sci. U. S. A. 111 (2014) 6198–6202.
[137] L. Wang, I. Meric, P.Y. Huang, Q. Gao, Y. Gao, H. Tran, T. Taniguchi, K. Watanabe, L.M. Campos, D.A. Muller, J. Guo, P. Kim, J. Hone, K.L. Shepard, C.R. Dean, One-dimensional electrical contact to a two-dimensional material, Science 342 (2013) 614–617.
[138] L. Britnell, R.M. Ribeiro, A. Eckmann, R. Jalil, B.D. Belle, A. Mishchenko, Y.-J. Kim, R.V. Gorbachev, T. Georgiou, S.V. Morozov, A.N. Grigorenko, A.K. Geim, C. Casiraghi, A.H.C. Neto, K.S. Novoselov, Strong light-matter interactions in heterostructures of atomically thin films, Science 340 (2013) 1311–1314.
[139] S.J. Haigh, A. Gholinia, R. Jalil, S. Romani, L. Britnell, D.C. Elias, K.S. Novoselov, L.A. Ponomarenko, A.K. Geim, R. Gorbachev, Cross-sectional imaging of individual layers and buried interfaces of graphene-based heterostructures and superlattices, Nat. Mater. 11 (2012) 764–767.
[140] P. Blake, E.W. Hill, A.H. Castro Neto, K.S. Novoselov, D. Jiang, R. Yang, T.J. Booth, A.K. Geim, Making graphene visible, Appl. Phys. Lett. 91 (2007) 063124.
[141] A. Castellanos-Gomez, N. Agraït, G. Rubio-Bollinger, Optical identification of atomically thin dichalcogenide crystals, Appl. Phys. Lett. 96 (2010) 213116.
[142] M.M. Benameur, B. Radisavljevic, J.S. Héron, S. Sahoo, H. Berger, A. Kis, Visibility of dichalcogenide nanolayers, Nanotechnology 22 (2011).
[143] C. Lee, H. Yan, L.E. Brus, T.F. Heinz, J. Hone, S. Ryu, Anomalous lattice vibrations of single- and few-layer MoS_2, ACS Nano 4 (2010) 2695–2700.
[144] H. Liu, A.T. Neal, Z. Zhu, Z. Luo, X. Xu, D. Tománek, P.D. Ye, Phosphorene: an unexplored 2D semiconductor with a high hole mobility, ACS Nano 8 (2014) 4033–4041.
[145] B.J. Robinson, C.E. Giusca, Y.T. Gonzalez, N.D. Kay, O. Kazakova, O.V. Kolosov, Structural, optical and electrostatic properties of single and few-layers MoS_2: effect of substrate, 2D Mater. 2 (2015) 015005.
[146] M. Velický, M.A. Bissett, C.R. Woods, P.S. Toth, T. Georgiou, I.A. Kinloch, K.S. Novoselov, R.A.W. Dryfe, Photoelectrochemistry of pristine mono- and few-layer MoS_2, Nano Lett. 16 (2016) 2023–2032.
[147] H. Li, Q. Zhang, C.C.R. Yap, B.K. Tay, T.H.T. Edwin, A. Olivier, D. Baillargeat, From bulk to monolayer MoS_2: evolution of Raman scattering, Adv. Funct. Mater. 22 (2012) 1385–1390.
[148] S. Tongay, J. Zhou, C. Ataca, K. Lo, T.S. Matthews, J. Li, J.C. Grossman, J. Wu, Thermally driven crossover from indirect toward direct bandgap in 2D semiconductors: $MoSe_2$ versus MoS_2, Nano Lett. 12 (2012) 5576–5580.
[149] N.D. Kay, B.J. Robinson, V.I. Fal'Ko, K.S. Novoselov, O.V. Kolosov, Electromechanical sensing of substrate charge hidden under atomic 2D crystals, Nano Lett. 14 (2014) 3400–3404.
[150] D. Sercombe, S. Schwarz, O.D. Pozo-Zamudio, F. Liu, B.J. Robinson, E.A. Chekhovich, I.I. Tartakovskii, O. Kolosov, A.I. Tartakovskii, Optical investigation of the natural electron doping in thin MoS_2 films deposited on dielectric substrates, Sci. Rep. 3 (2013) 3489.
[151] C.P. Lu, G. Li, J. Mao, L.M. Wang, E.Y. Andrei, Bandgap, mid-gap states, and gating effects in MoS_2, Nano Lett. 14 (2014) 4628–4633.
[152] M.S. Dresselhaus, A. Jorio, M. Hofmann, G. Dresselhaus, R. Saito, Perspectives on carbon nanotubes and graphene Raman spectroscopy, Nano Lett. 10 (2010) 751–758.

[153] A.C. Ferrari, J.C. Meyer, V. Scardaci, C. Casiraghi, M. Lazzeri, F. Mauri, S. Piscanec, D. Jiang, K.S. Novoselov, S. Roth, A.K. Geim, Raman spectrum of graphene and graphene layers, Phys. Rev. Lett. 97 (2006) 187401.
[154] T.J. Wieting, J.L. Verble, Infrared and Raman studies of long-wavelength optical phonons in hexagonal MoS_2, Phys. Rev. B 3 (1971) 4286–4292.
[155] A. Berkdemir, H.R. Gutiérrez, A.R. Botello-Méndez, N. Perea-López, A.L. Elías, C.I. Chia, B. Wang, V.H. Crespi, F. López-Urías, J.C. Charlier, H. Terrones, M. Terrones, Identification of individual and few layers of WS_2 using Raman spectroscopy, Sci. Rep. 3 (2013) 1755.
[156] M. Yamamoto, S.T. Wang, M. Ni, Y.-F. Lin, S.-L. Li, S. Aikawa, W.-B. Jian, K. Ueno, K. Wakabayashi, K. Tsukagoshi, Strong enhancement of Raman scattering from a bulk-inactive vibrational mode in few-layer $MoTe_2$, ACS Nano 8 (2014) 3895–3903.
[157] W. Zhao, Z. Ghorannevis, K.K. Amara, J.R. Pang, M. Toh, X. Zhang, C. Kloc, P.H. Tan, G. Eda, Lattice dynamics in mono- and few-layer sheets of WS_2 and WSe_2, Nanoscale 5 (2013) 9677–9683.
[158] X. Lu, M.I.B. Utama, J. Lin, X. Luo, Y. Zhao, J. Zhang, S.T. Pantelides, W. Zhou, S.Y. Quek, Q. Xiong, Rapid and nondestructive identification of polytypism and stacking sequences in few-layer molybdenum diselenide by Raman spectroscopy, Adv. Mater. 27 (2015) 4502–4508.
[159] Y.C. Jiang, J. Gao, L. Wang, Raman fingerprint for semi-metal WTe_2 evolving from bulk to monolayer, Sci. Rep. 6 (2016) 19624.
[160] B. Chakraborty, H.S.S.R. Matte, A.K. Sood, C.N.R. Rao, Layer-dependent resonant Raman scattering of a few layer MoS_2, J. Raman Spectrosc. 44 (2013) 92–96.
[161] Y. Zhao, J. Qiao, P. Yu, Z. Hu, Z. Lin, S.P. Lau, Z. Liu, W. Ji, Y. Chai, Extraordinarily strong interlayer interaction in 2D layered PtS_2, Adv. Mater. 28 (2016) 2399–2407.
[162] T. Kanazawa, T. Amemiya, A. Ishikawa, V. Upadhyaya, K. Tsuruta, T. Tanaka, Y. Miyamoto, Few-layer HfS_2 transistors, Sci. Rep. 6 (2016) 22277.
[163] S. Tongay, H. Sahin, C. Ko, A. Luce, W. Fan, K. Liu, J. Zhou, Y.-S. Huang, C.-H. Ho, J. Yan, D.F. Ogletree, S. Aloni, J. Ji, S. Li, J. Li, F.M. Peeters, J. Wu, Monolayer behaviour in bulk ReS_2 due to electronic and vibrational decoupling, Nat. Commun. 5 (2014) 3252.
[164] Y. Huang, E. Sutter, J.T. Sadowski, M. Cotlet, O.L.A. Monti, D.A. Racke, M.R. Neupane, D. Wickramaratne, R.K. Lake, B.A. Parkinson, P. Sutter, Tin disulfide – an emerging layered metal dichalcogenide semiconductor: materials properties and device characteristics, ACS Nano 8 (2014) 10743–10755.
[165] W. Zhao, Z. Ghorannevis, L. Chu, M. Toh, C. Kloc, P.-H. Tan, G. Eda, Evolution of electronic structure in atomically thin sheets of WS_2 and WSe_2, ACS Nano 7 (2013) 791–797.
[166] H. Nan, Z. Wang, W. Wang, Z. Liang, Y. Lu, Q. Chen, D. He, P. Tan, F. Miao, X. Wang, J. Wang, Z. Ni, Strong photoluminescence enhancement of MoS_2 through defect engineering and oxygen bonding, ACS Nano 8 (2014) 5738–5745.
[167] N. Mao, Y. Chen, D. Liu, J. Zhang, L. Xie, Solvatochromic effect on the photoluminescence of MoS_2 monolayers, Small 9 (2013) 1312–1315.
[168] Y.Y. Hui, X. Liu, W. Jie, N.Y. Chan, J. Hao, Y.-T. Hsu, L.-J. Li, W. Guo, S.P. Lau, Exceptional tunability of band energy in a compressively strained trilayer MoS_2 sheet, ACS Nano 7 (2013) 7126–7131.
[169] C. Rice, R.J. Young, R. Zan, U. Bangert, D. Wolverson, T. Georgiou, R. Jalil, K.S. Novoselov, Raman-scattering measurements and first-principles calculations of strain-induced phonon shifts in monolayer MoS_2, Phys. Rev. B 87 (2013) 081307.
[170] M.A. Bissett, M. Tsuji, H. Ago, Strain engineering the properties of graphene and other two-dimensional crystals, Phys. Chem. Chem. Phys. 16 (2014) 11124–11138.
[171] M. Peña-Álvarez, E. del Corro, Á. Morales-García, L. Kavan, M. Kalbac, O. Frank, Single layer molybdenum disulfide under direct out-of-plane compression: low-stress band-gap engineering, Nano Lett. 15 (2015) 3139–3146.
[172] M. Buscema, G.A. Steele, H.S.J. van der Zant, A. Castellanos-Gomez, The effect of the substrate on the Raman and photoluminescence emission of single-layer MoS_2, Nano Res. 7 (2014) 1–11.
[173] S.M. Tan, A. Ambrosi, Z. Sofer, Š. Huber, D. Sedmidubský, M. Pumera, Pristine basal- and edge-plane-oriented molybdenite MoS_2 exhibiting highly anisotropic properties, Chem. Eur. J. 21 (2015) 7170–7178.
[174] S. Mignuzzi, A.J. Pollard, N. Bonini, B. Brennan, I.S. Gilmore, M.A. Pimenta, D. Richards, D. Roy, Effect of disorder on Raman scattering of single-layer MoS_2, Phys. Rev. B 91 (2015) 195411.
[175] J.M. Soon, K.P. Loh, Electrochemical double-layer capacitance of MoS_2 nanowall films, Electrochem. Solid-State Lett. 10 (2007) 250–254.
[176] W. Zhou, X. Zou, S. Najmaei, Z. Liu, Y. Shi, J. Kong, J. Lou, P.M. Ajayan, B.I. Yakobson, J.-C. Idrobo, Intrinsic structural defects in monolayer molybdenum disulfide, Nano Lett. 13 (2013) 2615–2622.
[177] F. Pedraza, J. Cruz-Reyes, D. Acosta, M.J. Yanez, M. Avalos-Borja, S. Fuentes, The structure characterization of MoS_2 and WS_2 catalysts by HREM, J. Phys. Condens. Matter 5 (1993) A219–A220.
[178] H.I. Rasool, C. Ophus, A. Zettl, Atomic defects in two dimensional materials, Adv. Mater. 27 (2015) 5771–5777.
[179] Z. Yu, Y. Pan, Y. Shen, Z. Wang, Z.-Y. Ong, T. Xu, R. Xin, L. Pan, B. Wang, L. Sun, J. Wang, G. Zhang, Y.W. Zhang, Y. Shi, X. Wang, Towards intrinsic charge transport in monolayer molybdenum disulfide by defect and interface engineering, Nat. Commun. 5 (2014) 5290.
[180] R.R. Chianelli, A.F. Ruppert, S.K. Behal, B.H. Kear, A. Wold, R. Kershaw, The reactivity of MoS_2 single crystal edge planes, J. Catal. 92 (1985) 56–63.
[181] C. Huang, S. Wu, A.M. Sanchez, J.J.P. Peters, R. Beanland, J.S. Ross, P. Rivera, W. Yao, D.H. Cobden, X. Xu, Lateral heterojunctions within monolayer $MoSe_2$–WSe_2 semiconductors, Nat. Mater. 13 (2014) 1096–1101.
[182] L. Benoist, D. Gonbeau, G. Pfister-Guillouzo, E. Schmidt, G. Meunier, A. Levasseur, X-ray photoelectron spectroscopy characterization of amorphous molybdenum oxysulfide thin films, Thin Solid Films 258 (1995) 110–114.
[183] N.M.D. Brown, N. Cui, A. McKinley, An XPS study of the surface modification of natural MoS_2 following treatment in an RF-oxygen plasma, Appl. Surf. Sci. 134 (1998) 11–21.
[184] T.J. Whittles, L.A. Burton, J.M. Skelton, A. Walsh, T.D. Veal, V.R. Dhanak, Band alignments, valence bands, and core levels in the tin sulfides Sn_S, SnS_2, and Sn_2S_3: experiment and theory, Chem. Mater. 28 (2016) 3718–3726.
[185] S. McDonnell, R. Addou, C. Buie, R.M. Wallace, C.L. Hinkle, Defect-dominated doping and contact resistance in MoS_2, ACS Nano 8 (2014) 2880–2888.
[186] A. Winchester, S. Ghosh, S. Feng, A.L. Elias, T. Mallouk, M. Terrones, S. Talapatra, Electrochemical characterization of liquid phase exfoliated two-dimensional layers of molybdenum disulfide, ACS Appl. Mater. Interfaces 6 (2014) 2125–2130.
[187] S. Walia, S. Balendhran, Y. Wang, R. Ab Kadir, A. Sabirin Zoolfakar, P. Atkin, J. Zhen Ou, S. Sriram, K. Kalantar-zadeh, M. Bhaskaran, Characterization of metal contacts for two-dimensional MoS_2 nanoflakes, Appl. Phys. Lett. 103 (2013) 232105.
[188] A. Kozbial, X. Gong, H. Liu, L. Li, Understanding the intrinsic water wettability of molybdenum disulfide (MoS_2), Langmuir 31 (2015) 8429–8435.
[189] Z. Li, Y. Wang, A. Kozbial, G. Shenoy, F. Zhou, R. McGinley, P. Ireland, B. Morganstein, A. Kunkel, S.P. Surwade, L. Li, H. Liu, Effect of airborne contaminants on the wettability of supported graphene and graphite, Nat. Mater. 12 (2013) 925–931.
[190] M. Ghorbani-Asl, S. Borini, A. Kuc, T. Heine, Strain-dependent modulation of conductivity in single-layer transition-metal dichalcogenides, Phys. Rev. B 87 (2013) 235434.
[191] N. Zibouche, P. Philipsen, T. Heine, A. Kuc, Electron transport in MoWSeS monolayers in the presence of an external electric field, Phys. Chem. Chem. Phys. 16 (2014) 11251–11255.
[192] D. Parobek, H. Liu, Wettability of graphene, 2D Mater. 2 (2015) 032001.
[193] J. Rafiee, X. Mi, H. Gullapalli, A.V. Thomas, F. Yavari, Y. Shi, P.M. Ajayan, N.A. Koratkar, Wetting transparency of graphene, Nat. Mater. 11 (2012) 217–222.
[194] C.J. Shih, M.S. Strano, D. Blankschtein, Wetting translucency of graphene, Nat. Mater. 12 (2013) 866–869.
[195] R. Raj, S.C. Maroo, E.N. Wang, Wettability of graphene, Nano Lett. 13 (2013) 1509–1515.
[196] R.L. McCreery, Advanced carbon electrode materials for molecular electrochemistry, Chem. Rev. (Washington, DC, US) 108 (2008) 2646–2687.
[197] S. Trasatti, The absolute electrode potential: an explanatory note (Recommendations 1986), J. Electroanal. Chem. Interfacial Electrochem. 209 (1986) 417–428.
[198] A.J. Bard, L.R. Faulkner, Electrochemical Methods. Fundamentals and Applications, 2nd ed., John Wiley & Sons, Inc., New York, 2001.
[199] S.M. Ahmed, H. Gerischer, Influence of crystal surface orientation on redox reactions at semiconducting MoS_2, Electrochim. Acta 24 (1979) 705–711.
[200] A. Fujishima, Y. Noguchi, K. Honda, B.H. Loo, Photoelectrochemical studies of MoS_2 electrode by rotating ring-disk electrode technique, Bull. Chem. Soc. Jpn. 55 (1982) 17–22.
[201] S.M. Ahmed, Surface and photoelectrochemical studies of semiconducting MoS_2, Electrochim. Acta 27 (1982) 707–712.
[202] A.W. Bott, Electrochemistry of semiconductors, Curr. Sep. 17 (1998) 87–92.
[203] R. Krishnan, Fundamentals of Semiconductor Electrochemistry and Photoelectrochemistry, Encyclopedia of Electrochemistry, Wiley-VCH Verlag GmbH & Co. KGaA, 2007.
[204] W. Kautek, H. Gerischer, H. Tributsch, The role of carrier diffusion and indirect optical transitions in the photoelectrochemical behavior of layer type d-band semiconductors, J. Electrochem. Soc. 127 (1980) 2471–2478.
[205] Y. Xu, M.A.A. Schoonen, The absolute energy positions of conduction and valence bands of selected semiconducting minerals, Am. Mineral. 85 (2000) 543–556.
[206] E. Kecsenovity, B. Endrődi, P.S. Tóth, Y. Zou, R.A.W. Dryfe, K. Rajeshwar, C. Janáky, Enhanced photoelectrochemical performance of cuprous oxide/graphene nanohybrids, J. Am. Chem. Soc. (2017), http://dx.doi.org/10.1021/jacs.1027b01820.
[207] S.N. Frank, A.J. Bard, Semiconductor electrodes. II. Electrochemistry at n-type TiO_2 electrodes in acetonitrile solutions, J. Am. Chem. Soc. 97 (1975) 7427–7433.
[208] H.D. Abruña, G.A. Hope, A.J. Bard, Semiconductor electrodes: XLV. Photoelectrochemistry of n- and p-type $MoTe_2$ formula in aqueous solutions, J. Electrochem. Soc. 129 (1982) 2224–2228.
[209] H. Gerischer, Electrolytic decomposition and photodecomposition of compound semiconductors in contact with electrolytes, J. Vac. Sci. Technol. 15 (1978) 1422–1428.
[210] W. Kautek, H. Gerischer, Anisotropic photocorrosion of n-type MoS_2 $MoSe_2$, and WSe_2 single crystal surfaces: the role of cleavage steps, line and screw dislocations, Surf. Sci. 119 (1982) 46–60.
[211] J.R. Miller, L.T. Calcaterra, G.L. Closs, Intramolecular long-distance electron transfer in radical anions. The effects of free energy and solvent on the reaction rates, J. Am. Chem. Soc. 106 (1984) 3047–3049.
[212] G.L. Closs, L.T. Calcaterra, N.J. Green, K.W. Penfield, J.R. Miller, Distance, stereoelectronic effects, and the Marcus inverted region in intramolecular

electron transfer in organic radical anions, J. Phys. Chem. 90 (1986) 3673–3683.
[213] H. Tributsch, O. Gorochov, Photoelectrochemical reaction behaviour of platinum disulphide with water and reducing agents, Electrochim. Acta 27 (1982) 215–221.
[214] H.D. Abruña, A.J. Bard, Semiconductor electrodes. 44. Photoelectrochemistry at polycrystalline p-Type WSe_2 films, J. Electrochem. Soc. 129 (1982) 673–675.
[215] F.R.F. Fan, H.S. White, B. Wheeler, A.J. Bard, Semiconductor electrodes: XXIX. High efficiency photoelectrochemical solar cells with n-WSe_2 electrodes in an aqueous iodide medium, J. Electrochem. Soc. 127 (1980) 518–520.
[216] L.F. Schneemeyer, M.S. Wrighton, Flat-band potential of n-type semiconducting molybdenum disulfide by cyclic voltammetry of two-electron reductants: interface energetics and the sustained photooxidation of chloride, J. Am. Chem. Soc. 101 (1979) 6496–6500.
[217] H. Tributsch, Photoelectrochemical behaviour of layer-type transition metal dichalcogenides, Faraday Discuss. Chem. Soc. 70 (1980) 189–205.
[218] J. Gobrecht, H. Tributsch, H. Gerischer, Performance of synthetical n-$MoSe_2$ in electrochemical solar cells, J. Electrochem. Soc. 125 (1978) 2085–2086.
[219] H. Tributsch, Hole reactions from d-energy bands of layer type group VI transition metal dichalcogenides: new perspectives for electrochemical solar energy conversion, J. Electrochem. Soc. 125 (1978) 1086–1093.
[220] G.S. Calabrese, M.S. Wrighton, Photoelectrochemical oxidation of sulfur dioxide in strong acid solution: iodide-mediated oxidation at illuminated metal dichalcogenide electrodes, J. Am. Chem. Soc. 103 (1981) 6273–6280.
[221] L.F. Schneemeyer, M.S. Wrighton, n-Type molybdenum diselenide-based photoelectrochemical cells: evidence for Fermi level pinning and comparison of the efficiency for conversion of light to electricity with various solvent/halogen/halide combinations, J. Am. Chem. Soc. 102 (1980) 6964–6971.
[222] B.R. Horrocks, M.V. Mirkin, A.J. Bard, Scanning electrochemical microscopy. 25. Application to investigation of the kinetics of heterogeneous electron transfer at semiconductor (WSe_2 and Si) electrodes, J. Phys. Chem. 98 (1994) 9106–9114.
[223] C. Tan, J. Rodríguez-López, J.J. Parks, N.L. Ritzert, D.C. Ralph, H.D. Abruña, Reactivity of monolayer chemical vapor deposited graphene imperfections studied using scanning electrochemical microscopy, ACS Nano 6 (2012) 3070–3079.
[224] A.G. Güell, A.S. Cuharuc, Y.-R. Kim, G. Zhang, S.-Y. Tan, N. Ebejer, P.R. Unwin, Redox-dependent spatially resolved electrochemistry at graphene and graphite step edges, ACS Nano 9 (2015) 3558–3571.
[225] A.J. Wain, A.J. Pollard, C. Richter, High-resolution electrochemical and topographical imaging using batch-fabricated cantilever probes, Anal. Chem. 86 (2014) 5143–5149.
[226] J. Xia, F. Chen, J. Li, N. Tao, Measurement of the quantum capacitance of graphene, Nat. Nanotechnol. 4 (2009) 505–509.
[227] H. Ji, X. Zhao, Z. Qiao, J. Jung, Y. Zhu, Y. Lu, L.L. Zhang, A.H. MacDonald, R.S. Ruoff, Capacitance of carbon-based electrical double-layer capacitors, Nat. Commun. 5 (2014) 3317.
[228] D.A. Bandurin, A.V. Tyurnina, G.L. Yu, A. Mishchenko, V. Zólyomi, S.V. Morozov, R.K. Kumar, R.V. Gorbachev, Z.R. Kudrynskyi, S. Pezzini, Z.D. Kovalyuk, U. Zeitler, K.S. Novoselov, A. Patanè, L. Eaves, I.V. Grigorieva, V.I. Fal'ko, A.K. Geim, Y. Cao, High electron mobility, quantum Hall effect and anomalous optical response in atomically thin InSe, Nat. Nanotechnol. 12 (2016) 223–227.
[229] B.W.H. Baugher, H.O.H. Churchill, Y. Yang, P. Jarillo-Herrero, Intrinsic electronic transport properties of high-quality monolayer and bilayer MoS_2, Nano Lett. 13 (2013) 4212–4216.
[230] D.A.C. Brownson, L.J. Munro, D.K. Kampouris, C.E. Banks, Electrochemistry of graphene: not such a beneficial electrode material? RSC Adv. 1 (2011) 978–988.
[231] A.G. Güell, N. Ebejer, M.E. Snowden, J.V. MacPherson, P.R. Unwin, Structural correlations in heterogeneous electron transfer at monolayer and multilayer graphene electrodes, J. Am. Chem. Soc. 134 (2012) 7258–7261.
[232] W. Li, C. Tan, M.A. Lowe, H.D. Abruña, D.C. Ralph, Electrochemistry of individual monolayer graphene sheets, ACS Nano 5 (2011) 2264–2270.
[233] M.S. Goh, M. Pumera, The electrochemical response of graphene sheets is independent of the number of layers from a single graphene sheet to multilayer stacked graphene platelets, Chem. Asian J. 5 (2010) 2355–2357.
[234] H.V. Patten, M. Velický, R.A.W. Dryfe, Electrochemistry of graphene, in: R.C. Alkire, P.N. Bartlett, J. Lipkowski (Eds.), Electrochemistry of Carbon Electrodes, Wiley-VCH Verlag GmbH & Co. KGaA, 2015, pp. 121–162.
[235] Y. Son, Q.H. Wang, J.A. Paulson, C.-J. Shih, A.G. Rajan, K. Tvrdy, S. Kim, B. Alfeeli, R.D. Braatz, M.S. Strano, Layer number dependence of MoS_2 photoconductivity using photocurrent spectral atomic force microscopic imaging, ACS Nano 9 (2015) 2843–2855.
[236] C.E. Banks, T.J. Davies, G.G. Wildgoose, R.G. Compton, Electrocatalysis at graphite and carbon nanotube modified electrodes: edge-plane sites and tube ends are the reactive sites, Chem. Commun. (Camb. UK) (2005) 829–841.
[237] A. Ambrosi, A. Bonanni, M. Pumera, Electrochemistry of folded graphene edges, Nanoscale 3 (2011) 2256–2260.
[238] M.A. Edwards, P. Bertoncello, P.R. Unwin, Slow diffusion reveals the intrinsic electrochemical activity of basal plane highly oriented pyrolytic graphite electrodes, J. Phys. Chem. C 113 (2009) 9218–9223.
[239] J.-H. Zhong, J. Zhang, X. Jin, J.-Y. Liu, Q. Li, M.-H. Li, W. Cai, D.-Y. Wu, D. Zhan, B. Ren, Quantitative correlation between defect density and heterogeneous electron transfer rate of single layer graphene, J. Am. Chem. Soc. 136 (2014) 16609–16617.
[240] B. Liu, L.-J. Wu, Y.-Q. Zhao, L.-Z. Wang, M.-Q. Cai, Tuning the Schottky barrier height of the Pd-MoS_2 contact by different strains, Phys. Chem. Chem. Phys. 17 (2015) 27088–27093.
[241] J.E. Padilha, H. Peelaers, A. Janotti, C.G. Van de Walle, Nature and evolution of the band-edge states in MoS_2: from monolayer to bulk, Phys. Rev. B 90 (2014) 205420.
[242] C. Zhang, A. Johnson, C.L. Hsu, L.J. Li, C.K. Shih, Direct imaging of band profile in single layer MoS_2 on graphite: quasiparticle energy gap, metallic edge states, and edge band bending, Nano Lett. 14 (2014) 2443–2447.
[243] A. Ashraf, Y. Wu, M.C. Wang, N.R. Aluru, S.A. Dastgheib, S.W. Nam, Spectroscopic investigation of the wettability of multilayer graphene using highly ordered pyrolytic graphite as a model material, Langmuir 30 (2014) 12827–12836.
[244] Y.J. Shin, Y. Wang, H. Huang, G. Kalon, A.T.S. Wee, Z. Shen, C.S. Bhatia, H. Yang, Surface-energy engineering of graphene, Langmuir 26 (2010) 3798–3802.
[245] K.K. Kam, B.A. Parkinson, Detailed photocurrent spectroscopy of the semiconducting group VI transition metal dichalcogenides, J. Phys. Chem. 86 (1982) 463–467.
[246] Z. Chen, A.J. Forman, T.F. Jaramillo, Bridging the gap between bulk and nanostructured photoelectrodes: the impact of surface states on the electrocatalytic and photoelectrochemical properties of MoS_2, J. Phys. Chem. C 117 (2013) 9713–9722.
[247] C.A. Klein, W.D. Straub, Carrier densities and mobilities in pyrolytic graphite, Phys. Rev. 123 (1961) 1581–1583.
[248] K. Dolui, I. Rungger, S. Sanvito, Origin of the n-type and p-type conductivity of MoS_2 monolayers on a SiO_2 substrate, Phys. Rev. B: Condens. Matter Mater. Phys. 87 (2013) 165402.
[249] C. Ruppert, O.B. Aslan, T.F. Heinz, Optical properties and band gap of single- and few-layer $MoTe_2$ crystals, Nano Lett. 14 (2014) 6231–6236.
[250] A.N. Patel, M.G. Collignon, M.A. Oconnell, W.O.Y. Hung, K. McKelvey, J.V. MacPherson, P.R. Unwin, A new view of electrochemistry at highly oriented pyrolytic graphite, J. Am. Chem. Soc. 134 (2012) 20117–20130.
[251] D.J. Late, B. Liu, H.S.S.R. Matte, V.P. Dravid, C.N.R. Rao, Hysteresis in single-layer MoS_2 field effect transistors, ACS Nano 6 (2012) 5635–5641.
[252] K.R. Kneten, R.L. McCreery, Effects of redox system structure on electron-transfer kinetics at ordered graphite and glassy carbon electrodes, Anal. Chem. 64 (1992) 2518–2524.
[253] N. Nioradze, R. Chen, N. Kurapati, A. Khvataeva-Domanov, S. Mabic, S. Amemiya, Organic contamination of highly oriented pyrolytic graphite as studied by scanning electrochemical microscopy, Anal. Chem. 87 (2015) 4836–4843.
[254] Z. Li, A. Kozbial, N. Nioradze, D. Parobek, G.J. Shenoy, M. Salim, S. Amemiya, L. Li, H. Liu, Water protects graphitic surface from airborne hydrocarbon contamination, ACS Nano 10 (2016) 349–359.
[255] D.J. Lomax, P. Kant, A.T. Williams, H.V. Patten, Y. Zou, A. Juel, R.A.W. Dryfe, Ultra-low voltage electrowetting using graphite surfaces, Soft Matter 12 (2016) 8798–8804.
[256] Y.C. Lin, C.C. Lu, C.H. Yeh, C. Jin, K. Suenaga, P.W. Chiu, Graphene annealing: how clean can it be? Nano Lett. 12 (2012) 414–419.
[257] M. Her, R. Beams, L. Novotny, Graphene transfer with reduced residue, Phys. Lett. A 377 (2013) 1455–1458.
[258] J.W. Suk, W.H. Lee, J. Lee, H. Chou, R.D. Piner, Y. Hao, D. Akinwande, R.S. Ruoff, Enhancement of the electrical properties of graphene grown by chemical vapor deposition via controlling the effects of polymer residue, Nano Lett. 13 (2013) 1462–1467.
[259] H.V. Patten, M. Velický, N. Clark, C.A. Muryn, I.A. Kinloch, R.A.W. Dryfe, Electrochemistry of well-defined graphene samples: role of contaminants, Faraday Discuss. 172 (2014) 261–271.
[260] S. Ross, A. Sussman, Surface oxidation of molybdenum disulfide, J. Phys. Chem. 59 (1955) 889–892.
[261] R.R.M. Johnston, A.J.W. Moore, Water adsorption on molybdenum bisulfide containing surface contaminants, J. Phys. Chem. 68 (1964) 3399–3406.
[262] W. Bao, X. Cai, D. Kim, K. Sridhara, M.S. Fuhrer, High mobility ambipolar MoS_2 field-effect transistors: substrate and dielectric effects, Appl. Phys. Lett. 102 (2013) 042104.
[263] W. Feng, W. Zheng, W. Cao, P. Hu, Back gated multilayer InSe transistors with enhanced carrier mobilities via the suppression of carrier scattering from a dielectric interface, Adv. Mater. 26 (2014) 6587–6593.
[264] A.S. Mayorov, R.V. Gorbachev, S.V. Morozov, L. Britnell, R. Jalil, L.A. Ponomarenko, P. Blake, K.S. Novoselov, K. Watanabe, T. Taniguchi, A.K. Geim, Micrometer-scale ballistic transport in encapsulated graphene at room temperature, Nano Lett. 11 (2011) 2396–2399.
[265] J. Hui, X. Zhou, R. Bhargava, A. Chinderle, J. Zhang, J. Rodríguez-López, Kinetic modulation of outer-sphere electron transfer reactions on graphene electrode with a sub-surface metal substrate, Electrochim. Acta 211 (2016) 1016–1023.
[266] U.S. Department of Energy's Office of Energy Efficiency and Renewable Energy, 2017 (accessed 08.03.17) https://energy.gov/eere/fuelcells/hydrogen-storage.

[267] B.E. Conway, B.V. Tilak, Interfacial processes involving electrocatalytic evolution and oxidation of H_2, and the role of chemisorbed H, Electrochim. Acta 47 (2002) 3571–3594.
[268] M.A. Lukowski, A.S. Daniel, F. Meng, A. Forticaux, L. Li, S. Jin, Enhanced hydrogen evolution catalysis from chemically exfoliated metallic MoS_2 nanosheets, J. Am. Chem. Soc. 135 (2013) 10274–10277.
[269] Y. Yu, S.-Y. Huang, Y. Li, S.N. Steinmann, W. Yang, L. Cao, Layer-dependent electrocatalysis of MoS_2 for hydrogen evolution, Nano Lett. 14 (2014) 553–558.
[270] H. Zhu, M. Du, M. Zhang, M. Zou, T. Yang, S. Wang, J. Yao, B. Guo, S-rich single-layered MoS_2 nanoplates embedded in N-doped carbon nanofibers: efficient co-electrocatalysts for the hydrogen evolution reaction, Chem. Commun. (Camb. UK) 50 (2014) 15435–15438.
[271] Y. Li, H. Wang, L. Xie, Y. Liang, G. Hong, H. Dai, MoS_2 nanoparticles grown on graphene: an advanced catalyst for the hydrogen evolution reaction, J. Am. Chem. Soc. 133 (2011) 7296–7299.
[272] H. Wang, Z. Lu, S. Xu, D. Kong, J.J. Cha, G. Zheng, P.C. Hsu, K. Yan, D. Bradshaw, F.B. Prinz, Y. Cui, Electrochemical tuning of vertically aligned MoS_2 nanofilms and its application in improving hydrogen evolution reaction, Proc. Natl. Acad. Sci. U. S. A. 110 (2013) 19701–19706.
[273] T.F. Jaramillo, K.P. Jørgensen, J. Bonde, J.H. Nielsen, S. Horch, I. Chorkendorff, Identification of active edge sites for electrochemical H_2 evolution from MoS_2 nanocatalysts, Science 317 (2007) 100–102.
[274] D. Voiry, M. Salehi, R. Silva, T. Fujita, M. Chen, T. Asefa, V.B. Shenoy, G. Eda, M. Chhowalla, Conducting MoS_2 nanosheets as catalysts for hydrogen evolution reaction, Nano Lett. 13 (2013) 6222–6227.
[275] J. Yang, K. Wang, J. Zhu, C. Zhang, T. Liu, Self-templated growth of vertically aligned 2H-1T MoS_2 for efficient electrocatalytic hydrogen evolution, ACS Appl. Mater. Interfaces 8 (2016) 31702–31708.
[276] H. Wang, D. Kong, P. Johanes, J.J. Cha, G. Zheng, K. Yan, N. Liu, Y. Cui, $MoSe_2$ and WSe_2 nanofilms with vertically aligned molecular layers on curved and rough surfaces, Nano Lett. 13 (2013) 3426–3433.
[277] X. Yu, M.S. Prévot, N. Guijarro, K. Sivula, Self-assembled 2D WSe_2 thin films for photoelectrochemical hydrogen production, Nat. Commun. 6 (2015) 7596.
[278] D. Voiry, H. Yamaguchi, J. Li, R. Silva, D.C.B. Alves, T. Fujita, M. Chen, T. Asefa, V.B. Shenoy, G. Eda, M. Chhowalla, Enhanced catalytic activity in strained chemically exfoliated WS_2 nanosheets for hydrogen evolution, Nat. Mater. 12 (2013) 850–855.
[279] X. Cong, C. Cheng, Y. Liao, Y. Ye, C. Dong, H. Sun, X. Ji, W. Zhang, P. Fang, L. Miao, J. Jiang, Intrinsic charge storage capability of transition metal dichalcogenides as pseudocapacitor electrodes, J. Phys. Chem. C 119 (2015) 20864–20870.
[280] Z. Hu, S. Zhang, Y.-N. Zhang, D. Wang, H. Zeng, L.-M. Liu, Modulating the phase transition between metallic and semiconducting single-layer MoS_2 and WS_2 through size effects, Phys. Chem. Chem. Phys. 17 (2015) 1099–1105.
[281] A.Y.S. Eng, A. Ambrosi, Z. Sofer, P. Šimek, M. Pumera, Electrochemistry of transition metal dichalcogenides: strong dependence on the metal-to-chalcogen composition and exfoliation method, ACS Nano 8 (2014) 12185–12198.
[282] X. Chia, A. Ambrosi, D. Sedmidubský, Z. Sofer, M. Pumera, Precise tuning of the charge transfer kinetics and catalytic properties of MoS_2 materials via electrochemical methods, Chem. Eur. J. 20 (2014) 17426–17432.
[283] X. Chia, P. Lazar, Z. Sofer, J. Luxa, M. Pumera, Layered SnS versus SnS_2: valence and structural implications on electrochemistry and clean energy electrocatalysis, J. Phys. Chem. C 120 (2016) 24098–24111.
[284] S.M. Tan, C.K. Chua, D. Sedmidubský, Z.k. Sofer, M. Pumera, Electrochemistry of layered GaSe and GeS: applications to ORR, OER and HER, Phys. Chem. Chem. Phys. 18 (2016) 1699–1711.
[285] P. Calvert, Inkjet printing for materials and devices, Chem. Mater. 13 (2001) 3299–3305.
[286] D.C. Marcano, D.V. Kosynkin, J.M. Berlin, A. Sinitskii, Z. Sun, A. Slesarev, L.B. Alemany, W. Lu, J.M. Tour, Improved synthesis of graphene oxide, ACS Nano 4 (2010) 4806–4814.
[287] S. Stankovich, D.A. Dikin, R.D. Piner, K.A. Kohlhaas, A. Kleinhammes, Y. Jia, Y. Wu, S.T. Nguyen, R.S. Ruoff, Synthesis of graphene-based nanosheets via chemical reduction of exfoliated graphite oxide, Carbon 45 (2007) 1558–1565.
[288] D.A. Dikin, S. Stankovich, E.J. Zimney, R.D. Piner, G.H.B. Dommett, G. Evmenenko, S.T. Nguyen, R.S. Ruoff, Preparation and characterization of graphene oxide paper, Nature 448 (2007) 457–460.
[289] J.R. Potts, D.R. Dreyer, C.W. Bielawski, R.S. Ruoff, Graphene-based polymer nanocomposites, Polymer 52 (2011) 5–25.
[290] T. Ramanathan, A.A. Abdala, S. Stankovich, D.A. Dikin, M. Herrera Alonso, R.D. Piner, D.H. Adamson, H.C. Schniepp, X. Chen, R.S. Ruoff, S.T. Nguyen, I.A. Aksay, R.K. Prud'Homme, L.C. Brinson, Functionalized graphene sheets for polymer nanocomposites, Nat. Nanotechnol. 3 (2008) 327–331.
[291] F. Kopnov, Y. Feldman, R. Popovitz-Biro, A. Vilan, H. Cohen, A. Zak, R. Tenne, Intercalation of alkali metal in WS_2 nanoparticles, revisited, Chem. Mater. 20 (2008) 4099–4105.
[292] A.S. Golub', D.P. Rupasov, N.D. Lenenko, Y.N. Novikov, Modification of molybdenum disulfide (2H-MoS_2) and synthesis of its intercalation compounds, Russ. J. Inorg. Chem. 55 (2010) 1166–1171.
[293] J. Zou, C. Sole, N.E. Drewett, M. Velický, L.J. Hardwick, In situ study of Li intercalation into highly crystalline graphitic flakes of varying thicknesses, J. Phys. Chem. Lett. 7 (2016) 4291–4296.
[294] Y. Wang, J.Z. Ou, S. Balendhran, A.F. Chrimes, M. Mortazavi, D.D. Yao, M.R. Field, K. Latham, V. Bansal, J.R. Friend, S. Zhuiykov, N.V. Medhekar, M.S. Strano, K. Kalantar-Zadeh, Electrochemical control of photoluminescence in two-dimensional MoS_2 nanoflakes, ACS Nano 7 (2013) 10083–10093.
[295] Y. Wang, Z. Sofer, J. Luxa, M. Pumera, Lithium exfoliated vanadium dichalcogenides (VS_2, VSe_2, VTe_2) exhibit dramatically different properties from their bulk counterparts, Adv. Mater. Interfaces 3 (2016) 1600433.
[296] S. Balendhran, S. Walia, H. Nili, J.Z. Ou, S. Zhuiykov, R.B. Kaner, S. Sriram, M. Bhaskaran, K. Kalantar-zadeh, Two-dimensional molybdenum trioxide and dichalcogenides, Adv. Funct. Mater. 23 (2013) 3952–3970.
[297] F. Bonaccorso, L. Colombo, G. Yu, M. Stoller, V. Tozzini, A.C. Ferrari, R.S. Ruoff, V. Pellegrini, Graphene, related two-dimensional crystals, and hybrid systems for energy conversion and storage, Science 347 (2015) 1246501.
[298] X. Chen, A.R. McDonald, Functionalization of two-dimensional transition-metal dichalcogenides, Adv. Mater. 28 (2016) 5738–5746.
[299] Z. Liu, S.P. Lau, F. Yan, Functionalized graphene and other two-dimensional materials for photovoltaic devices: device design and processing, Chem. Soc. Rev. 44 (2015) 5638–5679.
[300] H. Schmidt, F. Giustiniano, G. Eda, Electronic transport properties of transition metal dichalcogenide field-effect devices: surface and interface effects, Chem. Soc. Rev. 44 (2015) 7715–7736.
[301] R. Sharma, J.H. Baik, C.J. Perera, M.S. Strano, Anomalously large reactivity of single graphene layers and edges toward electron transfer chemistries, Nano Lett. 10 (2010) 398–405.
[302] G.L.C. Paulus, Q.H. Wang, M.S. Strano, Covalent electron transfer chemistry of graphene with diazonium salts, Acc. Chem. Res. 46 (2013) 160–170.
[303] D. Voiry, A. Goswami, R. Kappera, C. de Carvalho Castro e Silva, D. Kaplan, T. Fujita, M. Chen, T. Asefa, M. Chhowalla, Covalent functionalization of monolayered transition metal dichalcogenides by phase engineering, Nat. Chem. 7 (2015) 45–49.
[304] K.C. Knirsch, N.C. Berner, H.C. Nerl, C.S. Cucinotta, Z. Gholamvand, N. McEvoy, Z. Wang, I. Abramovic, P. Vecera, M. Halik, S. Sanvito, G.S. Duesberg, V. Nicolosi, F. Hauke, A. Hirsch, J.N. Coleman, C. Backes, Basal-plane functionalization of chemically exfoliated molybdenum disulfide by diazonium salts, ACS Nano 9 (2015) 6018–6030.
[305] S. Presolski, M. Pumera, Covalent functionalization of MoS_2, Mater. Today 19 (2016) 140–145.
[306] S. Lei, X. Wang, B. Li, J. Kang, Y. He, A. George, L. Ge, Y. Gong, P. Dong, Z. Jin, G. Brunetto, W. Chen, Z.-T. Lin, R. Baines, D.S. Galvão, J. Lou, E. Barrera, K. Banerjee, R. Vajtai, P. Ajayan, Surface functionalization of two-dimensional metal chalcogenides by Lewis acid–base chemistry, Nat. Nanotechnol. 11 (2016) 465–471.
[307] C.R. Ryder, J.D. Wood, S.A. Wells, Y. Yang, D. Jariwala, T.J. Marks, G.C. Schatz, M.C. Hersam, Covalent functionalization and passivation of exfoliated black phosphorus via aryl diazonium chemistry, Nat. Chem. 8 (2016) 597–602.
[308] E.P. Nguyen, B.J. Carey, C.J. Harrison, P. Atkin, K.J. Berean, E. Della Gaspera, J.Z. Ou, R.B. Kaner, K. Kalantar-zadeh, T. Daeneke, Excitation dependent bidirectional electron transfer in phthalocyanine-functionalised MoS_2 nanosheets, Nanoscale 8 (2016) 16276–16283.
[309] X. Yu, A. Rahmanudin, X.A. Jeanbourquin, D. Tsokkou, N. Guijarro, N. Banerji, K. Sivula, Hybrid heterojunctions of solution-processed semiconducting 2D transition metal dichalcogenides, ACS Energy Lett. 2 (2017) 524–531.
[310] X. Ling, W. Fang, Y.H. Lee, P.T. Araujo, X. Zhang, J.F. Rodriguez-Nieva, Y. Lin, J. Zhang, J. Kong, M.S. Dresselhaus, Raman enhancement effect on two-dimensional layered materials: graphene, h-BN and MoS_2, Nano Lett. 14 (2014) 3033–3040.
[311] M. Amani, D.-H. Lien, D. Kiriya, J. Xiao, A. Azcatl, J. Noh, S.R. Madhvapathy, R. Addou, S. KC, M. Dubey, K. Cho, R.M. Wallace, S.-C. Lee, J.-H. He, J.W. Ager, X. Zhang, E. Yablonovitch, A. Javey, Near-unity photoluminescence quantum yield in MoS_2, Science 350 (2015) 1065–1068.
[312] L. Zhang, J. Yu, M. Yang, Q. Xie, H. Peng, Z. Liu, Janus graphene from asymmetric two-dimensional chemistry, Nat. Commun. 4 (2013) 1443.
[313] P.S. Toth, Q.M. Ramasse, M. Velický, R.A.W. Dryfe, Functionalization of graphene at the organic/water interface, Chem. Sci. 6 (2015) 1316–1323.
[314] P.S. Toth, M. Velický, M.A. Bissett, T.J.A. Slater, N. Savjani, A.K. Rabiu, A.M. Rakowski, J.R. Brent, S.J. Haigh, P. O'Brien, R.A.W. Dryfe, Asymmetric MoS_2/graphene/metal sandwiches: preparation, characterization, and application, Adv. Mater. 28 (2016) 8256–8264.
[315] P.S. Toth, M. Velický, Q.M. Ramasse, D.M. Kepaptsoglou, R.A.W. Dryfe, Symmetric and asymmetric decoration of graphene: bimetal-graphene sandwiches, Adv. Funct. Mater. 25 (2015) 2899–2909.
[316] J. Kim, S. Byun, A.J. Smith, J. Yu, J. Huang, Enhanced electrocatalytic properties of transition-metal dichalcogenides sheets by spontaneous gold nanoparticle decoration, J. Phys. Chem. Lett. 4 (2013) 1227–1232.
[317] Z. Samec, Dynamic electrochemistry at the interface between two immiscible electrolytes, Electrochim. Acta 84 (2012) 21–28.
[318] E. Aslan, I. HatayPatir, M. Ersoz, Catalytic hydrogen evolution by tungsten disulfide at liquid–liquid interfaces, ChemCatChem 6 (2014) 2832–2835.
[319] I. Hatay, P.Y. Ge, H. Vrubel, X. Hu, H.H. Girault, Hydrogen evolution at polarised liquid/liquid interfaces catalyzed by molybdenum disulfide, Energy Environ. Sci. 4 (2011) 4246–4251.
[320] D. McManus, S. Vranic, F. Withers, V. Sanchez-Romaguera, M. Macucci, H. Yang, R. Sorrentino, K. Parvez, S.-K. Son, G. Iannaccone, K. Kostarelos, G.

Fiori, C. Casiraghi, Water-based and biocompatible 2D crystal inks for all-inkjet-printed heterostructures, Nat. Nanotechnol. (2017), http://dx.doi.org/10.1038/nnano.2016.1281.
[321] A.G. Kelly, D. Finn, A. Harvey, T. Hallam, J.N. Coleman, All-printed capacitors from graphene-BN-graphene nanosheet heterostructures, Appl. Phys. Lett. 109 (2016) 023107.
[322] A. Capasso, A.E. Del Rio Castillo, H. Sun, A. Ansaldo, V. Pellegrini, F. Bonaccorso, Ink-jet printing of graphene for flexible electronics: an environmentally-friendly approach, Solid State Commun. 224 (2015) 53–63.
[323] L.E. Conroy, K.C. Park, Electrical properties of the Group IV disulfides, TiS_2, ZrS_2, HfS_2, and SnS_2, Inorg. Chem. 7 (1968) 459–463.
[324] P. Mirõ, M. Ghorbani-Asl, T. Heine, Two dimensional materials beyond MoS_2: noble-transition-metal dichalcogenides, Angew. Chem. Int. Ed. 53 (2014) 3015–3018.
[325] X. Chia, A. Adriano, P. Lazar, Z. Sofer, J. Luxa, M. Pumera, Layered platinum dichalcogenides (PtS_2, $PtSe_2$, and $PtTe_2$) electrocatalysis: monotonic dependence on the chalcogen size, Adv. Funct. Mater. 26 (2016) 4306–4318.
[326] L.A. Burton, D. Colombara, R.D. Abellon, F.C. Grozema, L.M. Peter, T.J. Savenije, G. Dennler, A. Walsh, Synthesis, characterization, and electronic structure of single-crystal SnS, Sn_2S_3, and SnS_2, Chem. Mater. 25 (2013) 4908–4916.
[327] L.A. Burton, T.J. Whittles, D. Hesp, W.M. Linhart, J.M. Skelton, B. Hou, R.F. Webster, G. O'Dowd, C. Reece, D. Cherns, D.J. Fermin, T.D. Veal, V.R. Dhanak, A. Walsh, Electronic and optical properties of single crystal SnS_2: an earth-abundant disulfide photocatalyst, J. Mater. Chem. A 4 (2016) 1312–1318.
[328] J.R. Brent, D.J. Lewis, T. Lorenz, E.A. Lewis, N. Savjani, S.J. Haigh, G. Seifert, B. Derby, P. O'Brien, Tin(II) sulfide (SnS) nanosheets by liquid-phase exfoliation of herzenbergite: IV–VI main group two-dimensional atomic crystals, J. Am. Chem. Soc. 137 (2015) 12689–12696.
[329] H.S. Song, S.L. Li, L. Gao, Y. Xu, K. Ueno, J. Tang, Y.B. Cheng, K. Tsukagoshi, High-performance top-gated monolayer SnS_2 field-effect transistors and their integrated logic circuits, Nanoscale 5 (2013) 9666–9670.
[330] Z. Tian, C. Guo, M. Zhao, R. Li, J. Xue, Two-dimensional SnS: a phosphorene analogue with strong in-plane electronic anisotropy, ACS Nano 11 (2017) 2219–2226.
[331] N.H. Tu, Y. Tanabe, Y. Satake, K.K. Huynh, K. Tanigaki, In-plane topological p–n junction in the three-dimensional topological insulator $Bi_{2-x}Sb_xTe_{3-y}Se_y$, Nat. Commun. 7 (2016) 13763.
[332] Y. Xu, B. Yan, H.-J. Zhang, J. Wang, G. Xu, P. Tang, W. Duan, S.-C. Zhang, Large-gap quantum spin hall insulators in tin films, Phys. Rev. Lett. 111 (2013) 136804.
[333] H. Zhao, C.-W. Zhang, W.-X. Ji, R.-W. Zhang, S.-S. Li, S.-S. Yan, B.-M. Zhang, P. Li, P.-J. Wang, Unexpected giant-gap quantum spin hall insulator in chemically decorated plumbene monolayer, Sci. Rep. 6 (2016) 20152.
[334] Y. Cao, A. Mishchenko, G.L. Yu, E. Khestanova, A.P. Rooney, E. Prestat, A.V. Kretinin, P. Blake, M.B. Shalom, C. Woods, J. Chapman, G. Balakrishnan, I.V. Grigorieva, K.S. Novoselov, B.A. Piot, M. Potemski, K. Watanabe, T. Taniguchi, S.J. Haigh, A.K. Geim, R.V. Gorbachev, Quality heterostructures from two-dimensional crystals unstable in air by their assembly in inert atmosphere, Nano Lett. 15 (2015) 4914–4921.
[335] G.W. Mudd, M.R. Molas, X. Chen, V. Zólyomi, K. Nogajewski, Z.R. Kudrynskyi, Z.D. Kovalyuk, G. Yusa, O. Makarovsky, L. Eaves, M. Potemski, V.I. Fal'ko, A. Patanè, The direct-to-indirect band gap crossover in two-dimensional van der Waals indium selenide crystals, Sci. Rep. 6 (2016) 39619.
[336] V. Tran, R. Soklaski, Y. Liang, L. Yang, Layer-controlled band gap and anisotropic excitons in few-layer black phosphorus, Phys. Rev. B 89 (2014) 235319.
[337] Y. Saito, Y. Iwasa, Ambipolar insulator-to-metal transition in black phosphorus by ionic-liquid gating, ACS Nano 9 (2015) 3192–3198.
[338] J. Hu, Z. Guo, P.E. McWilliams, J.E. Darges, D.L. Druffel, A.M. Moran, S.C. Warren, Band gap engineering in a 2D material for solar-to-chemical energy conversion, Nano Lett. 16 (2016) 74–79.
[339] C.-H. Lee, G.-H. Lee, A.M. van der Zande, W. Chen, Y. Li, M. Han, X. Cui, G. Arefe, C. Nuckolls, T.F. Heinz, J. Guo, J. Hone, P. Kim, Atomically thin p–n junctions with van der Waals heterointerfaces, Nat. Nanotechnol. 9 (2014) 676–681.
[340] G.W. Mudd, S.A. Svatek, L. Hague, O. Makarovsky, Z.R. Kudrynskyi, C.J. Mellor, P.H. Beton, L. Eaves, K.S. Novoselov, Z.D. Kovalyuk, E.E. Vdovin, A.J. Marsden, N.R. Wilson, A. Patanè, High broad-band photoresponsivity of mechanically formed InSe–graphene van der Waals heterostructures, Adv. Mater. 27 (2015) 3760–3766.
[341] P. Rivera, J.R. Schaibley, A.M. Jones, J.S. Ross, S. Wu, G. Aivazian, P. Klement, K. Seyler, G. Clark, N.J. Ghimire, J. Yan, D.G. Mandrus, W. Yao, X. Xu, Observation of long-lived interlayer excitons in monolayer $MoSe_2$–WSe_2 heterostructures, Nat. Commun. 6 (2015) 6242.
[342] X. Hong, J. Kim, S.-F. Shi, Y. Zhang, C. Jin, Y. Sun, S. Tongay, J. Wu, Y. Zhang, F. Wang, Ultrafast charge transfer in atomically thin MoS_2/WS_2 heterostructures, Nat. Nanotechnol. 9 (2014) 682–686.
[343] Y. Son, M.-Y. Li, C.-C. Cheng, K.-H. Wei, P. Liu, Q.H. Wang, L.-J. Li, M.S. Strano, Observation of switchable photoresponse of a monolayer WSe_2–MoS_2 lateral heterostructure via photocurrent spectral atomic force microscopic imaging, Nano Lett. 16 (2016) 3571–3577.
[344] S.I. Boldish, W.B. White, Optical band gaps of selected ternary sulfide minerals, Am. Mineral. 83 (1998) 865–871.
[345] A.J. Molina-Mendoza, E. Giovanelli, W.S. Paz, M.A. Niño, J.O. Island, C. Evangeli, L. Aballe, M. Foerster, H.S.J. van der Zant, G. Rubio-Bollinger, N. Agraït, J.J. Palacios, E.M. Pérez, A. Castellanos-Gomez, Franckeite as a naturally occurring van der Waals heterostructure, Nat. Commun. 8 (2017) 14409.
[346] M.F. Craciun, S. Russo, M. Yamamoto, J.B. Oostinga, A.F. Morpurgo, S. Tarucha, Trilayer graphene is a semimetal with a gate-tunable band overlap, Nat. Nanotechnol. 4 (2009) 383–388.
[347] Y. Zhang, T.T. Tang, C. Girit, Z. Hao, M.C. Martin, A. Zettl, M.F. Crommie, Y.R. Shen, F. Wang, Direct observation of a widely tunable bandgap in bilayer graphene, Nature 459 (2009) 820–823.
[348] Q. Yue, S. Chang, J. Kang, X. Zhang, Z. Shao, S. Qin, J. Li, Bandgap tuning in armchair MoS_2 nanoribbon, J. Phys. Condens. Matter 24 (2012) 335501.
[349] E.J.G. Santos, E. Kaxiras, Electrically driven tuning of the dielectric constant in MoS_2 layers, ACS Nano 7 (2013) 10741–10746.
[350] T. Chu, H. Ilatikhameneh, G. Klimeck, R. Rahman, Z. Chen, Electrically tunable bandgaps in bilayer MoS_2, Nano Lett. 15 (2015) 8000–8007.
[351] C.H. Lui, A.J. Frenzel, D.V. Pilon, Y.H. Lee, X. Ling, G.M. Akselrod, J. Kong, N. Gedik, Trion-induced negative photoconductivity in monolayer MoS_2, Phys. Rev. Lett. 113 (2014) 166801.
[352] K. Matsuki, J. Pu, D. Kozawa, K. Matsuda, L.-J. Li, T. Takenobu, Effects of electrolyte gating on photoluminescence spectra of large-area WSe_2 monolayer films, Jpn. J. Appl. Phys. 55 (2016), 06GB02.
[353] M.M. Perera, M.-W. Lin, H.-J. Chuang, B.P. Chamlagain, C. Wang, X. Tan, M.M.-C. Cheng, D. Tománek, Z. Zhou, Improved carrier mobility in few-layer MoS_2 field-effect transistors with ionic-liquid gating, ACS Nano 7 (2013) 4449–4458.
[354] A. Allain, A. Kis, Electron and hole mobilities in single-layer WSe_2, ACS Nano 8 (2014) 7180–7185.
[355] P.S. Toth, A. Valota, M. Velický, I. Kinloch, K. Novoselov, E.W. Hill, R.A.W. Dryfe, Electrochemistry in a drop: a study of the electrochemical behaviour of mechanically exfoliated graphene on photoresist coated silicon substrate, Chem. Sci. 5 (2014) 582–589.
[356] Y. Li, C.Y. Xu, J.K. Qin, W. Feng, J.Y. Wang, S. Zhang, L.P. Ma, J. Cao, P.A. Hu, W. Ren, L. Zhen, Tuning the excitonic states in MoS_2/graphene van der Waals heterostructures via electrochemical gating, Adv. Funct. Mater. 26 (2016) 293–302.
[357] H.J. Conley, B. Wang, J.I. Ziegler, R.F. Haglund, S.T. Pantelides, K.I. Bolotin, Bandgap engineering of strained monolayer and bilayer MoS_2, Nano Lett. 13 (2013) 3626–3630.
[358] S. Horzum, H. Sahin, S. Cahangirov, P. Cudazzo, A. Rubio, T. Serin, F.M. Peeters, Phonon softening and direct to indirect band gap crossover in strained single-layer $MoSe_2$, Phys. Rev. B 87 (2013) 125415.
[359] L. Britnell, R.V. Gorbachev, R. Jalil, B.D. Belle, F. Schedin, M.I. Katsnelson, L. Eaves, S.V. Morozov, A.S. Mayorov, N.M.R. Peres, A.H. Castro Neto, J. Leist, A.K. Geim, L.A. Ponomarenko, K.S. Novoselov, Electron tunneling through ultrathin boron nitride crystalline barriers, Nano Lett. 12 (2012) 1707–1710.
[360] G. Cassabois, P. Valvin, B. Gil, Hexagonal boron nitride is an indirect bandgap semiconductor, Nat. Photonics 10 (2016) 262–266.
[361] K. Watanabe, T. Taniguchi, H. Kanda, Direct-bandgap properties and evidence for ultraviolet lasing of hexagonal boron nitride single crystal, Nat. Mater. 3 (2004) 404–409.
[362] C.R. Dean, A.F. Young, I. Meric, C. Lee, L. Wang, S. Sorgenfrei, K. Watanabe, T. Taniguchi, P. Kim, K.L. Shepard, J. Hone, Boron nitride substrates for high-quality graphene electronics, Nat. Nanotechnol. 5 (2010) 722–726.
[363] C.J. Shih, Q.H. Wang, S. Lin, K.C. Park, Z. Jin, M.S. Strano, D. Blankschtein, Breakdown in the wetting transparency of graphene, Phys. Rev. Lett. 109 (2012) 176101.
[364] A.P.S. Gaur, S. Sahoo, M. Ahmadi, S.P. Dash, M.J.F. Guinel, R.S. Katiyar, Surface energy engineering for tunable wettability through controlled synthesis of MoS_2, Nano Lett. 14 (2014) 4314–4321.
[365] C.W. Monroe, L.I. Daikhin, M. Urbakh, A.A. Kornyshev, Electrowetting with electrolytes, Phys. Rev. Lett. 97 (2006) 136102.
[366] K. Ounnunkad, H.V. Patten, M. Velický, A. Farquhar, P.A. Brooksby, A.J. Downard, R. Dryfe, Electrowetting on conductors: anatomy of the phenomenon, Faraday Discuss. (2017), http://dx.doi.org/10.1039/C6FD00252H (in press).
[367] G. Zhang, A.G. Güell, P.M. Kirkman, R.A. Lazenby, T.S. Miller, P.R. Unwin, Versatile polymer-free graphene transfer method and applications, ACS Appl. Mater. Interfaces 8 (2016) 8008–8016.
[368] J.C. Slonczewski, P.R. Weiss, Band structure of graphite, Phys. Rev. 109 (1958) 272–279.
[369] A. Castellanos-Gomez, L. Vicarelli, E. Prada, J.O. Island, K.L. Narasimha-Acharya, S.I. Blanter, D.J. Groenendijk, M. Buscema, G.A. Steele, J.V. Alvarez, H.W. Zandbergen, J.J. Palacios, H.S.J. van der Zant, Isolation and characterization of few-layer black phosphorus, 2D Mater. 1 (2014) 025001.
[370] P.B. James, M.T. Lavik, The crystal structure of $MoSe_2$, Acta Crystallogr. 16 (1963) 1183.
[371] W.J. Schutte, J.L. De Boer, F. Jellinek, Crystal structures of tungsten disulfide and diselenide, J. Solid State Chem. 70 (1987) 207–209.
[372] D.E. Soule, Magnetic field dependence of the hall effect and magnetoresistance in graphite single crystals, Phys. Rev. 112 (1958) 698–707.